QUANTITATIVE COMPARISON OF 2D POROSITY AND PORE GEOMETRY BETWEEN THE UPPER CASTLE HAYNE AQUIFER, NORTH CAROLINA, AND THE BISCAYNE AQUIFER, FLORIDA, USING IMAGE AND GEOSPATIAL ANALYSIS

By

Alexander R. Culpepper

May 2012

Director of Thesis: Dr. Alex K. Manda

Major Department: Geological Sciences

Karst aquifers are vital sources of groundwater for domestic and industrial use in many parts of the world. To sustain rising population throughout the southeastern United States, karst aquifers are increasingly exploited to provide the populace a clean and reliable water resource. The moldic Spring Garden Member of the Castle Hayne Limestone and the vuggy Miami Limestone Formation of the Biscayne aquifer systems are two highly productive karst aquifers that provide critical water resources to millions of people in eastern North Carolina and southeastern Florida, respectively. In order to improve our understanding of karst media, a detailed investigation of 2D porosity and pore geometry of Castle Hayne and Biscayne aquifers was undertaken using image and geospatial analysis. The goal of this study was to compare and contrast the pore structure of moldic and vuggy karst aquifers by quantifying 2D porosity and pore geometry in borehole televiewer, slabbed core, and thin-section images. GIS provided an integrated environment for statistical and geospatial analysis, making it the ideal tool for identifying and extracting pore structures from the digital images. Macropore area and perimeter were derived from televiewer, core and thin-section images. These geometric attributes were used to calculate a shape measure. The shape measure provided additional insight into the

potential for interconnectivity and geometry of pores across the multiple scales of observation. Results show that both pore area and perimeter for the Castle Hayne and Biscayne aquifers can be described by exponential distributions. The moldic Castle Hayne aquifer has larger pore perimeters, when similar pore areas are compared to those extracted from the vuggy Biscayne aquifer. The complexity of shapes are essentially identical at smaller scales of observation for pores derived from both the Castle Hayne and Biscayne aquifers. However, as the scale of observation increases, the difference between the pore geometries of macropores from the Castle Hayne and Biscayne aquifers also increases. At the two largest scales of observation, pores from the Castle Hayne are more complex than pores with identical areas from the Biscayne.

Results also reveal that the scale of measurement plays a critical role in interpreting quantitative macropore structure within karst aquifers, thus requiring an approach that takes into account the scale of measurement of the macropore geometry. As scale of observation increases from thin-section to borehole image, pore size and pore complexity increase considerably over several orders of magnitude. Such quantitative measures can lead to a better understanding of porosity structure in karst aquifers that can be useful for designing and running groundwater flow models and assessing transport mechanisms in karst media. Most importantly, this study provides a quantitative assessment of the distribution of macropore geometry in karst aquifers with different structures and porosity.

QUANTITATIVE COMPARISON OF 2D POROSITY AND PORE GEOMETRY BETWEEN THE UPPER CASTLE HAYNE AQUIFER, NORTH CAROLINA, AND THE BISCAYNE AQUIFER, FLORIDA, USING IMAGE AND GEOSPATIAL ANALYSIS

A Thesis

Presented To the Faculty of the Department of Geological Sciences

East Carolina University

In Partial Fulfillment of the Requirements for the Degree

Master of Science in Geology

By

Alexander R. Culpepper

May, 2012

QUANTITATIVE COMPARISON OF 2D POROSITY AND PORE GEOMETRY BETWEEN THE UPPER CASTLE HAYNE AQUIFER, NORTH CAROLINA, AND THE BISCAYNE AQUIFER, FLORIDA, USING IMAGE AND GEOSPATIAL ANALYSIS

By

Alexander R. Culpepper

APPROVED BY:

DIRECTOR OF THESIS: _____
Dr. Alex K. Manda

COMMITTEE MEMBER: _____
Dr. Donald W. Neal

COMMITTEE MEMBER: _____
Dr. Terri L. Woods

COMMITTEE MEMBER: _____
Dr. Thomas R. Allen

CHAIR OF THE DEPARTMENT OF GEOLOGICAL SCIENCES _____
Dr. Stephen J. Culver

DEAN OF THE GRADUATE SCHOOL _____
Dr. Paul J. Gemperline

DEDICATION

This research is dedicated to my parents for their love, encouragement and most of all their persistence. Without your support, none of this would be possible.

ACKNOWLEDGMENTS

I would like to first thank Dr. Alex Manda for motivating me to pursue this project and serving as my thesis advisor. Thank you for your patience and willingness to truly teach as I went through this process. Your work ethic and vast knowledge of this topic were constants that I could rely on day in and day out.

In addition, the input of committee members Drs. Donald Neal and Terri Woods was greatly appreciated. I am also grateful to have received input from Dr. Tom Allen of the ECU Department of Geography.

Thanks are also extended to the graduate students, faculty, and staff of the ECU Department of Geological Sciences for an enjoyable and rewarding graduate career.

Finally, special thanks are due to my parents, my brother Adam (I know you got tired of me coming back and sleeping on your couch while I finished up) and my girlfriend Sara Michael without your love, encouragement, and support this wouldn't have been possible.

TABLE OF CONTENTS

LIST OF TABLES

LIST OF FIGURES

LIST OF SYMBOLS/ABBREVIATIONS

γ = Shape Index

GIS- Geographic Information System

OTV- Optical Televiewer

CHAS- Castle Hayne Aquifer System

ISODATA- Iterative Self Organizational Data Analysis

FWS- Full Waveform Sonic

ALT- Advanced Logic Technology

CCD- Charged Coupling Device

MSI- Mount Sopris Instruments

RMS- Root Mean Square

VBA- Visual Basic for Application

CHAPTER I: INTRODUCTION

Overview

This manuscript is a component of the requirements for the degree of Master of Science in Geology. The manuscript has been prepared in four parts: (1) General introduction (this section); (2) an independent article to be submitted to a peer-reviewed journal; (3) Additional insights and final synopsis; and (4) detailed supplementary material not included in the journal article but significant to the overall understanding of the material presented. As a result of the four part configuration of the manuscript, there may be repetition.

Chapter I

Chapter I presents the introduction, overview, and objectives of this thesis.

Chapter II

The body of the thesis is found within Chapter II, which is a self contained journal article titled: A Quantitative Investigation of Moldic and Vuggy Pore Structure in Karst Aquifers Using Image and Geospatial Analysis. This complete journal article will be submitted for publication.

Chapter III

Chapter III provides an overall summary including additional insights and applications to water resource management.

Appendices

Appendices A, B, and C include detailed supplementary material of the hydrogeology of the Castle Hayne aquifer system, Biscayne aquifer system, and methods of analysis including detailed data acquisition and image processing techniques. Appendices D through K include additional figures and tables.

Objectives

The goal of this study is to quantitatively characterize and compare the geometry, statistical distribution and scaling properties of macropores from the Castle Hayne and the Biscayne aquifers at three scales of observation using digital imaging and spatial analysis techniques. The three scales of observation used are borehole, core, and thin-section. Specific objectives are to:

- Employ multiple techniques to collect, manipulate, and analyze porosity from moldic and vuggy aquifers.

- Quantitatively characterize porosity in borehole, core, and thin-section images of the Castle Hayne and Biscayne aquifer.

- Compare and contrast porosity and pore geometry in the Biscayne and the Castle Hayne aquifers at three scales of observation (i.e. borehole, core, and thin-section images).

- Investigate the scaling relations of porosity and pore geometry between the Castle Hayne and Biscayne aquifers.

CHAPTER II: A QUANTITATIVE INVESTIGATION OF MOLDIC AND VUGGY PORE STRUCTURE IN KARST AQUIFERS USING IMAGE AND GEOSPATIAL ANALYSIS

Abstract

In order to improve our understanding of karst media, a detailed investigation of porosity and pore geometry was undertaken in the moldic Castle Hayne and the vuggy Biscayne aquifers using image and geospatial analysis. The goal of this study was to compare and contrast the pore structure of moldic and vuggy karst aquifers by quantifying porosity and pore geometry. Remote sensing and GIS software were used to classify high resolution optical televiewer, core, and thin-section images. GIS provided an integrated environment for statistical and geospatial analysis, making it the ideal tool for identifying and extracting pore structure from the digital images. Results show that both pore area and perimeter for the Spring Garden Member of the Castle Hayne aquifer and Miami Limestone Formation of the Biscayne aquifer exhibit exponential distributions. In all sets of optical televiewer, core, and thin-section images, relatively small pores have the highest occurrence, whereas large pores occur less frequently. The moldic Castle Hayne aquifer has larger pore perimeters, when similar pore areas are compared to those extracted from the vuggy Biscayne aquifer. These results show that quantitatively interpreting macropore structure within karst aquifers requires an approach that takes into account the scale of measurement of the macropore geometry. Most importantly, this study provides a quantitative assessment of the distribution of macropore geometry in karst aquifers with different structures and porosity.

2.1 Introduction

Carbonate aquifers are vital sources of groundwater for domestic and industrial use throughout the world. To sustain rising population throughout the southeastern United States, these aquifers are increasingly exploited to provide the populace clean and reliable water sources. The Castle Hayne and Biscayne aquifer systems are two highly productive carbonate aquifers that provide potable water to millions of people in eastern North Carolina and southeastern Florida, respectively. The highly complex internal structure of carbonate aquifers is a result of slightly acidic groundwater circulating through the limestone bedrock resulting in the development of dissolution features (White, 1988). Exposure to the circulating groundwater allows features to continue to develop and thus extend in size from dissolved fossils to large caves or caverns (Halihan et al., 2000; Clémens et al., 1999). The resulting enlargement of dissolution features may significantly influence the hydrologic properties of a formation by way of enhanced porosity and interconnectivity (Choquette and Pray, 1970).

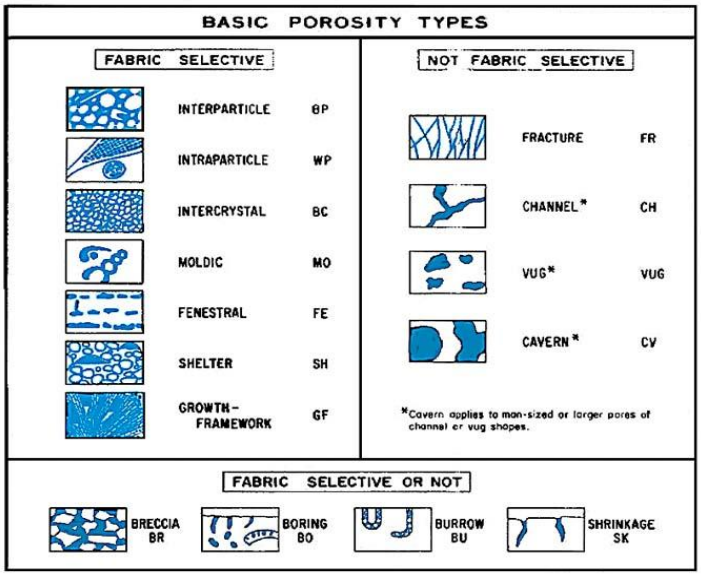

Figure 1. Classification system of a variety of basic pore types (Choquette and Pray, 1970). The fabric selective category is useful for stratigraphic analysis, while the non-fabric selective category has the greatest impact on fluid flow in carbonate rock systems.

The complex and heterogeneous character of carbonate aquifers is a direct result of this interconnectivity, which makes management of groundwater resources, development of protection strategies, and evaluation of potential contaminant transport exceedingly difficult (Mace and Hovorka, 2000; Taylor and Green, 2001; Scanlon et al., 2003; Smith et al., 2003, 2005). Evaluating and comparing carbonate aquifer systems often requires the use of data that are more difficult to obtain, such as quantitative measures of pore attributes and spatial distribution of porosity. This approach is important for understanding how hydrologic properties of karst aquifers are influenced by pore geometry and structure beyond the limitation of traditional aquifer characterization.

Choquette and Pray (1970) broadly classified macropores using the term 'vug', which they defined as a secondary pore that is somewhat equant or not markedly elongated, large enough to see with the unaided eye and does not specifically conform in position or shape to particular fabric elements of the host rock (Fig. 1). A moldic pore is defined by Choquette and Pray (1970) as a secondary pore formed by the selective (complete or partial) removal, normally by solution, of a former constituent such as a shell or oolith (Fig. 1). Commonly, moldic pores serve as precursors to vugs, which, with continued dissolution, can represent solution enlargement of fabric-selective pores to such an extent that the precursor can no longer be recognized (Choquette and Pray, 1970). Choquette and Pray (1970) also identify channelized porosity as being regularly associated with fracture porosity as well as vug and solution-enlarged moldic porosity. Lucia (1995) later subdivided vug or 'vuggy' pore space into two groups depending on how the vugs are interconnected: (1) separate vugs could be defined as vugs interconnected only through the interparticle pore network, and (2) touching vugs, are defined as vugs that form an interconnected pore system. The term 'conduit' refers to solution enlarged

pathways in the form of pipes or channels with impervious irregular walls whose apertures exceed 1 cm and form a connected network (Jeannin, 2001; White 2002; Worthington, 2000). Solution features that function as large aperture, low tortuosity, interconnected pathways, undoubtedly influence direction and rates of groundwater flow (Dreiss, 1982, 1989).

Analyzing the pore structure of karst media at a single scale of measurement (i.e. only thin-section) can provide lesser results because thin-sections are limited by size and do not account for the wide range in dimension of solution features present in karst aquifers. Core samples capture more features than thin-sections. However core analysis is largely dependent on the quality of core recovered which can be extremely low when drilling in karst formations. Digital borehole images provide a better representation of conduits and large dissolution features that could not be observed in thin-section or slabbed core. But as a result of image resolution, smaller scale features observed in thin-section and slabbed cores are hard to distinguish in borehole images, yet these features still affect the porosity and connectivity of the system. To effectively analyze and compare pore structures in karst, multiple scales of observation must be used to take into account the range of pore sizes.

In this study, digital imaging and spatial analysis techniques were used to quantitatively characterize and compare the pore geometry, and distribution of macropores from the Castle Hayne and Biscayne aquifers at three scales of observation: thin-section, core, and digital borehole images.

2.1.1 Geospatial image analysis

Remote sensing and Geographic Information Systems (GIS) have been used in the past to produce data sets classifying land cover (Wen and Tateishi, 2001), to detect clear-cutting of

boreal forest (Smith and Askne, 2001), and to map riparian ecosystems (Bourgeau-Chavez et al., 2007). All these demonstrate traditional applications of the technology. Image analysis techniques and GIS have more recently been used to quantitatively characterize and map porosity from digital borehole images (Cunningham et al., 2004a; Manda and Gross, 2006b). This non-traditional application of these methodologies is particularly useful for developing an understanding of karst aquifers (Cunningham et al., 2004a). Advances in computer processing abilities now make classification of digital images more appealing for analyzing porosity and pore geometry than other non-traditional techniques.

Manda and Gross (2006b) successfully applied new techniques incorporating GIS and image analysis to quantitatively calculate vuggy and conduit porosity in high-resolution digital borehole images in the Biscayne aquifer. Similar techniques are applied here to the Castle Hayne aquifer in an effort to gain a better understanding of pore structure and geometry in the aquifer. The GIS techniques developed by other workers not only provided the framework for quantifying geometry, distribution, and scaling properties of macropores but also allowed for direct comparison of porosity structure in vuggy and moldic aquifers.

2.1.2 Castle Hayne aquifer

Spanning approximately 12,500 square miles (3,200 km²) (Fig. 2), the Castle Hayne aquifer is the most productive aquifer in North Carolina, providing withdrawals upwards of 140 million gallons of water per day (530 million liters of water per day) (Lyke and Treece, 1988). In Craven County, North Carolina, USA the Castle Hayne aquifer is used for various industrial and agricultural purposes, whereas the majority of potable water for municipal and domestic use is supplied by the Cretaceous aquifer system. The stratigraphic section analyzed in this study

corresponds to the Spring Garden Member of the Castle Hayne Limestone (See Table 2, Appendix A). The limestone sequence was deposited in a low energy, shallow, tropical, marine basin during a middle Eocene transgressive sea (Thayer and Textoris, 1972, 1977; Ward and Blackwelder, 1978, 1980). Ward and Blackwelder (1978) redefined the limestone portion of the Castle Hayne formation as a sandy, molluscan-mold bio calcirudite. Thayer and Textoris (1977), using the Choquette and Pray (1970) classification scheme, described porosity as being primarily controlled by selective leaching of aragonite shells, that produces molds, vugs, and channels. Refer to Appendix A for supplementary materials describing the Castle Hayne aquifer.

2.1.3 Biscayne aquifer

The Biscayne aquifer spans approximately 6,400 square miles (16,500 km²) across Miami Dade, Broward, Palm Beach, and Monroe Counties in southeastern Florida, USA (Klein and Hull, 1978) (Fig. 2). The Biscayne aquifer is the principal water supply for Miami, Boca Raton, Pompano Beach, Fort Lauderdale, Hollywood, Miami Beach, and Homestead. In southeastern Florida, the subsurface is dominated by, semi-consolidated limestone and marl deposits of Pleistocene age associated with marine terraces that formed when the area was inundated by the sea at different times (Heath, 1984). The stratigraphic sections analyzed in this study correspond to the lower part of the Miami Limestone and the upper part of the Fort Thompson formations (See Table 3, Appendix B). Schroeder et al. (1958) and Parker et al. (1955) note that the marine limestone beds have been most affected by solution activity from percolating groundwater. As a result of dissolution, the highly permeable rock mass is riddled with secondary solution cavities as large as several feet (1m) in diameter. Consistent with Choquette and Pray's (1970) classification scheme, Vacher and Mylroie (2002) describe the porosity of the Biscayne aquifer as 'eogenetic' karst experiencing meteoric diagenesis. Cunningham et al. (2009), building upon

the carbonate pore-space classification scheme of Lucia (1995, 1999), divided the pore systems of the Biscayne into two types: (1) matrix porosity (interparticle and separate vugs), and (2) touching-vug porosity (biogenic macroporosity). Refer to Appendix B for Biscayne aquifer supplementary material.

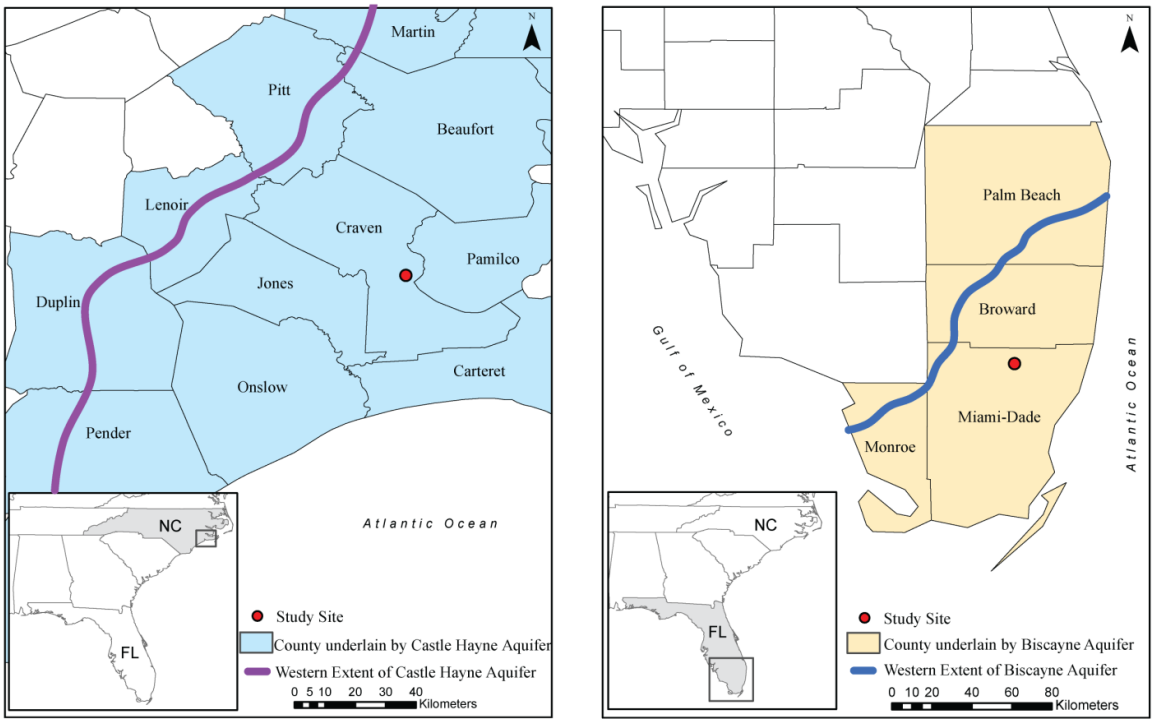

Figure 2. Locations from which core samples and borehole images were derived (a) Map of eastern North Carolina showing the aerial extent of the Castle Hayne aquifer and study site in Craven County (westernmost extent of Castle Hayne aquifer North Carolina modified from Woods et al. 2000); (b) Map of southern Florida showing the aerial extent of the Biscayne aquifer and location of study site in northern Miami-Dade County, Florida (western extent of Biscayne aquifer modified from Manda and Gross, 2006b).

2.2 Methods of Analysis

2.2.1 Data acquisition

The procedure for converting raw digital imagery to a format in which GIS can be used to extract data on pore geometry requires two primary steps: (1) acquisition of data at three scales

of observation from the two karst systems, and (2) processing of images for subsequent spatial analysis (Fig. 3). Dimensions of borehole images are 18 m or less in length by 0.2 m in circumference. Whereas core samples utilized are less than 0.1 x 0.3 m and thin-sections are approximately 0.4 x 0.7 m.

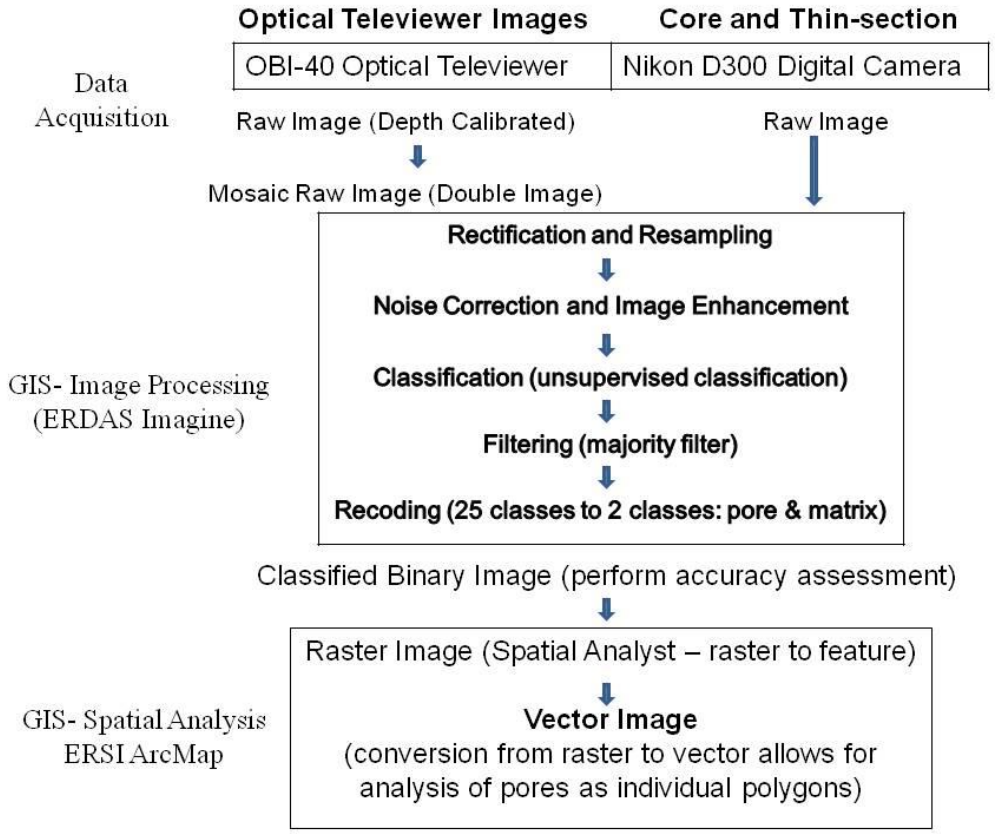

Figure 3. Flow chart outlining data collection and processing procedures for geospatial analysis of digital borehole, slabbed core samples, and thin section images (Modified from Manda and Gross, 2006b)

At both study sites digital images of borehole walls were acquired by using the OBI-40 slimhole optical televiewer manufactured by Advanced Logic Technology (ALT). Data from the Biscayne aquifer were acquired from a well that was drilled by the United States Geological Survey (USGS) in early 2000, to understand and characterize the stratigraphy and hydrogeology

of the Biscayne aquifer. Test corehole G-3770 was drilled to a depth of approximately 25.0 m in Northern Miami Dade County (Fig. 2). Polyvinyl Chloride (PVC) casing was set to a depth of 2.4 m which allowed the optical televiewer to image the 15.3 m of open hole. Core recovery was < 50% attributable to the presence of solution cavities.

Previous researchers (Manda and Gross, 2006b) converted optical televiewer and core images recovered from G-3770 to binary format that were used as source images for GIS analysis in this study. Thin-sections acquired from the core retrieved from well G-3770 were used in this project.

In the late 1990's, 17 pumping and observation wells were drilled for the city of New Bern to understand the hydrogeologic framework underlying the inactive Martin Marietta-Glenburnie quarry. Research conducted in this study focused on one of these wells (MM-PW5), which is a six-inch borehole, located in the southeast corner of the quarry (Fig.2). MM-PW5 was drilled to a depth of approximately 21 m and PVC casing was set to a depth of approximately 9 m. The rest of the well is an open borehole allowing the optical televiewer to image 12 m of the borehole. The highest clarity section of the image between 11.8 m and 16.2 m was selected for analysis. Cores were retrieved between the depths of 11.4 and 13.3 m and 18.3 to 19.1 m. Previous researchers slabbed cores and produced thin-sections from 0.5 m intervals.

Optical televiewer image logs are particularly valuable as they provide continuous uninterrupted views of the inside of the well bore. Use of WellCad software allowed the resulting borehole wall image to be exported as a depth-calibrated image file. Following the procedures outlined by Manda and Gross (2006b) cores acquired from MM-PW5 were slabbed and the flat surfaces were polished to reduce irregularities and roughness introduced by the sawing process. The cores were then painted with an orange water-soluble block printing ink to amplify the

difference between macropores and matrix. Thin-sections from both core sets were impregnated with blue epoxy by previous researchers, using a method similar to the one implemented by Friedman (1959). The blue epoxy enhanced the difference between the macropores and matrix, just as the orange block printing ink did to the core samples. Except that in the case of the thin sections, the blue color represented pores, whereas in the core samples the orange color represented matrix. Examples of core and thin-section images from the Biscayne and Castle Hayne aquifers are shown in Figure 4. Refer to Appendix C data acquisition for supplementary materials.

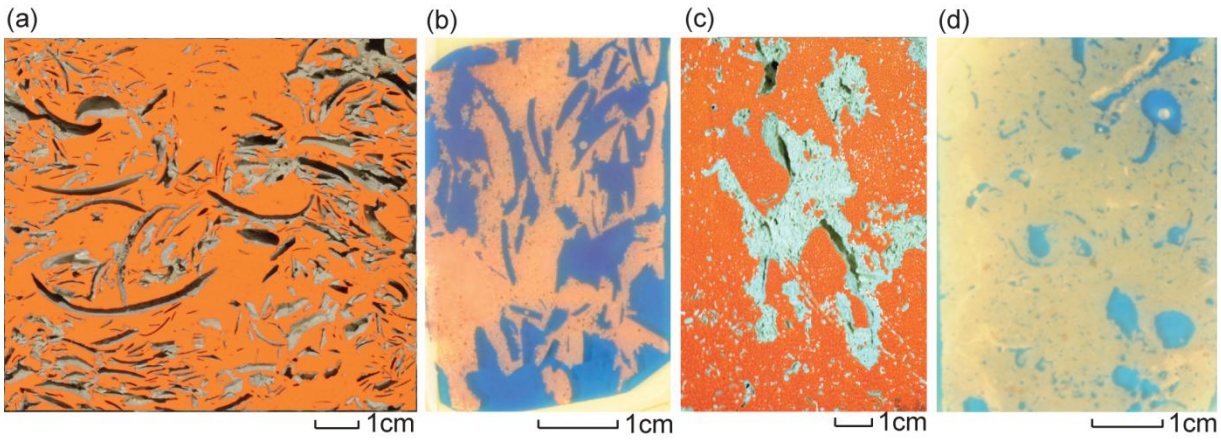

Figure 4. Examples of painted cores and thin-sections impregnated with blue epoxy: (a) Castle Hayne core; (b) Castle Hayne thin-section; (c) Biscayne core; (d) Biscayne thin-section.

2.2.2 Image processing and spatial analysis

Converting images of boreholes, slabbed core, and thin-section into a format that could be examined and manipulated in GIS was essential to obtain accurate information for image analysis. The method for converting digital images to a binary classified image format suitable for GIS analysis consisted of: image mosaic, rectification/calibration, noise removal, image enhancement, binary classification, and filtering (Fig. 3). Converting images to a GIS ready format followed procedures presented by Manda and Gross (2006b).

Using ERDAS Imagine® 9.3, two copies of the same optical televiewer image were placed side by side to create a double image. The double image was important for measuring the correct geometry of pores that intersect the edges of the borehole images. The borehole image is a 360° view, a pore that is truncated by the edge is actually continuous across to the other side of the image, which is not the case in slabbed core and thin-section images. During the rectification procedure images were resampled to a smaller cell size using the nearest-neighbor method to more accurately mimic features found on the original image during the classification procedure. The ISODATA (Iterative Self Organizational Data Analysis) algorithm was used to generate 25 classes for the unsupervised classification (ERDAS, 2010a). Each of the 25 classes was recoded to a specific matrix or macropore value based on comparison of a single computer-generated class to original raw image, the resulting binary image consisted of two values, one matrix and the other macropores (Fig. 5). Refer to Manda and Gross (2006b) for specific classification procedures.

Obtaining pore-attribute information from the binary classified images required conversion to a vector format line (Fig. 5). Vector analysis in ArcMap® 9.3 provided a means to identify and characterize pores based on purely geometric parameters (Fig. 5). See Appendix C for supplementary material on image processing and spatial analysis.

2D porosity is here defined as the percentage of surface area occupied by macropores within a rectangular window. After generating a rectangle with the dimensions of interest ArcMap field calculator was used to calculate the total area of all macropores within the window. Once the area of macropores within the rectangle was determined, simply dividing by the area of the rectangle gave a percent area covered by macropores (i.e. the porosity). This porosity calculation procedure was repeated for each image at the three scales of observation.

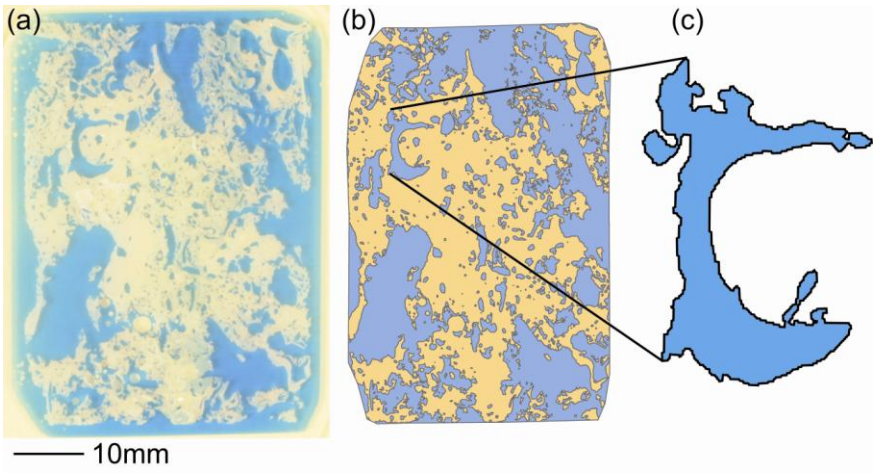

Figure 5. (a) Photograph of thin-section from the Biscayne aquifer; (b) Vector file of thin-section from the Biscayne aquifer; (c) Example of pore within the thin-section from which geometric attributes can be extracted (i.e. area, perimeter, and a shape index).

2.3 Results

The effects of image resolution were first considered before analyzing geometric attributes derived from images of different dimensions. This is important because geometric attributes were extracted at three scales of observation where the resolution of the images determines the minimum pore sizes that can be detected with accuracy. Therefore, minimum pore areas used for televiewer, core and thin-section images were 4.00 cm^2, 0.001 cm^2, and 1.0 x 10^{-5} cm^2, respectively. The minimum pore values determined were used as the threshold base line for the majority of subsequent quantitative analysis. When evaluating the true shape of pores, only pores that did not intersect the edge of the image were included in the analysis of pore geometry. Pores that intersect the edge of an image will possess a false shape because the pore in the image is truncated by an artificial boundary. Thus, truncated pores do not represent true areas, perimeters, and shapes of pores (Fig. 6). However, these pores were included in the calculation for porosity.

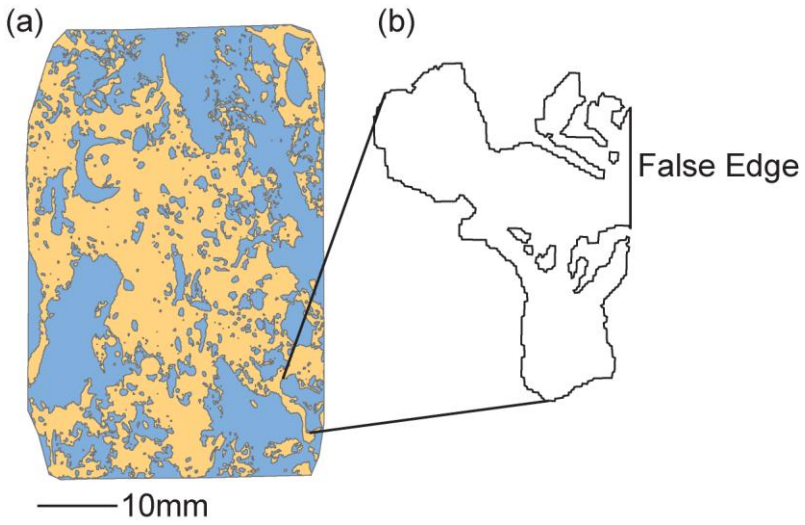

Figure 6. Extracting pores with only true geometries for analysis (a) Thin-section from the Biscayne aquifer after completed image processing (b) Example of pore which could not be included in pore geometry analysis because of the false edge that occurs where the pore intersects the boundary of the image.

2.3.1 Validation of image analysis techniques

The image analysis techniques presented are completely dependent on the strength of image classification; poor classification could lead to inaccurate representation of the original environment as a consequence of improper class designation. An accuracy assessment for the classification process, common in remote sensing analysis (Congalton, 1991), was performed by comparing accuracy of the classified binary image to the original image. The accuracy assessments for all binary classified images utilized in the study have mean kappa coefficients and overall accuracy of over 0.80 and 90%, respectively. These results show that the image analysis method is valid and results obtained from classified images will be accurate to at least 90 percent, which falls well within the range of acceptable accuracies for remotely sensed images (Congalton, 1991; Campbell, 1996; Lillesand, 2004).

2.3.2 Pore area, perimeter, and shape index distributions

In the optical televiewer images from the Biscayne and Castle Hayne aquifers, pores with the smallest areas (i.e. < 25cm²) have the highest occurrence whereas relatively larger pores occur less frequently. The distribution of pore areas from the Castle Hayne aquifer televiewer image ranges from ~4 cm^2 to ~609 cm², with a mean of ~20 cm² (Fig. 7a). Pore areas derived from the Biscayne aquifer televiewer image range from ~4 cm² to ~1469 cm², with a mean of ~32 cm² (Fig. 7b). The Biscayne televiewer image had a relatively higher number of moderately sized pores (50-100 cm²) compared to the Castle Hayne televiewer image (Fig. 7a, 7b).

For pores derived from Castle Hayne aquifer core images (Fig. 7c), the pore areas range from 0.001 cm² to 7.01 cm² with a mean of 0.040 cm², whereas the pore areas from Biscayne aquifer core images range from 0.001 cm² to 5.84 cm², with a mean of 0.012 cm² (Fig. 7d). Similar to the optical televiewer images there were very few large pores and a very large number of relatively small pores (< 0.10 cm²) in the core images. In general pore areas from the Biscayne aquifer were smaller than those from the Castle Hayne aquifer core images.

The pore areas from all Castle Hayne aquifer thin-section images (Fig. 7e) range from 1.40×10^{-5} cm² to 0.805 cm², with a mean of 2.22×10^{-3} cm², whereas the pore areas from the Biscayne aquifer thin-section images (Fig. 7f) range from 4.00×10^{-5} cm² to 0.397 cm², with a mean of 2.43×10^{-3} cm². Relatively small pore areas of less than 0.001 cm² occurred most frequently in both images. Mean pore areas are similar in both sets of thin-section images.

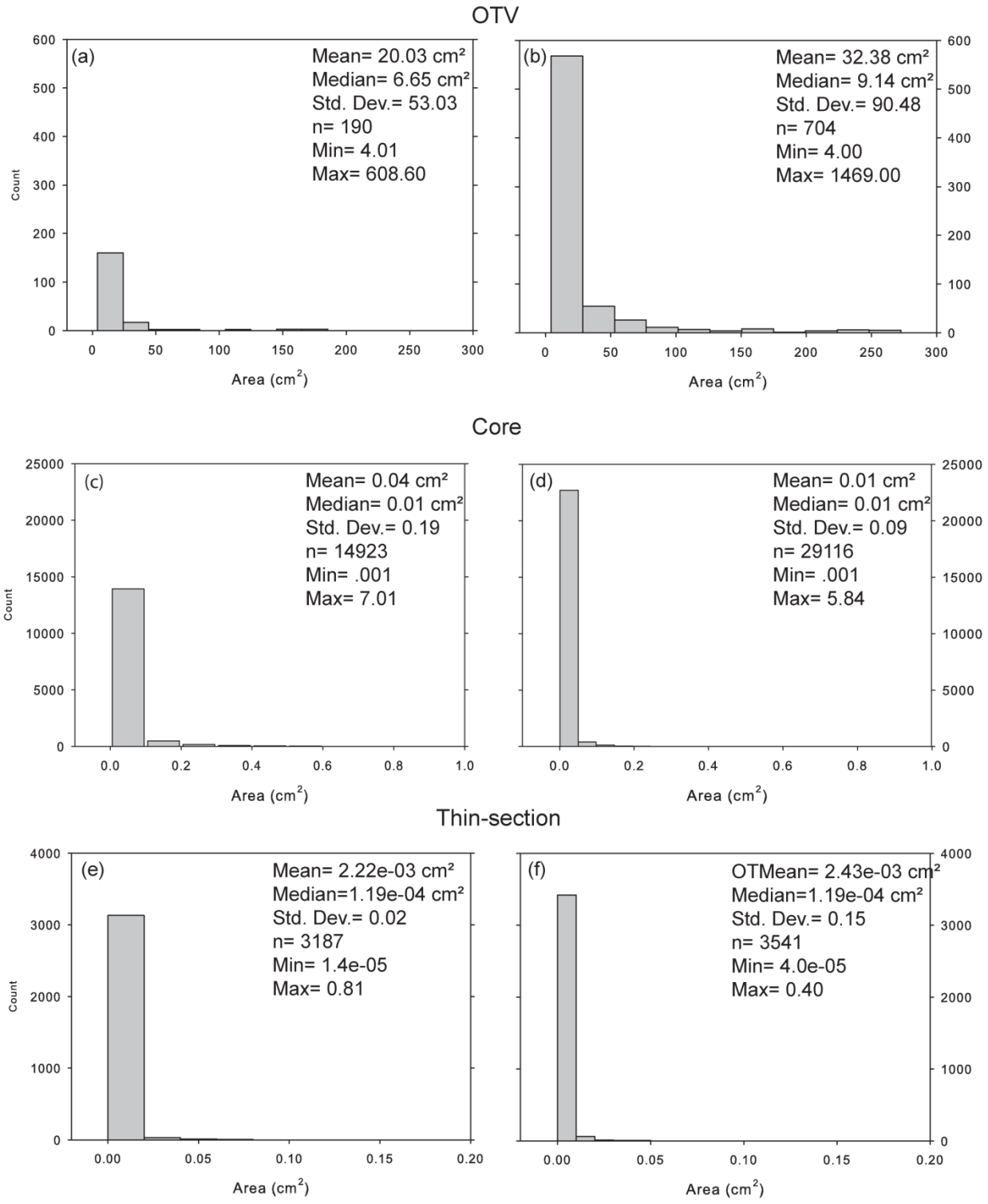

Figure 7. Histogram of areas of pores derived from (a) televiewer image of the Castle Hayne; (b) televiewer image of the Biscayne; (c) core images of the Castle Hayne; (d) core images of the Biscayne; (e) thin-section images of the Castle Hayne; (f) thin-section images of the Biscayne. (All pore area histograms can be found in Appendix K)

Pore perimeters extracted from optical televiewer images also follow an exponential distribution, with small perimeters occurring at the highest frequency and large perimeters occurring less frequently. The pore perimeters from the Castle Hayne aquifer televiewer image (Fig. 8a) range from 18.20 cm to 2554.18 cm with a mean of 99.98 cm. In the Biscayne aquifer televiewer image, perimeters of pores range from 8.00cm to 2789.36 cm, with a mean of 55.88 cm (Fig. 8b). In the Castle Hayne televiewer image, mean pore perimeter was nearly twice that of the mean pore perimeter of the Biscayne televiewer image.

The distribution of pore perimeter from all core images of the Castle Hayne aquifer (Fig 8c) ranges from 0.019 cm to 82.01 cm with a mean of 0.843cm. Distribution of all pore perimeters from Biscayne aquifer cores images (Fig 8d) range from 0.10 cm to 49.56 cm, with a mean of 0.44 cm. Pore perimeters from both aquifer cores follow a exponential distribution. The Castle Hayne core images had a higher number of pores with moderate perimeters (2 cm-4 cm) compared to Biscayne core images resulting in a mean pore perimeter of the Castle Hayne nearly twice that of mean pore perimeter of Biscayne core images.

The distribution of pore perimeter from all Castle Hayne aquifer thin-section images (Fig. 8e) ranges from 0.016 cm to 13.38 cm with a mean of 0.139 cm. In all the Biscayne aquifer thin-section images pore perimeter ranges from 0.008 cm to 17.64 cm, with a mean of 0.156 cm (Fig. 8f). The exponential distribution observed in pore areas holds true in corresponding pore perimeters in images from all three scales of observation.

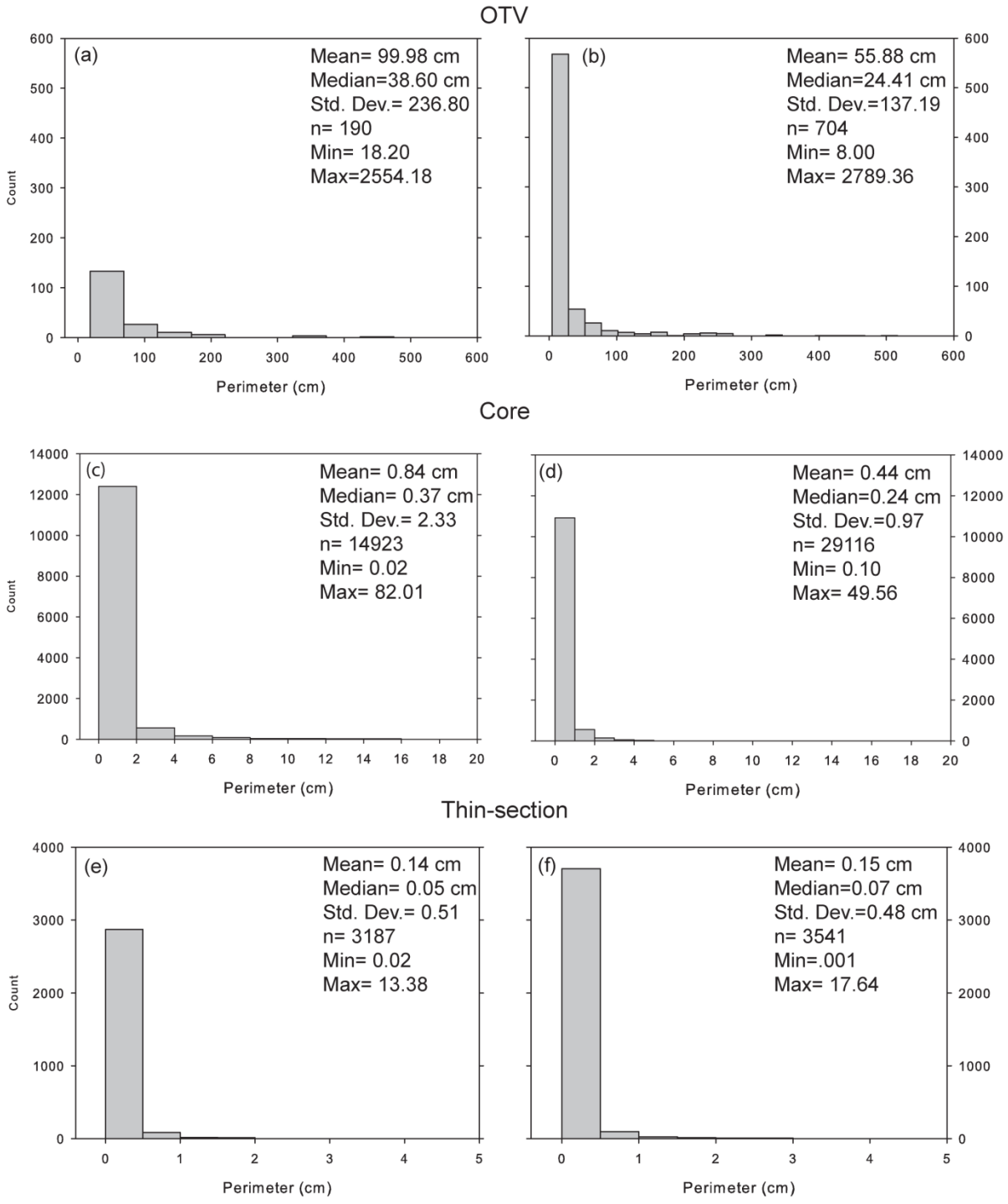

Figure 8. Histogram of perimeters of pores derived from (a) televiewer image of the Castle Hayne; (b) televiewer image of the Biscayne; (c) core images of the Castle Hayne; (d) core images of the Biscayne; (e) thin-section images of the Castle Hayne; (f) thin-section images of the Biscayne. (All pore area histograms can be found in Appendix K)

Porosity affects the physical properties of rocks (e.g. strength, density and permeability); however, this is greatly influenced by the geometry of pores within the media (Anselmetti and Eberli, 1993; Lucia, 1995). Elongated or interconnected pores have different effects on physical properties than simple round pores (Wikens et al., 1991). Pore area and perimeter measurements were used to compute, a shape measure that describes the complex nature of pore shapes in carbonate rocks):

$$\gamma = \frac{P}{2\sqrt{\pi A}}$$

Where γ is the shape index, *P* is the perimeter and *A* is the area of the pore (Anselmetti et al., 1998). The shape index has a range from one to infinity; a shape index of one would represent a circle and higher values indicate an increase in complexity of the shape. Shape index is associated with the connectivity of the pore because complex, branching pore geometries are more likely to form connected pore networks (Anselmetti et al., 1998).

The shape index from the televiewer image of the Castle Hayne (Fig. 9a) ranges from 2.39 to 29.2 (mean = 5.39). In the televiewer image of the Biscayne, the shape index ranges from 1.04 to 20.5 (mean = 2.70) (Fig. 9b). In both optical televiewer images, pores displayed an exponential distribution illustrating that the majority of macropores are simple in shape (shape index of 2-4). In the televiewer image of the Castle Hayne aquifer, the majority of pores have shape indices between 2 and 6, while the majority of pores in the Biscayne televiewer image have shape indices between 1 and 4. Mean shape index of pores derived for the televiewer image of the Castle Hayne aquifer is nearly twice as large as that derived from the Biscayne aquifer. This shows that macropores in the Castle Hayne aquifer are more complex than pores in the Biscayne aquifer.

The mean shape index of the pores derived from core images of the Castle Hayne aquifer (1.49) is slightly higher than that derived from core images of the Biscayne aquifer (1.46) (Figs. 9c & d). The histograms for the shape indices derived from the Biscayne and Castle Hayne aquifers show that there are more macropores with simple shapes captured in the Biscayne aquifer than the Castle Hayne aquifer. In the core images of both aquifers, simple pores occur at a high frequency whereas complex pores occur at low frequency. This shows that moldic pores are slightly more complex than vuggy pores, however, there are more vuggy pores captured at the same scale of observation.

The shape indices from thin-section images of the Castle Hayne and Biscayne aquifers averaged 1.31 (Figs. 9e & f). Similar to what was observed in the core and televiewer images, pores with relatively simple shapes occur at the highest frequency whereas complex pores occur at the lowest frequency. Histograms of shape indices for both sets of thin-sections are similar in shape suggesting that at this scale of observation, macropore structures of the Castle Hayne and Biscayne aquifers are not that different.

2.3.3 Pore geometry variations

Scatter plots of pore area versus perimeter cross plots derived from the optical televiewer images of the Castle Hayne and Biscayne aquifers (Fig. 10a), there is a positive relationship between pore area and pore perimeters: big pores are associated with large pore perimeters. The line of best fit for the Castle Hayne televiewer has a steeper slope than the Biscayne televiewer, which illustrates pore areas in the Castle Hayne aquifer have larger pore perimeters than similar Biscayne aquifer pore areas.

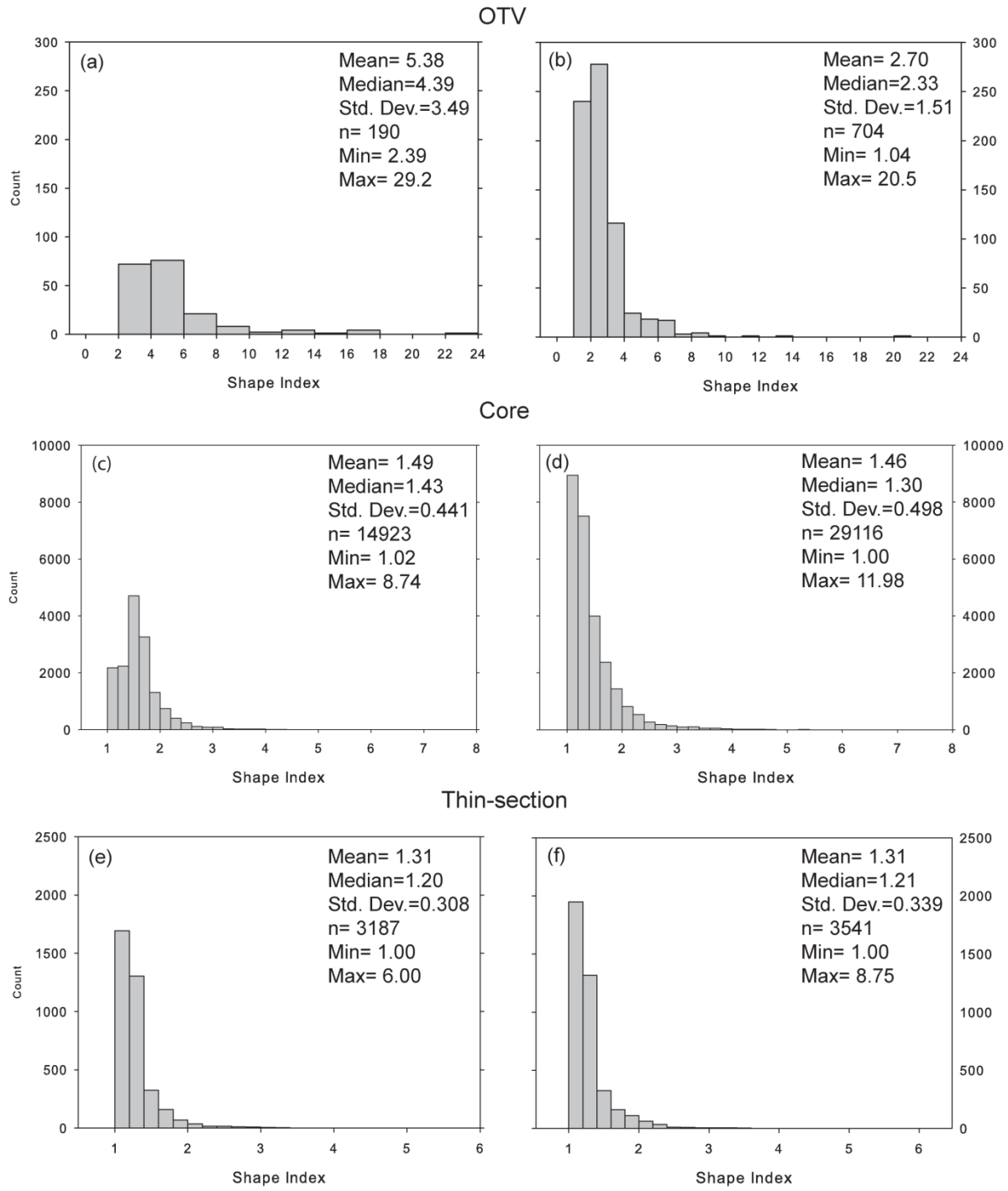

Figure 9. Histogram of pore shape index derived from (a) televiewer image of the Castle Hayne; (b) televiewer image of the Biscayne; (c) core images of the Castle Hayne; (d) core images of the Biscayne; (e) thin-section images of the Castle Hayne; (f) thin-section images of the Biscayne.

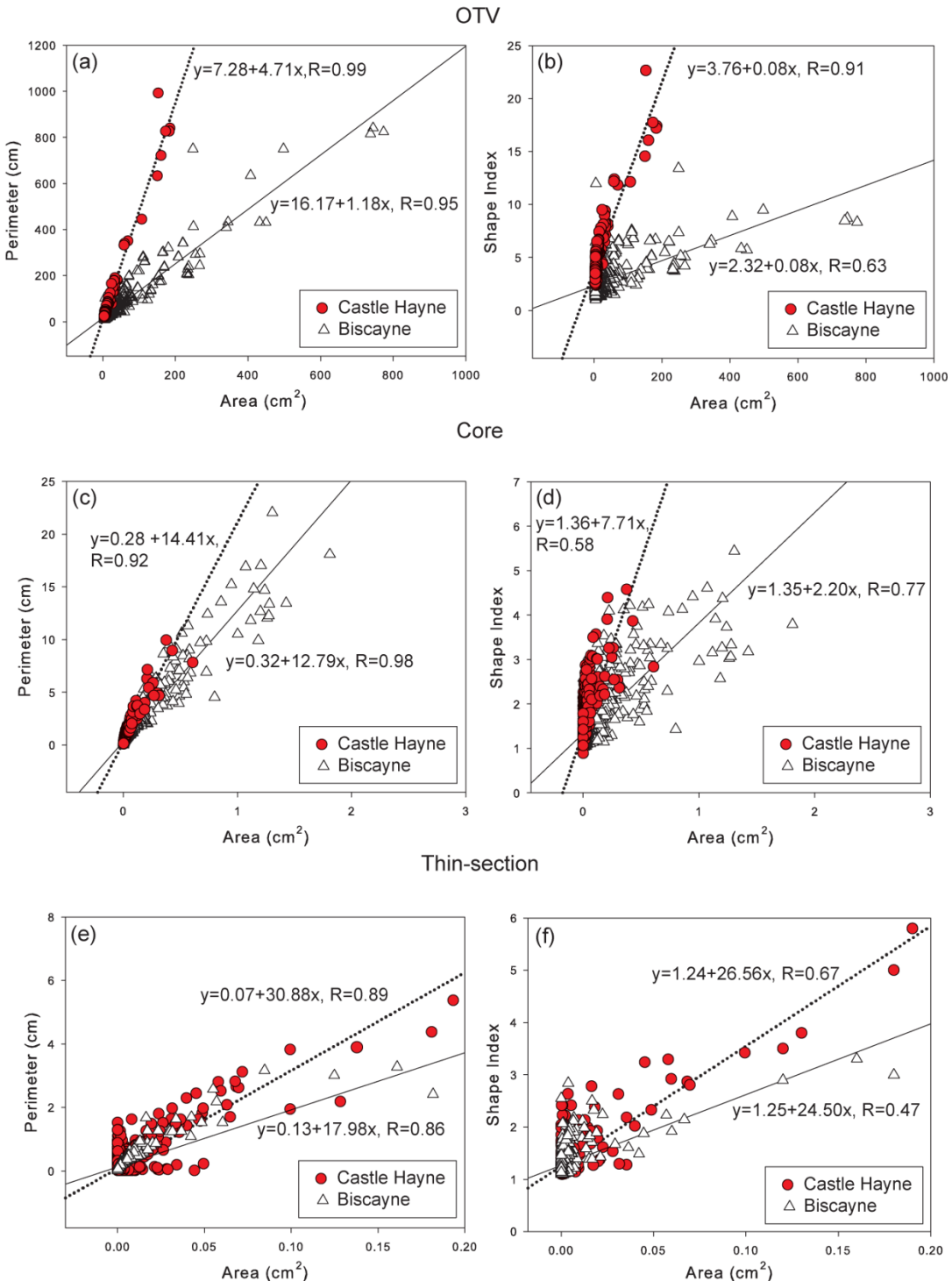

Figure 10. Pore area vs. perimeter (a) from data derived from televiewer images; Pore area vs. shape index (b) from data derived from televiewer images; Pore area vs. perimeter (c) from data derived from core images; Pore area vs. shape index (d) from data derived from core images; Pore area vs. perimeter (e) from data derived from thin-section images; Pore area vs. shape index (f) from data derived from thin-section images.

Scatter plots of pore area versus shape index derived from televiewer images (Fig. 10b) show there is a positive relationship between pore area and shape index in both the Castle Hayne and Biscayne aquifer plots, although the Castle Hayne televiewer line of best fit has a steeper slope than the Biscayne televiewer. The line of best fit with a steeper slope suggests that as pore area increases in Castle Hayne televiewer, the complexity of the shape will increase more rapidly compared to Biscayne televiewer pore areas.

Scatter plots of pore area versus perimeter derived from core images (Fig. 10c) show a positive relationship between pore area and pore perimeter, with the Castle Hayne and Biscayne aquifers having very similar slopes. In both the Castle Hayne and Biscayne core images, as pore area increases, pore perimeters increase at comparable rate. The slope of the best-fit line for the cores belonging to the Castle Hayne aquifer is slightly higher than the Biscayne cores. However, on the area versus shape index scatter plots (Fig. 10d), the best-fit lines diverge and the Castle Hayne has a much steeper slope. Figure 10d shows positive relationship between pore area and shape index in both the Castle Hayne and Biscayne aquifers core images. Despite the similarity of pore areas and perimeters (Figure 10c), scatter plots of pore area versus shape index of cores illustrate that pores in the Castle Hayne are more complex than those derived from the Biscayne.

Scatter plots of pore area versus perimeter derived from thin-section images (Fig. 10e) again demonstrate a positive relationship between areas pore perimeters. In both sets of thin-sections, as pore area increases pore perimeter increases at comparable rates. The best-fit line of the Castle Hayne has a steeper slope than the best-fit line of the Biscayne, but in area versus shape indexes scatter plots (Fig. 10f) the slopes of best-fit lines are fairly similar. Scatter plots derived from thin-sections shows a positive relationship between pore area and shape index.

2.3.4 2D porosity analysis

Using the methods summarized in Section 2.2, the overall mean 2D porosity was calculated for the optical televiewer, core, and thin-section images. Computation of the porosity takes into account all pore space including truncated pores that intersect the edges of the images. The mean porosity from the televiewer image of the Castle Hayne was lower than the mean porosity from the televiewer image of the Biscayne (Table 1). The porosity calculated from all Castle Hayne core images, however, was higher than the porosity from Biscayne core images. Mean porosity from the thin-sections of the Castle Hayne was higher than mean porosity from the thin-sections of the Biscayne.

Highest mean porosity generated from the Castle Hayne at a single scale of observation was the mean thin-section porosity (40%). Porosity generated from the Castle Hayne had an 8% deviation across the three scales of observation. In the Biscayne, the televiewer image generated the highest porosity (39%) from a single scale of observation and the variation in porosity was 16% across the three scales of observation. The lowest mean porosity (23%) was calculated from cores of the Biscayne aquifer, this low porosity is possibly a result of the poor core recovery of highly porous sections.

Table 1. Mean 2D porosities acquired from optical televiewer, core and thin section images of the Castle Hayne and Biscayne Aquifers (range in parentheses)

Scale of Observation	Castle Hayne	Biscayne
Optical Televiewer	32%	39%
Core Images	36% (25-51%)	23% (6-65%)
Thin-section Images	40% (20-64%)	38% (5-68%)

2.4 Discussion

Karst aquifers are highly heterogeneous systems; this holds true in the Castle Hayne and Biscayne units evaluated in this study, and becomes more evident during quantitative evaluation of porosity at multiple scales of observation. The following section discusses the distribution of macropore geometries and effects of scale on pore geometry attributes.

2.4.1 Influence of scale of observation on pore characteristics

Based on geospatial analysis, porosity structures were broken into two main categories: 'macropore' and 'conduit.' Any dissolution feature larger than the minimum pore area (4.00 cm^2) and not continuous from one end of the televiewer image to the other was designated 'macropore.' Conduits are continuous features spanning the entire width of the televiewer image. From the 5 m, Castle Hayne televiewer, vector analysis eliminated only one potential conduit whereas nine potential conduits were revealed by analysis of televiewer images from the Biscayne aquifer, with aperture measurements from a minimum of 1 cm to a maximum of 159 cm. Because of their potential for increased interconnectivity, conduits contribute large volumetric flow rates and the highly heterogeneous distribution of conductivity in karst aquifers (Atkinson, 1977; White, 2002). In order to compare pore geometries at three scales, conduits were removed from GIS layers because they did not contain true pore geometries. Eliminating conduits meant the largest scale features that account for a lot of the permeability and water flow were not included in pore shape analysis. Note, that the conduits were included in the calculation of overall porosity at the three scales of observation. Area and perimeter were the two geometric attributes derived from televiewer, core and thin-section images for use in this study.

In televiewer, core and thin-section images, macropores with the smallest areas have the

highest occurrence, intermediate pores occur at a moderately low frequency, while relatively large pores occur at the lowest frequency This observed exponential distribution holds true for corresponding pore perimeters in images from all three scales of observation.

After eliminating conduits, areas of macropores derived from televiewer images of the Castle Hayne and Biscayne aquifer are similar. However, pore perimeters derived from images of the Castle Hayne aquifer are nearly twice that of the Biscayne aquifer. In the Castle Hayne aquifer, intermediate-to-large macropores were interpreted as moldic pores that have coalesced to form larger pores. In contrast, pores with similar areas derived from televiewer images of the Biscayne aquifer could be described as non-fabric selective touching vugs owing to the simple structure of a vuggy pore. In the Castle Hayne aquifer, molds commonly form by dissolution through the selective leaching of aragonite shells (Thayer and Textoris, 1977). As dissolution continues, pores become enlarged and begin to interconnect. As moldic pores coalesce, the perimeters become higher than enlarging and interconnecting vugs with similar areas (Fig. 10a). It is expected that the shape index will increase at a similar rate to that of the perimeters and as expected (Fig. 10b). For pores with identical areas, macropores derived from the Castle Hayne aquifer are more complex than macropores derived from the Biscayne aquifer.

Comparable to the televiewer images, molds and vugs show similar pore areas in core images but the resulting mean pore perimeter for moldic pores calculated from core images is nearly twice that of the vuggy pores. As pore areas increase, the complexity of the pore shape index increases more dramatically in the Castle Hayne than for the Biscayne core images, even though pore areas are similar. At the intermediate scale of observation there were pores that intersected both sides of the image; these ‘conduits’ were not included in the geometry analysis but were included in overall porosity measurements. More of the coalesced pores were present in

the larger, more intact, Castle Hayne cores, probable due to poor core recovery from the Biscayne aquifer where drilling-induced disaggregation of vuggy intervals is common.

At the smallest scale of observation (thin-section), separate molds and vugs in both sets of thin-section images have very similar pore areas and perimeters. The result is nearly identical mean shape measures, which in both cases, indicates low complexity of pore shapes. Thin-sections are limited by their size and because of this; larger dissolution features were not observed at the smallest scale of observation. The complexity of shapes is also identical at smaller scales of observation for pores derived from both the Castle Hayne and Biscayne aquifers. However, as the scale of observation increases, the difference between the pore geometries of macropores from images of both aquifers increases. At each scale of observation, moldic pores are more complex than vuggy pores with identical areas (Fig. 10). As moldic pores become larger and coalesce through dissolution, they will become more complex in shape than coalescing vuggy pores of a similar area.

After quantifying pore geometries at three scales of observation, it becomes evident that the scale at which macropores are extracted is a critical factor in quantitative analysis. Figure 11 illustrates the distribution of pore attributes across the three-scales of observation between the two aquifers. In the box plots (Fig. 11), mean area and perimeters for both aquifers are in the upper percentiles of the data, believed to be a direct result of the large outliers distorting the results. The outliers are low in numbers but large enough in size to skew the mean values away from the median areas and perimeters. As the scale of observation increases, pore size increase considerably over several orders of magnitude. Therefore, when extracting pore attributes, it is most important to consider scale of observation because that will affect the size and distribution of pore structure.

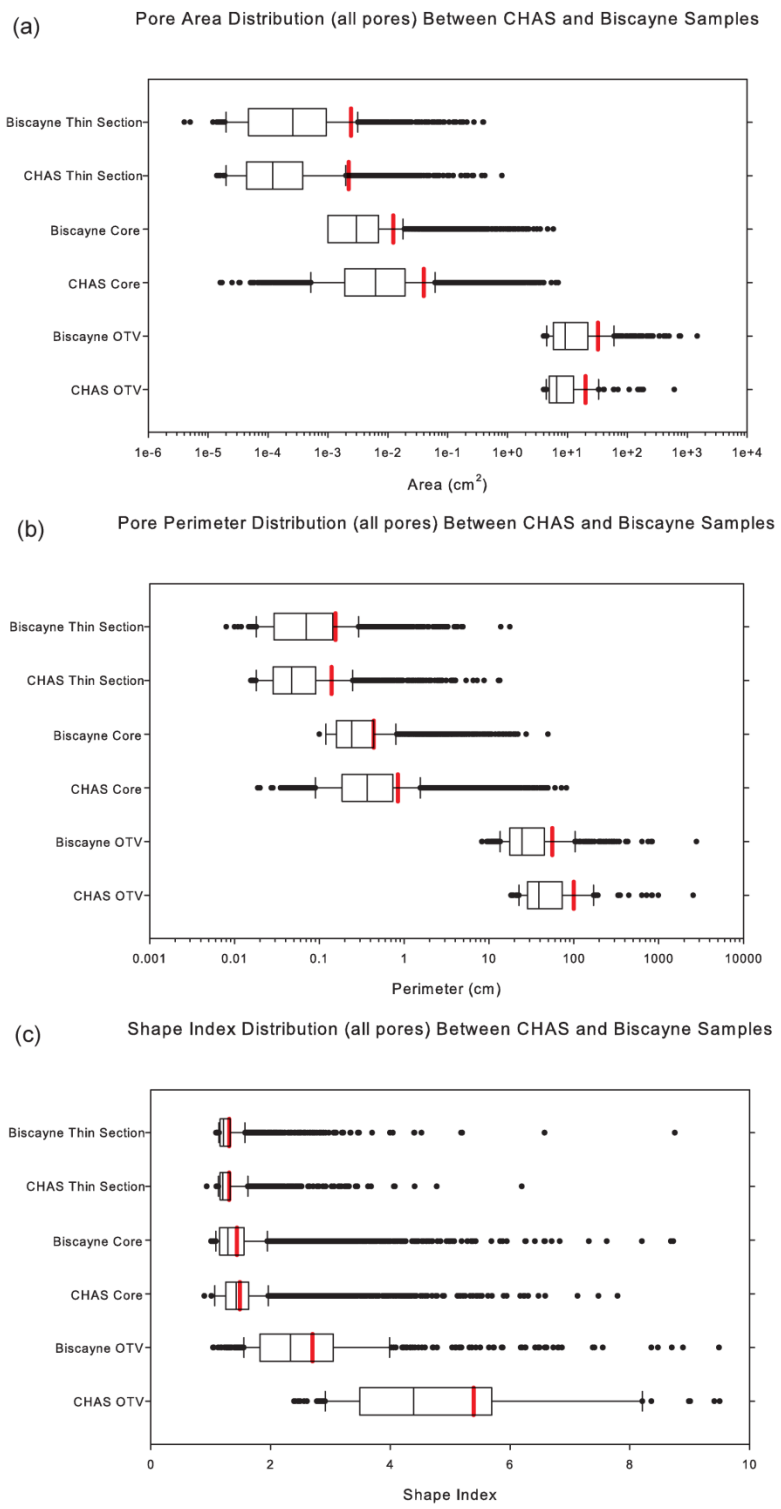

Figure 11. (a) Box plots of all pore areas found within Castle Hayne and Biscayne samples; (b) Box plots of all pore perimeters found within Castle Hayne and Biscayne samples; (c) Box plots of all pore shape indexes found within Castle Hayne and Biscayne samples. Red line equal to the mean value, upper/lower adjacents are 5/95% percentile, and upper/lower hinges are 25/75%. See Appendix D for statistics associated with this figure.

2.4.2 Implementing geospatial analysis for 2D porosity measurements

The mean porosity generated from the televiewer images falls within the ranges given by Cunningham et al. (2004a, 2004b) and Bolster et al. (2001) for the Biscayne and the ranges given by Winner and Coble (1989) and Thayer and Textoris (1977) for the Castle Hayne. In televiewer images, 'conduits' were included for the porosity calculation. With more conduits present in the Biscayne aquifer televiewer image the resulting porosity was higher than the Castle Hayne aquifer televiewer image, which has a smaller quantity of 'conduits'. The mean porosity obtained from televiewer images is a good estimate of aquifer scale porosity because the value is calculated from a continuous image that reflects the heterogeneous nature of karst aquifers more than just cores. This is most evident in Biscayne aquifer core images where porosity is calculated at approximately 23 percent. This is a significantly lower porosity than that generated from the televiewer image and is a direct effect of disaggregation of the vuggy intervals in which core recovery is low. As a result, cores analyzed were those found to be most intact, and therefore, least porous. Porosity from cores of the Castle Hayne aquifer was approximately 36%, which falls within Winner and Coble (1989) and Thayer and Textoris (1977) porosity ranges for the Castle Hayne aquifer.

GIS provides an alternative to traditional point-counts for identifying and calculating pore space, which can be imprecise for a variety of reasons (Demirmen, 1971). The overall, mean, porosity calculated from Castle Hayne thin-section images was approximately 40%, higher than the total porosity measured by Baum (1981) and Quinn (1988), who provided porosity estimates of 32 and 36%, respectively. The mean porosity generated from Biscayne thin-section images falls in the range of porosities for the Biscayne aquifer. All values are good

estimates of porosity at a particular scale but for overall aquifer porosity, the best estimate is porosity generated from largest-scale televiewer images.

2.4.3 Multi-scale geospatial analysis

As a result of the heterogeneous character of karst aquifers, hydraulic properties, including porosity, vary greatly as a function of scale (Whitaker and Smart, 2000; White 2006). Therefore, implementing a multi-scale, geospatial, porosity- and pore-structure analysis provides benefits which complement other techniques applied to karst formations, such as (1) Models which completely rely on laboratory-derived porosity and, (2) traditional, wire-line porosity logs (i.e. sonic, density, neutron, and magnetic resonance). Models for karst aquifers that rely solely on laboratory-derived measurements for porosity may provide misleading results because the quality of core recovered is usually extremely low when drilling in karst formations. Drilling can cause disaggregation of the highly vuggy zones, only allowing the most intact core to be recovered. The results will be a possible underestimation of the total porosity because larger solution features and highly vuggy zones are completely disregarded. Traditional wire-line logs offer continuous porosity readings, but fail to identify differences in macropore geometries with any level of precision when evaluating multiple formations, compared to that of vector image analysis (Manda and Gross, 2006b). The analysis presented in this paper is derived from a single well at each study site. Because of the limited data set, any inference as to the hydraulic significance of macropores at the aquifer scale is impracticable. Therefore, future work must involve applying the techniques outlined to multiple wells in each aquifer to account for the highly heterogeneous character laterally across karst formations.

2.5 Conclusion

Cunningham and Sukop (2011) concluded that the major challenge confronting the evaluation of groundwater flow in karst aquifers is characterizing and simulating the complex geometry of porosity networks. This research addresses their concerns of representing karst aquifer heterogeneity, by implementing a multi-scale approach to the quantitative investigation of pore structure and porosity.

This study presents an example of how quantitative measures of pore attributes and structure may be used to compare karst media with different porosity characteristics at multiple scales of observation. Using digital imaging and GIS spatial-analysis techniques to quantitatively characterize macropore structure and calculate porosity from the Castle Hayne and Biscayne aquifers, allowed for an unprecedented quantitative analysis of pore structure in karst aquifers. GIS provided the integrated environment for geospatial analysis without the need for programming, thus making it the ideal tool for identifying and extracting pore attributes from classified digital images of karst media. Thin-sections were limited by size and were often smaller than a single large macropore observed on a core image. Also, core analysis was largely dependent on quality of core recovery which was difficult in highly vuggy zones found in the Biscayne aquifer. Optical televiewers were ideal because they provided a continuous image of the borehole wall; therefore overcoming the difficulties which exist in analyzing large scale macropores utilizing thin-sections and cores. However, due to image resolution, smaller-scale macropores still significant to porosity were overlooked when only using optical televiewers for analysis. Thus, to truly quantitatively analyze, understand, and compare macropore structure within karst aquifers, multiple scales of observation must be included in analysis to overcome the unique challenges confronting the evaluation of groundwater flow in karst aquifers.

CHAPTER III: SUMMARY

3.1 Additional insight and application to groundwater management

This research presents the next step in the development of a more accurate quantitative understanding of porosity in karst media by comparing karst aquifers with different porosity characteristics using quantitative measures of pore attributes and structure. As more quantitative data are gathered about macropore structure, an enhanced understanding of the flow dynamics in karst aquifers can be attained. In order to effectively access current and future water demands and evaluate potential contamination using groundwater modeling, more refined modeling parameters, including porosity and pore geometry must be acquired.

Source-water protection and predictive strategies become exceedingly difficult when parameters used to model flow cannot fully appreciate the complex nature of karst media, especially when most data available comes from whole core or core plug samples representing a single scale of observation (Renken et al., 2008). Data from well tests and tracer tests are only adequate when attempting to completely characterize the complex internal flow structure in karst. In order to determine suitable parameters for modeling, Worthington (1999), suggests a comprehensive approach which integrates multiple sources of information, along with measurements of the porosity and permeability of unfractured rock.

Porosity is the percent of the volume of the rock that is open pore space, and primarily determines the amount of water that the rock can contain. On the other hand, permeability is a measure of the degree to which pore spaces are interconnected, and the size of the interconnections (Heath, 1970). Both porosity and permeability are dependent on the structure of the macropores present within the material. Low porosity usually results in low permeability, but high porosity does not necessarily imply high permeability. The multiple flow regimes (e.g.

conduit and interparticle) observed in both aquifers affect the porosity, but most importantly illustrate the exceptionally heterogeneous permeability found in karst terrains (White, 2002).

The research community is conscious of the fact that traditional Darcian-based, numerical, groundwater flow-models struggle to account for the non-Darcian, multi-porosity components of flow in karst aquifers (Taylor and Greene, 2001, Hill et al., 2010). Generally two types of groundwater flow are present in karst terranes, diffuse (slow, laminar flow) and conduit (rapid, turbulent flow). The slower diffuse flow occurs predominantly in primary openings, where conduit flow occurs generally in secondary openings (Mull et al., 1988). Worthington (1999) examined four karst aquifers across North America, and found that in all four cases approximately 90% of the aquifer storage is in the matrix and approximately 90% of the flow is in channels. Although flow through karst aquifers may be dominated by conduits where present, in the absence of conduits other fabric- and non-fabric selective porosity may dominate or in some cases porosity could occur in both forms where both are well developed (Martin and Dean, 1991).

Any information that assists in identifying the location and constraints of features that control fluid flow is highly sought-after. Cunningham et al. (2004b) and Manda and Gross (2006a, b) have pioneered the application of optical televiewers for identifying vuggy porosity and evaluating the spatial distribution and internal structure of karst conduits in southeastern Florida. Currently, researchers are applying innovative technologies to characterize the spatial distribution of porosity and permeability within the Biscayne aquifer to get beyond previous limitations in predictive simulation of groundwater flow (Cunningham and Sukop, 2011). Permeability in karst aquifers is exceedingly difficult to measure with traditional methodologies because a permeameter cannot account for multiple flow regimes. They are also unable to

measure large permeability values; therefore, the affects of conduits are poorly accounted for (Cunningham and Sukop, 2011). Traditionally applied to small-scale, computational modeling of fluid-flow, Lattice Boltzmann Methods (LBMs) have been integrated to overcome the challenges of modeling karst hydraulics in larger-scale characterization (Sukop et al., 2008). LBMs have the ability to simulate inertial flow, incorporate conduit geometries, and solve multiple flow regimes making it a particularly attractive tool for numerical modeling of flow in karst aquifers (Sukop et al., 2008). However, only preliminary research has been completed applying LBMs to borehole imagery from the Biscayne aquifer to simulate aquifer-scale groundwater flow (Sukop et al., 2008; Cunningham and Sukop, 2011).

The ability to use quantitative pore attributes and porosity measurements to characterize the spatial distribution of permeability and model groundwater flow across multiple scales of observation is the critical point in geospatial analysis of karst media in both the Castle Hayne and Biscayne aquifers.

3.2 Future work

This project has laid the groundwork for future researchers who wish to advance the quantitative understanding of hydraulic properties of the Castle Hayne aquifer. By converting optical televiewer, slabbed core, and thin-section images to a geospatial format, researchers can use these data to overcome the challenges facing of evaluating karst aquifers. The next step will be examining the quantitative relationship between porosity and permeability at multiple scales of observation. Advancing the understanding of hydraulic properties and the spatial distribution of porosity and permeability will undoubtedly improve modeling of groundwater flow by way of

more accurate quantitative input data with the ultimate goal of enhancing management of groundwater resources and evaluation of potential for contaminant transport.

3.3 Closing summary and conclusions

This study utilized digital imaging and spatial analysis techniques to quantitatively characterize and compare the geometry, distribution, and scaling properties of macropores from the Castle Hayne and the Biscayne aquifer at three scales of observation. This quantitative perspective of pore structures is achieved through a combination of image analysis techniques and GIS. The major advantage of using the Manda and Gross (2006b) image-processing procedures over other methods was the ability to integrate GIS for data extraction. This provided the environment for geostatistical and geospatial analysis without the need for programming which makes it the ideal tool for identifying and extracting pore attributes from classified digital images.

The image-processing techniques allowed study of the Castle Hayne aquifer using quantitative methods not yet utilized by previous researchers, and presented the first results of porosity extracted using an optical televiewer image. Also, no previous research has extracted moldic pore geometries from the Castle Hayne aquifer using classified images at multiple scales of observation. Performing a detailed quantitative assessment of macropore geometry and porosity on a vital aquifer here in eastern North Carolina allowed direct comparisons with another prolific karst aquifer – The Biscayne of southeastern Florida which has different structures and porosity.

Major observations of the project are as follows:

- Porosity derived from optical televiewer and thin-section images were similar between the two karst aquifers. The porosity from the optical televiewer images gave the best representation of the heterogeneous character of the aquifers.
- Porosity derived from core images of the Biscayne aquifer was significantly lower than porosity derived from core images of the Castle Hayne aquifer.
- Macropore areas and perimeters derived at all three scales of observation displayed exponential distributions.
- Moldic pores of the Castle Hayne aquifer had similar areas to vuggy pores of the Biscayne aquifer. However, the perimeters of the moldic pores were larger than the perimeters of vuggy pores.
- As the scale of observation increases, pore size increases considerably over several orders of magnitude.
- Conduits were present in optical televiewer images of both aquifers. However, more conduits were present in the images of the Biscayne aquifer compared to the images of the Castle Hayne aquifer.
- The largest pores in the Castle Hayne aquifer were associated with interconnecting moldic pores that were highly complex in shape. The largest pores in the Biscayne aquifer were associated with conduits and interconnecting vugs that were not as complex as the moldic pores from the Castle Hayne aquifer.

REFERENCES

Advanced Logic Technology Website, http://www.alt.lu

Anselmetti, F.S. and Eberli G.P., 1993, Controls on sonic velocity in carbonates, Pure and Applied Geophysics 141, Chapter 2-4, 287-323 p.

Anselmetti, F.S., Luthi, S.M., and Eberli, G.P., 1998, Quantitative characterization of carbonate pore systems by digital image analysis, AAPG Bulletin, Vol. 82, 1815-1836 p.

Atkinson, T.C., 1977, Diffuse flow and conduit flow in limestone terrain in the Mendip Hills, Somerset (Great Britain), Journal of Hydrology, Vol. 35, 93-110 p.

Bain, G.L., 1970, Geology and ground water resources of New Hanover County, North Carolina: North Carolina Department of Water and Air Resources, Ground Water Bulletin 17,79 p.

Bain and Palmer, Inc., 1987, Martin Marietta Aggregates Final Report: Dewatering of the Clarks Quarry. North Carolina. Department of Environmental Management

Baum, G.R., 1981, Lithostratigraphy, Depositional, Environments and Tectonic Framework of the Eocene New Bern Formation and Oligocene Trent Formation, North Carolina, Southeastern Geology, Vol. 22, 177-191 p.

Bourgeau-Chavez, L. L., Kasischke, E. S., Riordan, K., Brunzell, S. M., Nolan, M., Hyer, E. J., Slawski, J. J., Medvecz, M., Walters, T. and Ames, S., 2007, Remote monitoring of spatial and temporal surface soil moisture in fire disturbed boreal forest ecosystems with ERS SAR imagery, International Journal of Remote Sensing, Vol. 28, No. 10, 2133-2162 p.

Bolster, C.H., David, P.G., Saiers, J.E., 2001, Determination of specific yield for the Biscayne aquifer with a canal-drawdown test, Ground Water, Vol. 39, Iss. 5., 768-777

Campbell, J.B., 1996, Introduction to remote sensing (2nd Edition), Taylor and Francis, London

Chandra, A.M., Ghosh, S.K., 2005, Remote sensing and geographical information system, Alpha Science International Ltd., 250 p.

Choquette, P. W., and L. C. Pray, 1970, Geologic nomenclature and classification of porosity in sedimentary carbonates: AAPG Bulletin., Vol. 54, p.

Clémens, T.D. Hüchinghaus, R. Liedl and M. Sauter, 1999, Simulation of the development of karst aquifers: role of the epikarst. International Journal of Earth Science, Vol. 88, 157–162 p.

Cooke, C. W., Mossom, S., 1929, Geology of Florida: Florida Geol. Survey 20th Annual Report, 29-227 p.

Congalton, R.G., 1991, A review of assessing the accuracy of classifications of remotely sensed data. Remote Sensing of Environment. Vol. 37, 35-46 p

Cunningham K.J., Carlson J.L., Hurley N.F., 2004a, New method for quantification of vuggy porosity from digital optical borehole images as applied to the karstic Pleistocene limestone of the Biscayne aquifer, Southeastern Florida, Journal of Applied Geophysics, Vol. 55, 77–90 p.

Cunningham, K.J., Carlson, J.L., Wingard, G.L., Robinson, E., and Wacker, M.A., 2004b, Characterization of Aquifer Heterogeneity Using Cyclostratigraphy and Geophysical Methods in the Upper Part of the Karstic Biscayne Aquifer, Southeastern Florida: U.S. Geological Survey Water-Resources Investigations Report 03-4208, 66 p.

Cunningham, K.J., Sukop, M. C., Huang, H., Alvarez, P.F., Curran, H.A., Renken, R.A., and Dixon, J.F., 2009, Prominence of ichnologically influenced macroporosity in the karst Biscayne aquifer: Stratiform "super-K" zones: Geological Society of America Bulletin, Vol. 121, no. 1-2, 164-180 p.

Cunningham, K.J., Sukop, M.C., 2011, Multiple technologies applied to characterization of the porosity and permeability of the Biscayne aquifer, Florida: U.S. Geological Survey Open-File Report 2011–1037, 8 p.

Demirmen, F., 1971 Counting error in petrographic point-count analysis: A theoretical and experimental study, Journal of the International Association for Mathematical Geology, Vol. 3, 15-41 p.

DeWiest, R.J.M., Sayre, A.N., and Jacob, C.E., 1967, Evaluation of potential impact of mining on ground-water resources of eastern North Carolina: N.C. Department of Water Resources, 167 p.

Dreiss, S.J., 1982, Linear kernels for karst aquifer: Water resources research, Vol. 18, 865-876 p.

Dreiss, S.J., 1989, Regional scale transport in a karst aquifer, Component separation of spring flow hydrographs, Water Resources Research, Vol. 25, 117-125 p.

ERDAS, 2010a, ERDAS field guide, Atlanta, ERDAS Inc., 812 p.

ERDAS, 2010b ERDAS tour guide, Atlanta, ERDAS Inc. 950 p.

Fish, J.E., 1988, Hydrogeology, aquifer characteristics, and ground-water flow of the surficial aquifer system, Broward County, Florida: U.S. Geological Survey Water-Resources Investigations Report 87-4034, 92 p.

Fish, J.E., and Stewart, M.T., 1991, Hydrogeology of the surficial aquifer system, Dade County, Florida: U.S. Geological Survey Water-Resources Investigations Report 90-4108, 50 p.

Floyd, E.O., 1969, Ground-water resources of Craven County, North Carolina: U.S. Geological Survey Hydrologic. Investigation. Atlas HA-343

Friedman, G. M., 1959, Identification of carbonate minerals by staining methods: Journal of Sedimentary Petrology, Vol. 29, 87-97 p.

Gao, J., 2008 Digital analysis of remotely sensed imagery, First Edition: McGraw-Hill, Inc., 674 p.

Halihan, T.J, M. Sharp and R.E. Mace, 2000, Flow in the San Antonio segment of the Edwards aquifer: matrix, fractures, or conduits?, I.D. Sasowsky, C.M. Wicks, Editors , Groundwater flow and contaminant transport in carbonate aquifers, A.A. Balkema, Rotterdam, 129–146 p.

Heath, R. C., 1984, Ground water regions of the United States. United States Geological Survey Water Supply Paper 2242, 59 p.

Heath, R. C., 1987, Basic ground-water hydrology. U.S. Geological Survey Water-Supply Paper 2220.

Heath, R. C., H. B. Wilder, H. Peek, and P. Nelson, 1970, Groundwater Resources of North Carolina with emphasis on the basic principles of groundwater hydrology.

Hill, M. E., Stewart, M. T. and Martin, A., 2010, Evaluation of the MODFLOW-2005 Conduit Flow Process: Ground Water, Vol. 48: 549–559 p.

Hoffmeister, J.E. and Multer, H.G., 1968. Geology and origin of the Florida Keys. Geological Society of America Bulletin, 79: 1487-1502 p.

Jeannin, P.Y., 2001, Modeling flow in phreatic and epiphreatic karst conduits in the Holloch cave (Muotatal, Switzerland). Water Resources Research, Vol. 37, No 2 191–200 p.

Jenson. J.R., 1996, Introductory digital image processing: A remote sensing perspective, London, Prentice Hall International Inc., 381 p.

Klein, H., Armbruster, J. T., McPherson, B. P., and Freibergcr, H. J., 1975, Water and the south Florida environment: U.S. Geological Survey Water Resources Investigation 24-75 p.

Klein, H., Causaras, C.R., 1982, Biscayne aquifer, southeast Florida, and contiguous surficial aquifer to the north, in Franks, B.J., ed., Principal aquifers in Florida: U.S. Geological Survey Water-Resources Investigations Open-File Report 82-255 p.

Klein, H., Hull, J.E., 1978, Biscayne aquifer, southeast Florida: U.S. Geological Survey Water-Resources Investigations 78-107, 52 p.

Lautier, J.C., 1998, Hydrogeologic Assessment of the Proposed Deepening of the Wilmington Harbor Shipping Channel, New Hanover and Brunswick Counties, North Carolina, Department of Environment Health, and Natural Resources Division of Water Resources, 52 p.

Lautier, J.C. 2001. Hydrogeologic Framework and GroundWater Conditions in the North Carolina Central Coastal Plain. North Carolina Department of Environment and Natural Resources, Division of Water Resources, Raleigh, NC.

Legrand, H. E., 1960, Geology and Groundwater resources of Wilmington-New Bern area: North Carolina Department of Water Resources. Division of Ground water, Ground water Bulletin No.1, 80 p.

Lillestand, T.M., Kiefer, R.W., J.W. Chipman, 2004, Remote sensing and image interpretation, (5^{th} edition), John Wiley &Sons, New York

Lyke, W.L., and Treece, M.W., Jr., 1988, Hydrogeology and effects of ground-water withdrawals in the Castle Hayne aquifer in coastal North Carolina, in Lyke, W.L., and Hoban, T.J., Proceedings of the AWRA Symposium on Coastal Water Resources.

Lucia, F.J., 1995, Rock-fabric/petrophysical classification of carbonate pore space for reservoir characterization: American Association of Petroleum Geologists Bulletin, Vol.. 79, 1275-1300 p.

Lucia, F.J., 1999, Carbonate reservoir characterization: New York, Springer-Verlag, 226 p.

Mace, R. E., and Hovorka, S. D., 2000, Estimating porosity and permeability in a karstic aquifer using core plugs, well tests, and outcrop measurements, in Sasowsky, D.I., and Wicks, C. M., Groundwater flow and contaminant transport in carbonate aquifers: Brookfield, Vermont, A. A. Balkema, 93-111 p.

Manda, A.K. and Gross, M.R., 2006a, Estimating aquifer-scale porosity and the REV for karst limestones using GIS-based spatial analysis, in Harmon, R.S. and Wicks, C., eds., Perspectives on karst geomorphology, hydrology, and geochemistry - A tribute volume to Derek C. Ford and William B. White: Geological Society of America Special Paper 404, 177-189 p.

Manda, A.K. and Gross, M.R., 2006b, Identifying and characterizing solution conduits in karst aquifers through geospatial (GIS) analysis of porosity from borehole imagery: an example from the Biscayne aquifer, south Florida (U.S.A.): Advances in Water Resources, Vol. 29, 383-396 p.

Martin, J.B. and Dean, R.W., 2001, Exchange of water between conduits and matrix in the Floridan aquifer. Chemical Geology, Vo1. 79, No. 1–4, 145–165 p.

Mather, P.M., Magaly, K., 2011, Computer processing of remotely-sensed images: an introduction, (4th Edition), John Wiley and Sons, Inc, 434 p.

Mull, D.S., Liebermann, T.D., Smoot, J.L., and Woosley, L.H., Jr., 1988, Application of dye-tracing techniques for determining solute-transport characteristics of ground water in karst terranes. United States Environmental Protection Agency Region 4, Atlanta, Georgia, Publication EPA, 103 p.

Narkunas, James, 1980, Groundwater evaluation in the central Coastal Plain of North Carolina: North Carolina Department of Natural Resources and Community Development, 119 p.

Parker, G.G., 1951, Geologic and hydrologic factors in the perennial yield of the Biscayne aquifer: American Water Works Association Journal, Vol. 43, No. 10, 817-835 p.

Parker, G.G., Cooke, C. W., 1944, Late Cenozoic geology of southern Florida, with a discussion of the ground water: Florida Geol. Survey Bull. 27, 119 p.

Parker, G.G., Ferguson, G.E., Love, S.K., and others, 1955, Water resources of southeastern Florida, with special reference to the geology and ground water of the Miami area: U.S. Geological Survey Water-Supply Paper 1255, 965 p.

Quinn, J., 1998, Porosity of the Castle Hayne Limestone (Eocene), southern New Hanover County, North Carolina, Unpublished Masters Thesis, Wilmington, University of North Carolina, 91 p.

Renken, R. A., K. J. Cunningham, A. M. Shapiro, R. W. Harvey, M. R. Zygnerski, D. W. Metge, and M. A. Wacker (2008), Pathogen and chemical transport in the karst limestone of the Biscayne aquifer: 1. Revised conceptualization of groundwater flow, Water Recourse Research., 44 p.

Richards, H.G. 1950, Geology of the Coastal Plain of North Carolina. Transactions of the American Philosophical Society. Vol.. 40, No. 1

Rogan, J. S.. Yool R , 2001 Mapping fire-induced vegetation depletion in the Peloncillo Mountains, Arizona and New Mexico, International Journal of Remote Sensing ,Vol. 22, Iss. 16

Sanford, S., 1909, The topography and geology of southern Florida: Florida Geol. Survey 2nd Annual Report, 175-231 p.

Scanlon, B.R., Mace, R.E., Barret, M.E., and Smith, B., 2003, Can we simulate regional groundwater flow in a karst system using equivalent porous media models? Case study, Barton Springs Edwards aquifer, USA: Journal of Hydrology Vol.. 276, 137–158 p.

Schroeder, M.C., Klein, Howard, and May, N.D., 1958, Biscayne aquifer of Dade and Broward Counties, Florida: Florida Geological Survey Report of Investigations 17, 56 p.

Sellard, E. H., 1919 Geologic section across the Everglades of Florida: Florida Geol. Survey 12th Annual Report, 67-76 p.

Smith, D.G., George E.D. and Brenton, P.L. 1996, Water resources data North Carolina water year 1995, Ground-Water Records. U.S. Geological Survey Water-Data Report NC-9502, Vol. 2

Smith, G., Askne, J., 2001, Clear-cut detection using ERS interferometry, International Journal of Remote Sensing, Vol. 22, No. 18, 3651-3664 p.

Smith, B., Scanlon, B., 2003, Applications and Limitations of Numerical Modeling of Karst Aquifers. Proceedings from the International Conference on Karst Hydrogeology and Ecosystems: Bowling Green Kentucky.

Smith, B. Hunt, B., Jones, I, Lindgren, R., and Schindel, G. 2005, Ground-Water Availability Modeling of the Three Major Segments of the Edwards Aquifer, Central Texas." Abstract Book of the 2005 Ground Water Summit Program: NGWA. San Antonio, Texas, 232-233p.

Sukop, M.C., Anwar, S., Lee, J.S., Cunningham, K.J., and Langevin, C.D., 2008, Modeling ground-water flow and solute transport in karst with Lattice Boltzmann methods, *in* Kuniansky, E.L., ed., Proceedings of the U.S. Geological Survey Karst Interest Group Workshop, May 27-29, 2008, Bowling Green, Kentucky: U.S. Geological Survey Scientific Investigations Report 2008-5023, 77-86 p.

Taylor, J.C., Greene E. 2001. Quantitative Approaches in Characterizing Karst Aquifers: U.S. Geological Survey Karst Interest Group Proceedings. Water Resources Investigations Report 01–401: U.S. Geological Survey Karst Interest Group Proceedings, St. Petersburg, Florida, February 13-16, 2001., Atlanta , Georgia, 164–166 p.

Thayer, P.A., D.A. Textoris, 1972, Petrology and diagenesis of Tertiary aquifer carbonates, North Carolina: Transactions, Gulf Coast Assoc. of Geological Societies 22: 257-265 p.

Thayer, P.A., D.A. Textoris, 1977, Faunal and diagenetic controls of porosity and permeability in Tertiary aquifer carbonates, North Carolina. Special publication 7. North Carolina. Department of Natural and Economic Resources. Geology and Mineral Resource Section, 1-35 p.

Vacher, H. L., and Mylroie, J. E., 2002, Eogenetic karst from the perspective of an equivalent porous medium, Carbonates and Evaporites, Vol. 17, No. 2, 182-196 p.

Verbyla, D.L.,2002. Practical GIS Analysis, Taylor & Francis, London, 161 p.

Ward, L. W., Blackwelder, B. W., 1980, Stratigraphy of Eocene, Oligocene, and lower Miocene formations – Coastal Plain of the Carolinas: Excursions in Southeastern Geology Vol. 1, 190-207 p.

Ward, L. W., Lawrence, D. R., and Blackwelder, B. W., 1978, Stratigraphic revision of the middle Eocene, Oligocene, and lower Miocene-Atlantic Coastal Plain of North Carolina: U. S. Geological Survey Bulletin 1457-F, 23 p.

Wen, C. G., and Tateishi, R, 2001, 30-second degree grid land cover classification of Asia. International Journal of Remote Sensing. Vol. 22, No. 18, 3845-3854 p.

Whitaker F.F., Smart P.L., 2000 Characterizing scale-dependence of hydraulic conductivity in carbonates: evidence from the Bahamas. Journal of Geochemical Exploration 69–70, 133–137 p.

White, W.B., 1988, Geomorphology and Hydrology of Karst Terrains, Oxford University Press, New York, 464 p.

White, W.B. 2002, Karst hydrology: recent developments and open questions. Eng Geol, 65 2–3, 85–105 p.

White W.B. 2006 Fifty years of karst hydrology and hydrogeology: 1953–2003. In: Harmon RS, Wicks C (eds) Perspectives on karst geomorphology, hydrology, and geochemistry: a tribute volume to Derek C. Ford and William B. White. Geologic Society of America Special Paper 404, 139–152 p.

Wilkens, R.H., Fryer, G.J., and Karsten, J., 1991, Evolution of porosity and seismic structure of upper oceanic crust: importance of aspect ratios. .Journal of Geophysical Research, Vol., 17981-17995 p.

Williams, J. H., Carole D.J., 2004, Acoustic and optical borehole-wall imaging for fractured-rock aquifer studies, Journal of Applied Geophysics, Vol. 55, Iss. 1-2, 151-159 p.

Winner, M.D. and R.W. Coble, 1989, Hydrogeologic framework of the North Carolina Coastal Plain aquifer system, U.S.G.S. Open-File Report 87-690.

Winner, M.D., and R.W. Coble. 1996. Hydrogeologic Framework of the North Carolina Coastal Plain. U.S. Geological Survey Professional Paper 1404-I: p. 123-127.

Woods, T.L., Fullagar, P.D., Spruill, R.K. and Sutton, L.C. ,2000, Strontium Isotopes and Major Elements as Tracers of Ground Water Evolution: Example from the Upper Castle Hayne Aquifer of North Carolina, Ground Water, Vol. 38, 762-771 p.

Worthington S.R.H.,1999, A comprehensive strategy for understanding flow in carbonate aquifers. In: Palmer AN, Palmer MV, Sasowsky ID (eds) Karst modeling. Symposium proceedings, Charlottesville, Karst Water Institute, Special Publication 5, 30–37 p.

Worthington S.R.H., Davies G.J., Ford D.C., 2000, Matrix, fracture and channel components of storage and flow in a Paleozoic limestone aquifer. In: Sasowsky ID, Wicks CM (eds) Groundwater flow and contaminant transport in carbonate aquifers. A.A. Balkema, Rotterdam, 113–128 p.

Zhou, Q., Robson, M. 2001, Automated rangeland vegetation cover and density estimation using ground digital images and a spectral-contextual classifier, International Journal of Remote Sensing Vol. 22, Iss. 17, 3457-3470 p.

APPENDIX A: CASTLE HAYNE AQUIFER SYSTEM BACKGROUND

Location and Setting

Spanning approximately 12,500 square miles the CHAS is the most productive aquifer in the eastern North Carolina Coastal Plain, providing withdrawals upwards of 140 million gallons of water per day (Lyke and Treece, 1988). In Craven County the CHAS is used for various industrial and agricultural purposes, while the majority of potable water for municipal and domestic use is supplied by the Cretaceous aquifer system. Investigation within Craven County of the CHAS focused on an area north of the City of New Bern, including the inactive Martin Marietta Glenburnie quarry (Fig. 12). The Martin Marietta Glenburnie property is currently owned by the City of New Bern. The now abandoned excavation pits are currently filled with water. A majority of the surrounding area is natural wetlands with some residential development to the west and south of the property.

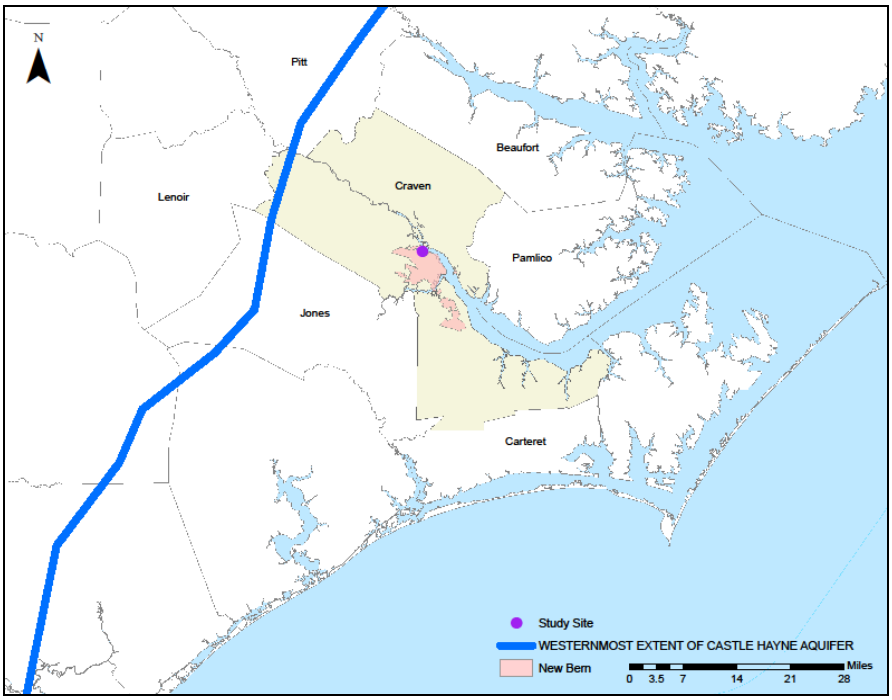

Figure 12. Map of eastern North Carolina showing the aerial extent of the Castle Hayne aquifer and study site in Craven County. (Westernmost extent of Castle Hayne aquifer North Carolina Modified from Woods et al. 2000).

Previous Studies

Investigation into the hydrogeologic framework beneath Craven County, and collection of data on the CHAS has been ongoing for well over 60 years. The groundwater system surrounding the Wilmington-New Bern area was initially investigated in a study by Legrand (1960) in which he described the underlying geology and identified the Castle Hayne aquifer as a major groundwater resource. Heath et al. (1970) published early work investigating the basic geology, hydraulic properties, and water chemistry of the CHAS found in the Coastal Plain of North Carolina. At the same time (Bain 1970) had conducted a comprehensive investigation of the hydrogeology of New Hanover County (South of Craven County) in which he described in detail the lithology, thickness, lateral occurrence, hydraulic characteristics, water levels, and water quality of the Castle Hayne limestone aquifer and surrounding units.

These researchers focused primarily on the hydrologic character of the aquifer, omitting detailed petrologic information, until Thayer and Textoris (1972 and 1977) published articles providing insight into petrology, diagenesis, and depositional environments of the limestone units. Based on outcrops at the former Superior Stone Company Quarry (Martin Marietta Glenburnie) in New Bern, their research revealed that the Castle Hayne Limestone is Middle to Upper Eocene in age. Thayer and Textoris (1972) subdivided the Castle Hayne into three major units and estimated porosity and permeability values for each.

Ward and Blackwelder (1980) further evaluated the Castle Hayne Formation exposed in outcrops in the Martin Marietta Glenburnie quarry (Fig. 14). Bain and Palmer (1987) later investigated the hydraulic properties of the CHAS, determining thicknesses and various aquifer parameters such as hydraulic conductivity, transmissivity, and storativity values.

Study Area Geology

The North Carolina Coastal Plain (40,000 km² in area) (Fig 13) is underlain by a gently eastward dipping, and eastward thickening sedimentary wedge composed of sand, clay, silt, limestone, and shell material. The marine and transitional sedimentary deposits that overlie the Pre-Cambrian crystalline basement range in age from Late Cretaceous to Pliocene (Legrand, 1960; Winner and Coble, 1996). The thickness of the sedimentary wedge ranges from zero along the Fall Line to more than 10,000 feet at Cape Hatteras (Richards, 1950).

From bottom to top, the geologic formation present in the subsurface of the New Bern area of Craven County are the Cretaceous Cape Fear, Black Creek, and Peedee, the Paleocene Beaufort, the Eocene Castle Hayne, the Oligocene River Bend, and the Pliocene Yorktown formations (Table 2). The most pertinent formations to this project are the River Bend and the Castle Hayne formations.

Thayer and Textoris (1972 and 1977), along with Ward and Blackwelder (1978 and 1980), provided comprehensive description of the geologic units exposed inoutcrops from the former Superior Stone Company quarry, now inactive Martin Marietta Glenburnie quarry, northwest of the City of New Bern (Fig. 4). The studies indicated that the thick Castle Hayne limestone sequence was deposited in a low energy, shallow, tropical, marine basin by a middle Eocene transgressive sea. Ward and Blackwelder (1978) redefined the limestone portion of the Castle Hayne formation as a size-sorted, cross-bedded, bryozoan hash and divided the unit into three members based on facies relationships, and petrologic and faunal evidence. The three new members to the Castle Hayne Formation defined by Ward and Blackwelder (1978) are: New Hanover Member, Comfort Member, and Spring Garden Member.

Geologic interpretations of the study area, according to Ward and Blackwelder (1980), and including the redefined Castle Hayne Formation are summarized as follows:

- The New Hanover Member consists of cobble to pebble sized, sandy, calcareous clasts, generally sub-rounded to well-rounded, and contains molluscan molds of nautiloid cephalpods, gastropods, along with various other bivalve species.
- A sharp contact allows the New Hanover Member to be easily delineated from the underlying Peedee Formation, a gray mold and cast siliceous limestone.
- The abrupt, uneven contact between the New Hanover Member and overlying Comfort Member, a bryozoan-echinoid bicalcarenite is easily distinguishable.
- The Comfort Member unconformably overlies the New Hanover Member throughout the region.
- The Spring Garden Member in Craven County is a tan to gray sandy, molluscan-mold biocalcirudite, it is most prevalent in the study area surrounding the Martin Marietta quarry in New Bern, where up to 6 meters of the limestone is exposed.
- The upper surface of the Spring Garden Member is a thin phosphate layer containing Oligocene aged oysters and barnacles which serves as the contact between the base of the River Bend Formation.
- The River Bend Formation consists of molluscan-mold biocalcirudite ranging in age from middle Oligocene to late Oligocene interpreted to be an inner shelf deposit that formed below wave base.
- The River Bend Formation overlies the Eocene Castle Hayne Formation at the Martin Marietta quarry in New Bern.

Hydrologic properties

The term CHAS collectively combines all aquifers present in the Castle Hayne, River Bend, and Beaufort Formations, creating the single most productive aquifer in eastern North Carolina (Winner and Coble, 1989). However in the study area below the Martin Marietta Quarry in New Bern the Castle Hayne aquifer consists of the Castle Hayne and River Bend Formation and generally described as a sandy, molluscan-mold limestone. The Castle Hayne aquifer can be further subdivided into upper and lower portions. The upper portion of the aquifer is dominated by moldic limestone and the lower portion aquifer is dominated by sand. This upper limestone portion of the aquifer commonly has much higher porosity and permeability then the lower portion because of dissolution and further enlargement of pore space (Winner and Coble, 1989; Thayer and Textoris, 1977). Geophysical work below Craven County generally shows decreasing permeability towards the base of the aquifer due to introduction of more continuous clay layers. (Winner and Coble, 1989). The upper portion moldic limestone higher zones of porosity and permeability are attributed to diagenetic processes.

Thayer and Textoris (1972) listed four major diagenetic processes found in the upper moldic limestone: 1) aragonites converting to low-Mg calcite, 2) solution of aragonitic pelecypod and gastropod shells to form molds, 3) solution and enlargement, and 4) infilling with low-Mg calcite spar. Thayer and Textoris (1977) also suggest that the primary packing of shells and the amount of infilling of calcite controls the porosity and permeability.

Thayer and Textoris (1977) using rock slab samples collected from the near 30ft of exposed limestone outcrops at the New Bern quarry subdivided the Castle Hayne Limestone (CHL) into three major units major units (from base upward): The first unit comprises sand, pelecypod-mold biomicudite with pseudospar matrix. The second unit comprises sandy,

pelecypod-mold biosparite and biosparrudie. The third unit consists of sandy, pelecypod-mold biomicrudite with pseudospar matrix. The porosities and permeabilities for each unit of the CHL from base upward are : 1) porosity in the first unit ranges from16-30 percent (mean porosity = 25 percent), whereas permeability ranges from 1.97 x 10^{-10} m^2 to 1.18 x 10^{-6} m^2) porosity in the second unit ranges from 9-25 percent (mean porosity = 17 percent), whereas permeability ranges from 9.73 x 10^{-9} m^2 to 1.70 x 10^{-6} m^2 ;3) porosity in the third unit ranges from 30-42 percent (mean porosity = 34 percent) and permeability ranges from 1.96 x 10^{-7} m^2 to 5.14 x 10^{-6} m^2.

Narkunas (1980) completed a groundwater evaluation in the Central Coastal Plain and calculated transmissivity, storage coefficient, and specific capacity for the CHAS. Transmissivity was calculated from data collected during eleven aquifer test and ranged from 6,100 to 12,100 ft^2/day and averaged 8,700 ft^2/day. Storage coefficient ranged from 2.6 x 10^{-3} to 7.4 x 10^{-5} averaging 1.3 x 10^{-3} estimated based on data collected from two aquifer test. Using 24 hour pump test data from 20 six-inch wells specific capacity values calculated ranged from 0.61 gpm/ft to 22.73 gpm/ft and averaged 9.54 gpm/ft. Lautier (1998) performed similar aquifer tests indicating transmissivity ranges of 212 to 9930 ft^2/day and hydraulic conductivity ranges of .42 to 31 ft/day. Lautier (2001) also found that higher transmissivity and hydraulic conductivity values came where well screens were exclusively in the upper limestone portion of the aquifer and lower values came from well screens entirely in the lower non-limestone portion of the aquifer.

Recharge for the Castle Hayne aquifer occurs form of leakage through the overlaying confining beds, previous researchers have calculated recharge values as low as 200,000 (gal/day/mi^2) (Floyd, 1969) to as high as 382,000 (gal/day/mi^2) (DeWiest et al., 1969). Narkunas 1980 groundwater evaluation of the CHAS estimated recharge to average 240,000 (gal/day/mi^2).

System	Series	Stratigraphic Units	Hydrogeologic Units		Brief Description
Quaternary	Recent	Surfical Sediments	Surficial Aquifer		Sand, silt, shells, and some clay
	Pleistocene	Croatan Formation	Croatan		
Tertiary	Pliocene	Yorktown Formation	Yorktown		Interbedded silt, sand, and clay with shell beds
	Miocene	Pungo River Formation	Pungo River		Phosphate and quartz sand, silt, clay, and limestone
		Belgrade Formation			
	Oligocene	River Bend Formation	Castle Hayne Aquifer	Upper Castle Hayne	Moldic limestone containing calcite, quartz, glauconite, and dolomite with Interlayered calcareous sands
	Eocene	Castle Hayne Formation		Lower Castle Hayne	Shell limestone interbedded with calcareous sand
	Paleocene	Beaufort Formation		Beaufort	Fine glauconitic sand, silty, and sand
Cretaceous	Upper Cretaceous	Peedee Formation	Peedee		Interbedded clay, fine sand, and silt more calcareous in the Peedee
		Black Creek Formation	Black Creek		
		Cape Fear Formation	Cape Fear		
	Lower Cretaceous	Unnamed Deposits	Lower Cretaceous		
Mesozoic - Precambrian Basement Complex					

Table 2. General stratigraphy and hydrology of units in CHAS study area. (Modified from Lautier 1998, Narkunas 1980, Reynolds and Spruill 1995, Winner and Coble 1996).

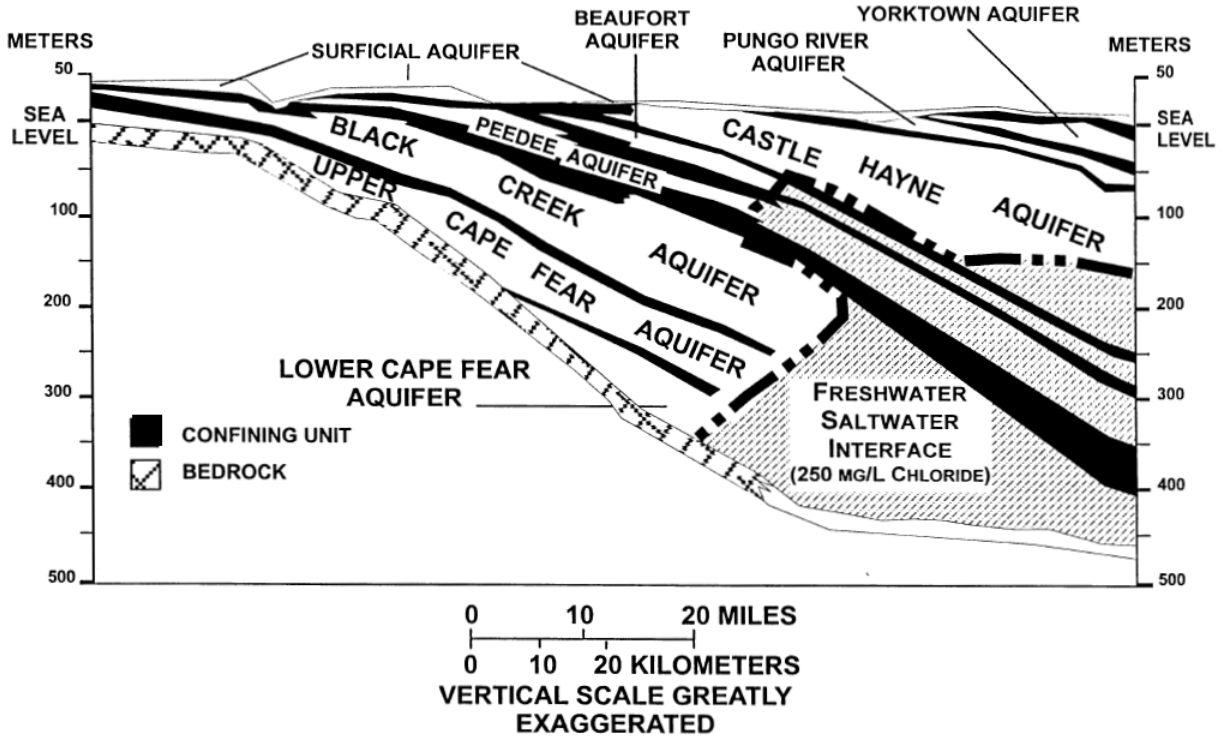

Figure 13. East-West cross section of hydrologic units including the Castle Hayne aquifer below Craven County (from Smith et al. 1996).

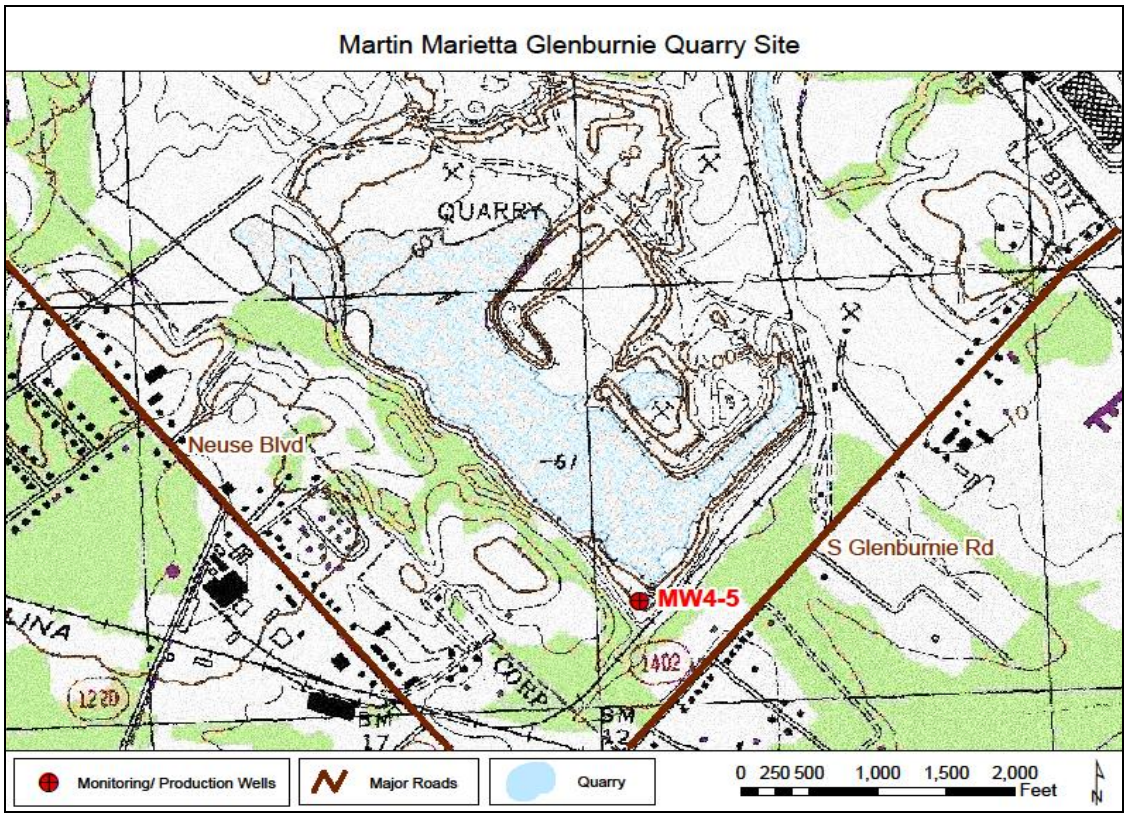

Figure 14. Topographic map of southeast corner of the former Martin Marietta Glenburnie Quarry showing general study area and well PW5 location.

APPENDIX B: BISCAYNE AQUIFER BACKGROUND

Location and Setting

The Biscayne aquifer spans approximately 6,437 square miles across Miami-Dade, Broward, Palm Beach, and Monroe Counties (Klein and Hull, 1978) and is the principal water supply for Miami, Boca Raton, Pompano Beach, Fort Lauderdale, Hollywood, Miami Beach, and Homestead. Major population centers are located in the coastal area of Miami-Dade and Broward counties, which are flanked by the Atlantic Ocean to the East and key agricultural and conservation areas associated with the Florida Everglades to the West (Fig. 15). The Biscayne aquifer underlies all major municipalities in the coastal region of southeast Florida and most of the Everglades up to the Broward-Palm Beach county line (Schroder et al. 1958).

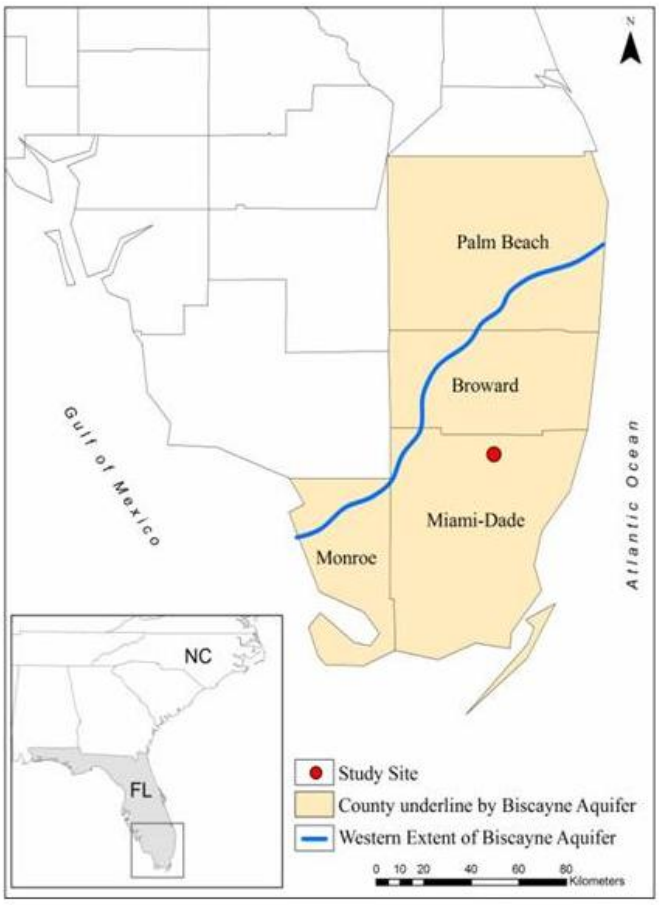

Figure 15. Map of southern Florida showing the aerial extent of the Biscayne aquifer and location of study site in northern Miami-Dade County, Florida

Previous Studies

In-depth studies of Dade and Broward counties began in the early 1900's when Sanford (1909) first described and named surficial limestones while investigating the basic surface geology of southeast Florida. As the United States Army Corp of Engineers began to dig new drainage canals across the everglades to supply water in order to facilitate population growth, Sellard (1919) collected the first data on geologic formations present in the subsurface. Cooke and Mossom (1929), using cored material from test wells, continued describing the limestone formations which contained freely circulating water. Parker and Cooke (1944) then provided geologic descriptions and correlations with discussion of groundwater occurrence.

The Biscayne aquifer was named and defined by Parker (1951) as the hydrologic unit of water-bearing rocks that carries unconfined ground water in southeastern Florida. As more comprehensive investigations continued on the Biscayne aquifer, Parker et al. (1955) re-defined the aquifer in further detail, naming and defining the following formations: (1) Tamiami Formation, (2) Caloosahatchee Marl, (3) Fort Thompson Formation,(4) Anastasia Formation, (5) Key Largo Limestone and, and (6) Pamlico Sand (Table 3). Parker et al. (1955) investigatedthe Biscayne aquifer and provided essential information on the occurrence, movement, and quality of water in the subsurface.

Schroeder et al. (1958), with the United States Army Corps of Engineers, drilled shallow test holes across Dade County and Broward County to provide additional description and contour the thickness of the Biscayne aquifer across the region. These descriptions have been continually modified and improved by more comprehensive studies of the Biscayne aquifer by Klein et al. (1975) and; Klein and Hull (1978). Other comprehensive ground water reports by Fish (1988) examine water quality, factors that affect water quality, hydraulic characteristics of the surficial

aquifer. Later, Fish and Stewart (1991) investigative report provided greater insight into not only the framework of the surficial aquifer but principal hydraulic characteristics and the distribution of these characteristics throughout the sediments. Fish and Stewart (1991) analyzed drill cores and aquifer- test data, and provided accurate hydraulic conductivity, specific capacities, and transmissivity in local areas to reveal trends and patterns of the surficial-aquifer system. Recently Cunningham el al. (2004b) combined tools such as ground-penetrating radar, borehole geophysical logs, cycolotratigraphy, imaging of karst features, and whole-core analysis allowing for high resolution profiling of geologic contacts and hydrogeologic units. Thus providing the most accurate and up to date assessment of the aquifers hydrogeologic framework.

Study Area Geology

The Southeast Coastal Plain is an area of about 212,000 km^2 predominantly in Florida, southern Georgia, Alabama, and South Carolina. Most of the area, including the southern peninsula of Florida is a nearly flat plain less than 10 meters above sea level (Heath, 1987). The peninsula of Florida is the exposed eastern portion of the Floridan Plateau which resembles a massive horst separating the Atlantic Ocean and the Gulf of Mexico (Parker et al. 1955). The igneous and metamorphic rock composing the core of the Floridan Plateau are overlain by unconsolidated deposits of Pleistocene age consisting of limestone, sand, gravel, clay, and shell beds that range in thickness from about 4,000 feet in central Florida to more than 15,000 feet in southern Florida (Parker et al. 1955). In southeastern Florida the subsurface is dominated by semi consolidated limestone and marl deposits associated with marine terraces that formed when the area was inundated by the sea at different times (Heath, 1984).

From oldest to youngest, the geologic formations found in the subsurface of southeastern Florida are the: Eocene age Lake City limestone, Avon Park limestone and Ocala limestone; Oligocene age Suwannee Limestone; Miocene age Tampa Limestone, Hawthorn formation, and Tamiami formation; Pliocene age Caloosahatchee marl, Fort Thompson formation, Key largo limestone, Anastasia formation, Miami Oolite, and Pamlico sand; Holocene age Lake Flirt marl (Parker et al. 1955) (Table 3). The full stratigraphic sequence given above is not present at any one place; the most relevant formations to this project will be the Miami limestone and Fort Thompson formation.

The Miami Limestone (formerly Miami Oolite) is described by Schroeder et al. (1958) as the surface rock that blankets nearly all of Dade County, parts of eastern and southern Broward County, and the southern mainland of Monroe County. Occurring not only on the mainland, the Miami limestone can be found in the southern keys from Big Pine Key to the Marquesas Keys (Hoffmeister and Multer, 1968). The northern extent of the Miami Limestone can be found in Palm Beach County, where it grades laterally northward into the Anastasia Formation. A visible contact between the Miami limestone and the underlying Fort Thompson formation can be found along numerous cut walls of everglades canals (Parker et al. 1955). Hoffmeister and Multer (1968) concluded the Miami limestone consists of two distinct faces, an oolitic facies and a broyozon facies. The oolite facies is typically a white-to-yellowish, massive, cross-bedded, oolitic limestone containing varying amounts of sand, usually in solution holes (Schroeder et al. 1958). Hoffmeister and Multer (1968) describe the bryozoan facies as, consisting of white to orange gray, poorly to well indurated, sandy, fossiliferous limestone, consisting of varying amounts of skeletal material including: corals, echinoids, mollusks, and alge.

Schroeder et al. (1958) identify the Fort Thompson Formation as the alternating fresh-water and marine limestone and marl bed which unconformably overlies the Tamiami Formation, or where present the Caloosachatchee marl and underlies the Miami limestone unconformably. The Formation is generally separated into two parts, based on the hydrologic characteristic of the rock. The northern portion of the formation which underlies the upper Everglades area to the northwest of Broward County is generally much lower in permeability. The southern portion of the formation in the Dade-Broward County area is composed of light gray to cream, fossiliferous, marine, sandy limestone, calcareous sandstone, with thin beds of hard freshwater limestone (Parker et al., 1955). Schroeder et al., (1958) and Parker et al., (1955) both note the marine limestone beds in formation have been most affected by solution activity from percolating ground water. The result of solution is a very highly permeable rock mass riddled with secondary solution cavities, as much as several feet in diameter. The solution cavities can also be found filled or partially filled with younger fine to medium quartz sand. A vast majority of fossils in the formation are not found in their original form, but instead preserved has molds and casts with secondary deposits of calcite crystals within the concavities of the shells (Schroeder et al., 1958).

Hydrologic properties

The Biscayne aquifer is currently defined by (Fish, 1988) as that part of the surficial aquifer system comprised of Pleistocene aged sediments (from land surface downward) of the Pamlico Sand, Miami Oolite, Fort Thompson Formation, Anastasia Formation, Key Largo Limestone as well as upper most permeable portions of the Pliocene Tamiami Formation (Fig.

17). According to Fish and Stewart (1991) these units collectively form an unconfined aquifer system which provides the majority of the potable water to southeastern Florida.

Fish and Stewart (1991) estimated transmissivity values averaging 300,000 ft^2/day, with values decreasing to less than 75,00 ft^2/day west of Dade County and over 900,000 ft^2/day to the southeast of Broward County . The extremely high transmissivity values are usually associated with thick section of the Fort Thompson formation within the aquifer. Hydraulic conductivities for the entire Biscayne aquifer range over seven orders of magnitude; from more than 10,000 ft/day for highly permeable marine limestones in the Fort Thompson to about 0.001 ft/day or less for dense, green clay of the Key Largo Formation (Fish and Stewart, 1991). Calculated values of specific capacity for production wells in Dade County range from just over 100 (gal/min)/ft up to 7,410 (gal/min)/ft (Fish and Stewart, 1991).

Fish (1988) reported porosities of samples determined by laboratory tests to range from 37 to 48%, while Manda and Gross (2006b) found core samples displayed a much wider range of porosities (10-48%). Similar to that of Cunningham et al., (2004a,b) with porosity measured from core samples ranging between 6% and 49% and analysis of digital borehole wall images produced a 5-45% range with occasional spike of 100% in larger solution cavities.

The average daily pumpage from the Biscayne aquifer in 1950 was estimated to be roughly 130 million gallons (Schroder et al., 1958). By 1975, daily pumpage of the surficial aquifer had already reached over 500 million gallons for public water-supply and another 165 million gallons daily for irrigation (Klein and Hull 1978). The unconfined aquifer is recharged primarily by precipitation and infiltration from canals that drain surface water directly from conservation areas developed in the Everglades (Heath, 1984).

Series	Geologic Units	Hydrogeologic Units	Brief Description
Holocene	Organic Soils	Semi-Confining Unit	Peat and Muck; water has high color content. Almost impermeable. Lake Flirt is shelly, calcareous mud.
	Lake Flirt Marl		
Pleistocene	Pamlico Sand	Biscayne Aquifer	Quartz sand; water high in iron Small yields to domestic wells.
	Miami Limestone		Sandy oolitic limestone, large yields.
	Fort Thompson Formation		Alternating marine shell beds and freshwater limestone. High permeability. Large yields
	Anastasia Formation		Coquina reef rock. Large yields.
	Key Largo Limestone		Caralline reef rock. Large yields.
	Caloosahatchee Marl		Sand, shell, silt, and marl. Moderate yields
Pliocene	Tamiami Formation	Semi-Confining Unit	Limestone, clay, and marl. Occasional Moderate yields in upper few feet. Remainder forms upper part of basal confining unit.

Table 3. Generalized stratigraphic and hydrologic units of the Biscayne aquifer (modified from Klein and Causaras, 1982; Fish and Stewart, 1991).

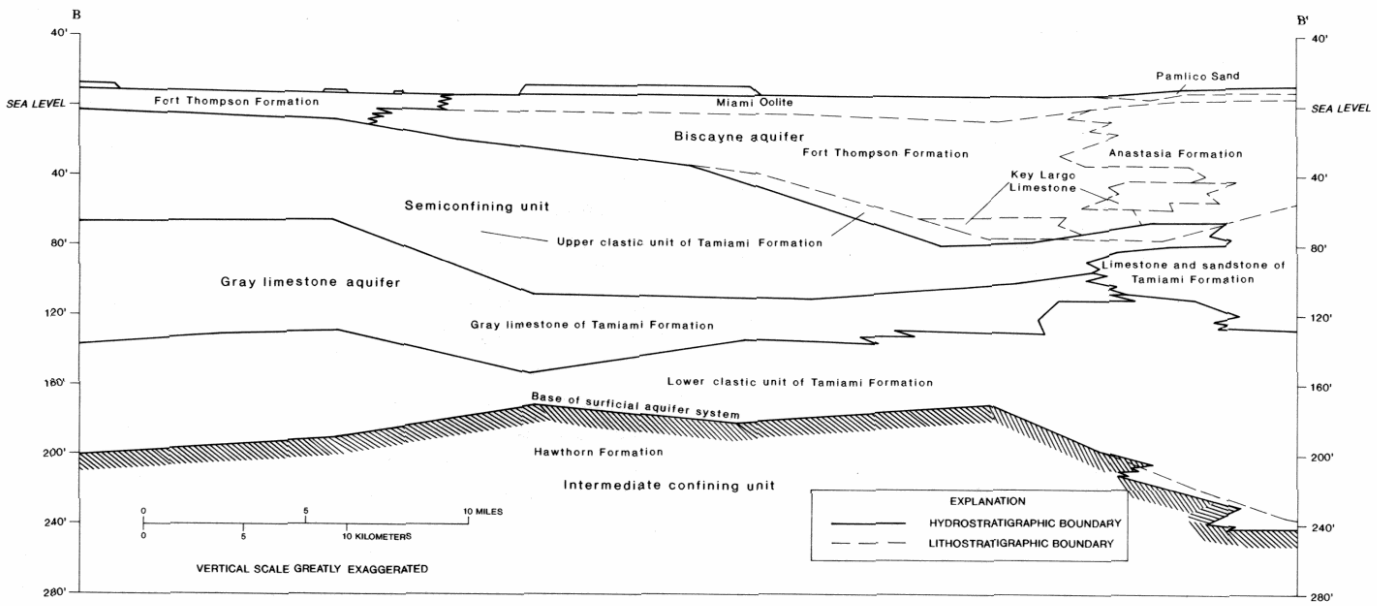

Figure 19. Generalized cross section of Biscayne aquifer in central Miami-Dade County (from Fish and Stewart, 1991)

APPENDIX C: METHODS OF ANALYSIS

Data Acquisition

In early 2000, in an effort to better understand and characterize the stratigraphy and hydrogeology of the Biscayne aquifer, the United States Geological Survey (USGS) drilled two wells (FPL1 and FPL2) at a study site in northern Miami-Dade County. Onsite geologists collected caliper, gamma, full-waveform sonic (FWS), resistivity, acoustic and optical televiewer logs in each well. The USGS provided optical televiewer logs and cores collected from FPL1 to the 2004 Florida International University research project in which, Alex Manda and Michael Gross successfully converted optical televiewer images (Appendix E) and core images (Appendix F) into a classified binary format. The binary images were used as source images in a GIS for accurate data extraction and spatial analysis. Though not analyzed in the 2004 research project, thin sections were created from the core retrieved at well FPL1; which Alex Manda has generously provided for use in this project. In order to compare the CHAS at three scales of observation, to the Biscayne aquifer data set collected from well FPL1, a CHAS study site had to be selected based on the ability to provide optical televiewer images, slabbed core, and thin sections from a single well.

In the late 1990's, a City of New Bern project was designed to predict the hydrologic implications of disposing 4 to 6 mgd of tertiary-treated wastewater effluent into the former Martin Marietta Glenburnie Quarry with the goal of using the groundwater system as a natural infiltration system. In order to develop an understanding of the hydrogeologic framework underlying the quarry, 17 pumping and observation wells were installed throughout the site. After the wells were drilled, onsite geologist recovered core and collected resistivity and gamma geophysical logs for each well. CHAS research will focus principally on one production well (PW5), which is a six-inch open borehole well, located in the southeast corner of the Martin

Marietta Glenburnie Quarry (Fig. 15). Returning to the Martin Marietta Glenburnie quarry site in July of 2010, ECU geologists ran caliper, resistivity, temperature, heat pulse, downhole video, and optical televiewer logs on well PW5 (Fig. 18). Optical televiewer logs were particularly valuable as they supply the most detailed information by allowing for direct viewing of the inside of the well bore from high resolution digital images (ALT). Analogous processing techniques used in successfully generating binary images from optical televiewer images of the Biscayne aquifer were applied to optical televiewer images of the CHAS, this in turn allowed for a direct comparison of lithologic features from borehole images in each system.

Figure 18. Alex Culpepper (left) and field assistant Nick Desimone (right) lowering OBI-40 optical televiewer in well (PW5) at Martin Marietta Glenburnie Quarry.

In 2001, Dr. Richard Spruill provided the core collected from well PW5 during the 1998 City of New Bern groundwater investigation to East Carolina University for graduate research and petrographic analysis. The PW5 core was slabbed and thin sections were produced at 0.5m intervals between depths of 37.5 to 43.5 feet and 60 to 62 feet, orientated both parallel and perpendicular to bedding. Use of these previously collected cores and thin sections in conjunction with the optical televiewer images of well PW5 provided the three scales of observation from a single well in which to compare to the Biscayne FPL1 well.

Slabbed PW5 core samples were photographed with a Nikon D300 digital camera (Fig.19 and 24; Appendix G) and carefully processed using similar methods to those implemented in Manda's 2004 successful analysis of slabbed Biscayne core collected from well FPL1. Collecting and processing the CHAS PW5 core images using methods similar to those employed by previous researchers allowed for direct comparison of the binary images in a GIS with previously analyzed Biscayne core images.

Thin sections had been created by previous researchers from both CHAS (PW5) core and Biscayne (FPL1) core but neither had previously been photographed or processed. In order to quantitatively compare binary thin sections images in a GIS; photographs of Biscayne (FPL1) thin sections (Appendix H) and CHAS (PW5) thin sections (Fig. 20; Appendix I), photographs were taken with a Nikon D300 digital camera and processed in the same way as optical televiewer and core images. As a result, the complete data set contains information from three scales of observation; optical televiewer, slabbed core, and thin section images for both the Biscayne and CHAS. This section describes the methodology and tools implemented in converting optical televiewer, core, and thin sections into a GIS appropriate format for data extraction and spatial analysis.

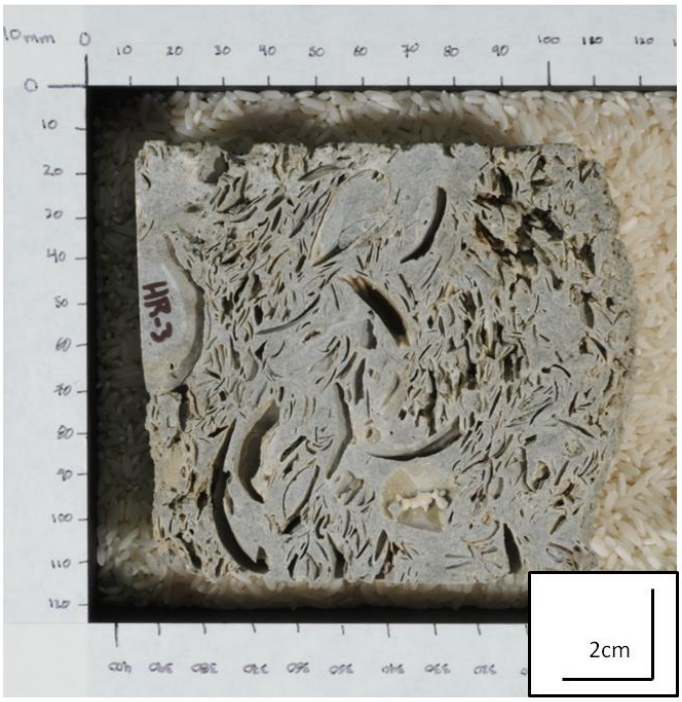

Figure 19. Example of CHAS core after being sawed in half to give a cross sectional view of the rock.

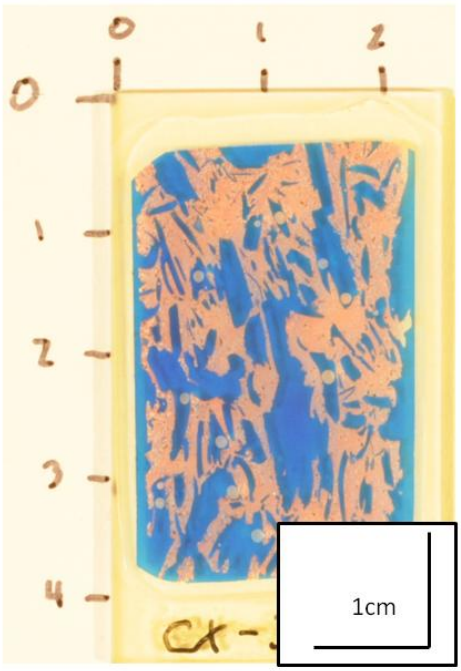

Figure 20. Example of CHAS thin section used in analysis.

Tools and software packages employed

Imaging with optical televiewers is most frequently employed in the study of fractured-rock aquifers where the continuous and orientated 360° images of the borehole wall allow for greater ease in defining the character, relation, and orientation of lithological and structural features (Williams and Carole, 2004). More recently, imaging with optical televiewers in limestone aquifers has been employed because the optical images that allow for direct viewing of the borehole wall character can be exported to more robust software programs allowing for detailed analysis of lithological and structural information (Manda and Gross 2006b). The OBI-40 slimhole optical televiewer (OTV) (Fig. 21) manufactured by Advanced Logic Technology (ALT) of Luxemburg (ALT Website) is the latest and most powerful tool used to obtain optical images of borehole walls.

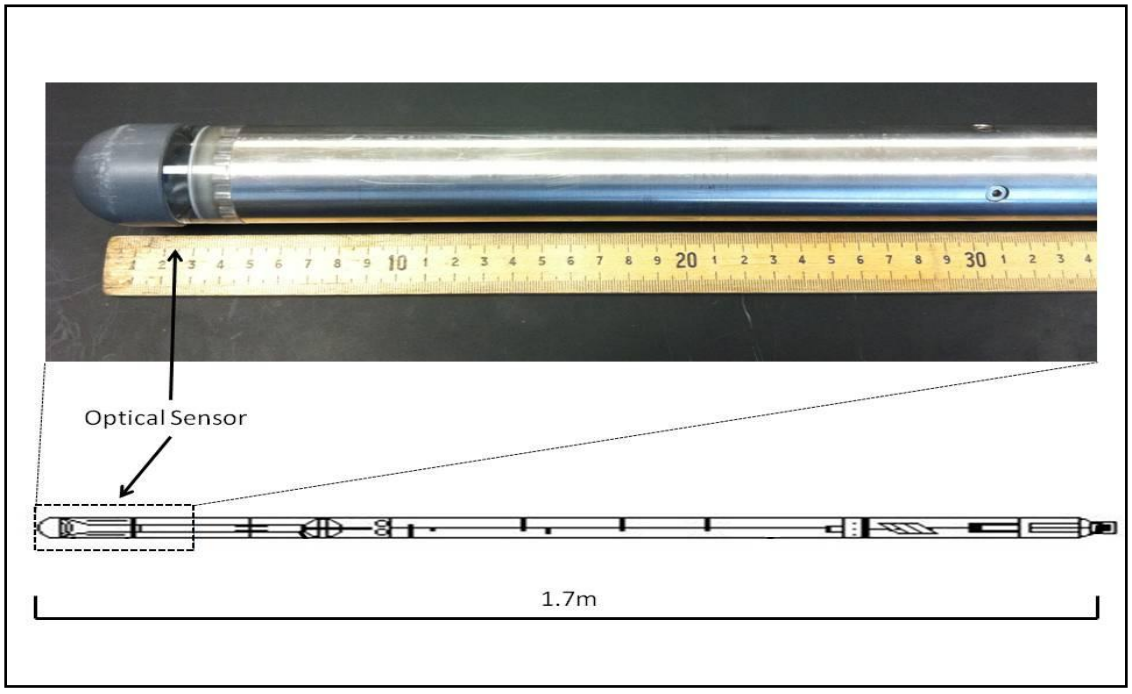

Figure 21. OBI 40 slimhole optical telviewer (developed by ALT) used to generate a continuous and orientated 360° color image of the borehole wall.

The approximate length of the OBI 40 is 1.7m, diameter is 40mm, and its approximate weight is 7 kilograms. The tool consists of a ring of LED lights used to illuminate the borehole, a charged coupling device (CCD) camera, and conical reflector housed in a transparent cylindrical window.

The conical prism system on the tool focuses a 360° slice of the borehole wall into the lens of the charge-coupled device (CCD) camera which measures the intensity of the color spectrum in red, green, and blue (RGB). The optical image scan is digitized downhole then sent up the logging cable as digital signal. Vertical and horizontal resolutions are user-defined at the time of logging, with vertical set to depth (e.g. 0.5, 1, or 2mm) and horizontal set to 180, 360, or 720 pixels per line. For the CHAS PW5 image, the vertical and horizontal resolutions were set to 1mm and 720 pixels/360° respectively. For both Biscayne FPL1 and FPL2 images, the vertical and horizontal resolutions were .3mm and 720 pixels/360°. The logging speed for OTV images is dependent on the selected vertical and horizontal, cable type, and system design (Williams and Johnson, 2000).

Typical logging speeds for most systems range from 1m/min to no more than 3m/min for 1mm and 720 pixels per line data. OTV logging of PW5 was run at a constant 0.8m/min. Within the tool, a three-axis magnetometer and three accelerometers permit borehole wall images to be orientated providing true three-dimensional location of measurement. OBI-40 slimhole OTV has the ability to accurately image boreholes ranging in size from 1.75” to 24” depending on borehole conditions (ALT website).

The East Carolina, geophysical, logging trailer is equipped with the most current Mount Sopris Instrument/Advanced Logic Technology (MSI/ALT) MARIX acquisitions systems, widely considered the industry standard in slim line borehole geophysical logging equipment (Fig. 22). The 4MXA-1000 winch system manufactured by MSI is spooled with 500m of 0.125’

single-conductor wireline which acts as the data conduit between the sonde and data collector. The winch has the ability to supply precise depth records of the sonde using an optical encoder attached to the sheave wheel. The MATRIX data collector (Fig. 22) coordinates the image and orientation sampling of the OTV with depth information from the winch to the laptop computer loaded with MSLog data acquisition software. The Windows based MSLog program provides an easy-to-use, on-screen graphical user interface for controlling the electronic components of the acquisition hardware.

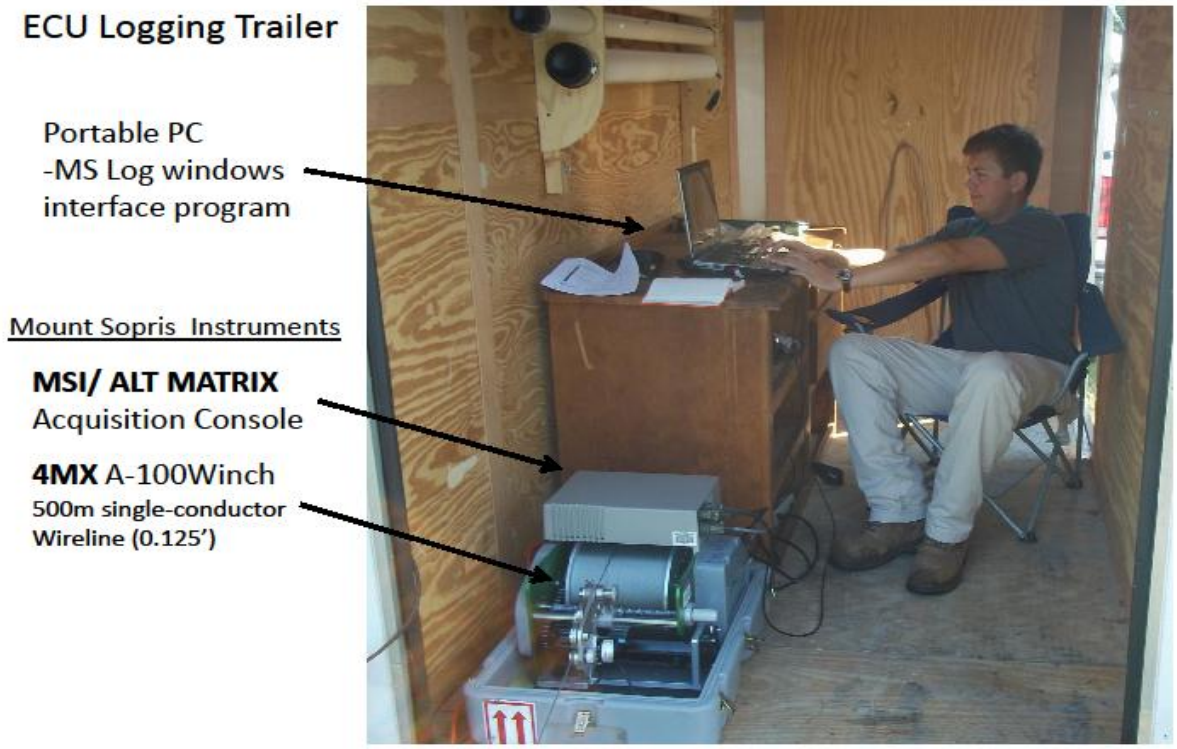

Figure 22. Interior of ECU geophysical logging trailer with tools and instruments employed during well logging. Alex Culpepper pictured operating winch using MATRIX software.

Wellcad® 4.3 (ALT) software was used to display, edit, and analyze well data from borehole logs in addition to exporting the OTV images in usable (.bmp) format. The images were mosaiced in Adobe Illustrator ® CS4. Erdas Imagine® 9.3 to perform all other image processing (rectification, calibration, enhancement, noise correction, classification, filtering, accuracy assessment, and conversion to a GIS format). ArcView® 9.3 was the preferred software to serve as the platform for visualization, management, and data acquisition during spatial analysis. Further data manipulation was performed in Microsoft Excel and plotted using Sigma Plot® 11.0.

Core sample preparation

A majority of the core acquired from the PW5 borehole had been slabbed by previous researchers, i.e. it was sawed in half giving a cross sectional view of the rock. The core was then labeled and the flat surface was polished to eliminate imperfections from sawing. Hand polishing with the grinding wheel and 220 grit silicon carbide successfully removed any fabric introduce by sawing and ensured the flat surface was completely planar. Painting the flat surface with an orange, water-soluble, block-printing ink using a rubber roller amplified the difference between macropores and matrix (Fig. 23). A copy stand was employed to photograph the core samples ensuring that the flat painted face of each core sample would remain aligned and orientated correctly with the digital camera (Fig. 24). To guarantee samples are photographed precisely horizontally and vertically, a small double axis bubble level was employed before photographing. Samples were photographed first as non- painted cores for sample identification then photographed a second time after the flat surface was painted. Photographs were downloaded directly from the camera to the PC using Nikon (software) for further manipulation.

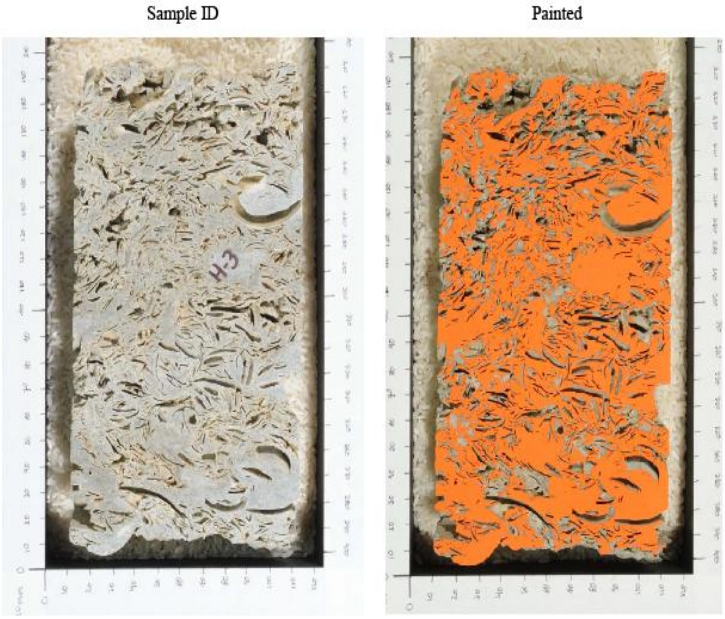

Figure 23. Unpainted and painted surfaces of slabbed core with orange printing ink that amplifies the difference between macropores and matrix.

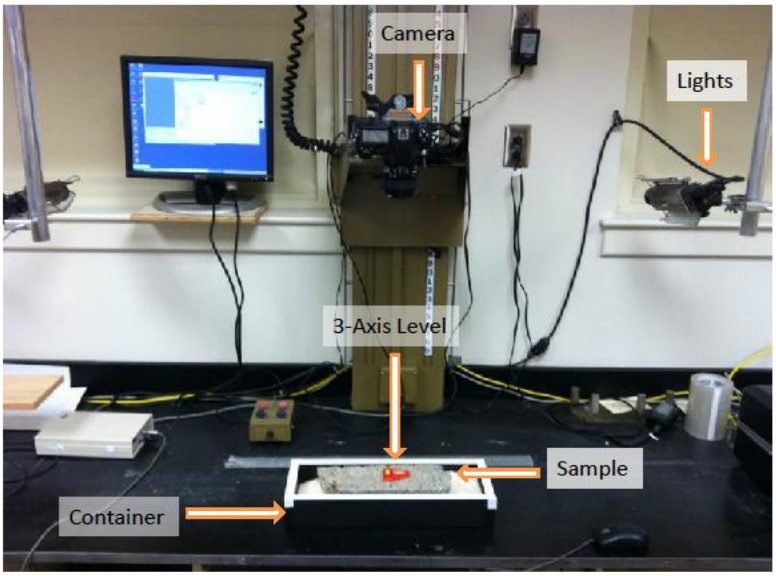

Figure 24. Copy stand employed to photograph core samples to ensure the flat surface would aligned and orientated correctly with digital camera.

Thin section preparation

Thin sections for both aquifers were made from samples impregnated with blue epoxy normally used to permit identification of carbonate minerals, which are difficult to distinguish due to their similar physical characteristics (Friedman, 1959). For the purpose of this study, the blue epoxy was used to enhance the difference between the macropores and matrix, just as the orange block printing ink did for the core samples. However, in this case the color represents pore spaces whereas in the painted core, the color represents the matrix. Next photographs of the multiple thin sections were made using a digital camera, enabling downloading into a computer for digital analysis.

Image Processing

Converting raw borehole, slabbed core, and thin section images into a format that could be examined and manipulated GIS was essential in obtaining accurate information for image analysis. Conversion of the raw, borehole, slabbed core, and thin section images to the binary classified image format suitable for GIS analysis required the following procedures: image mosaic, rectification/calibration, noise removal, image enhancement, binary classification, and filtering. A flow chart describing the general outline for image processing and conversion to appropriate GIS format is shown in Figure 25. Individual procedures highlighted in the Figure 25 flow chart are explained in more detail in the following section and are illustrated in Figure 29.

Image Mosaic

Two copies of the raw televiewer image were placed side by side to form a double image (Fig. 26) with the intention of eliminating any edge effect problem caused by examining a 360º

image of the borehole wall in planar view. When bisecting a 360 º image the pores at the edges were cut and lose their true areas, perimeters, and shape. With the goal of not only quantifying porosity, but also acquiring data characteristics related to pore geometry, image mosaics were necessary to account for all pores in the televiewer image. Slabbed core and thin section images did not require the image mosaic procedure because the entire sample was captured in the raw image.

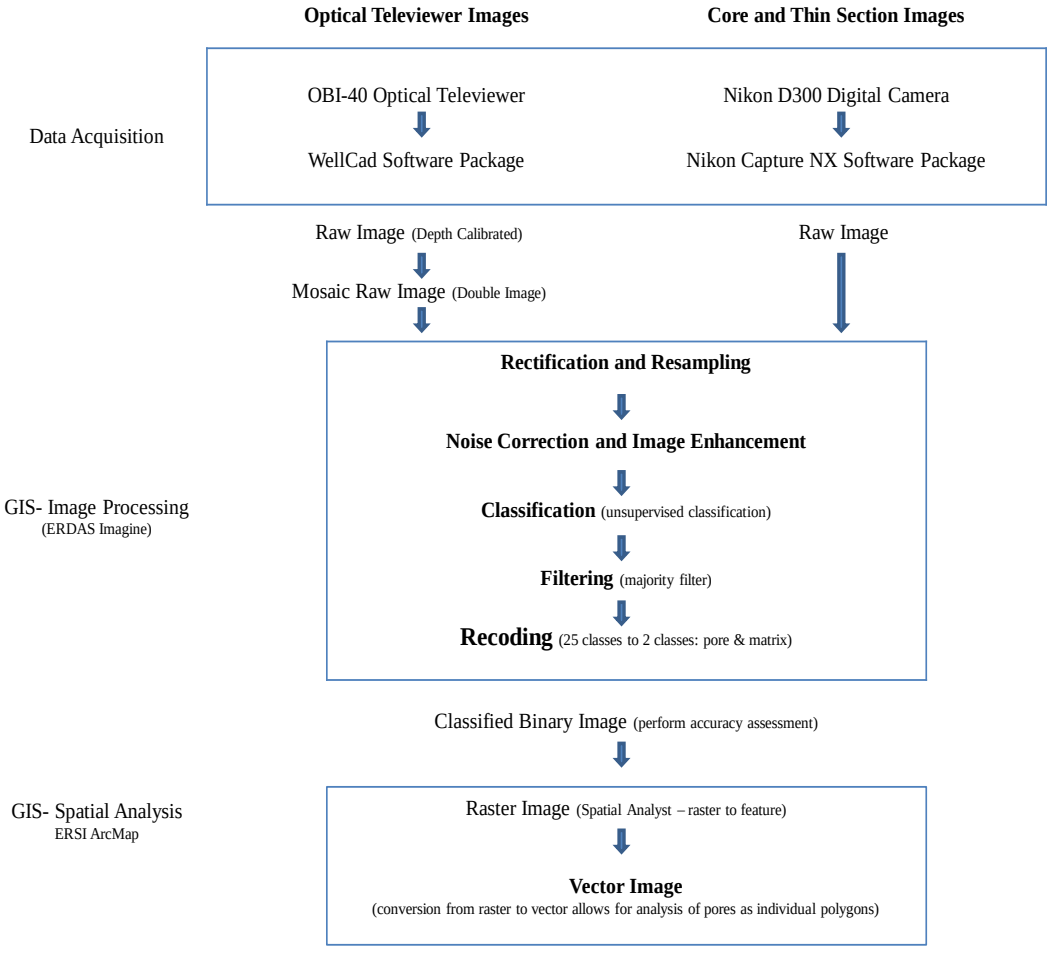

Figure 25 . Flow chart showing general image processing procedure and conversion of raw images to a GIS usable format.

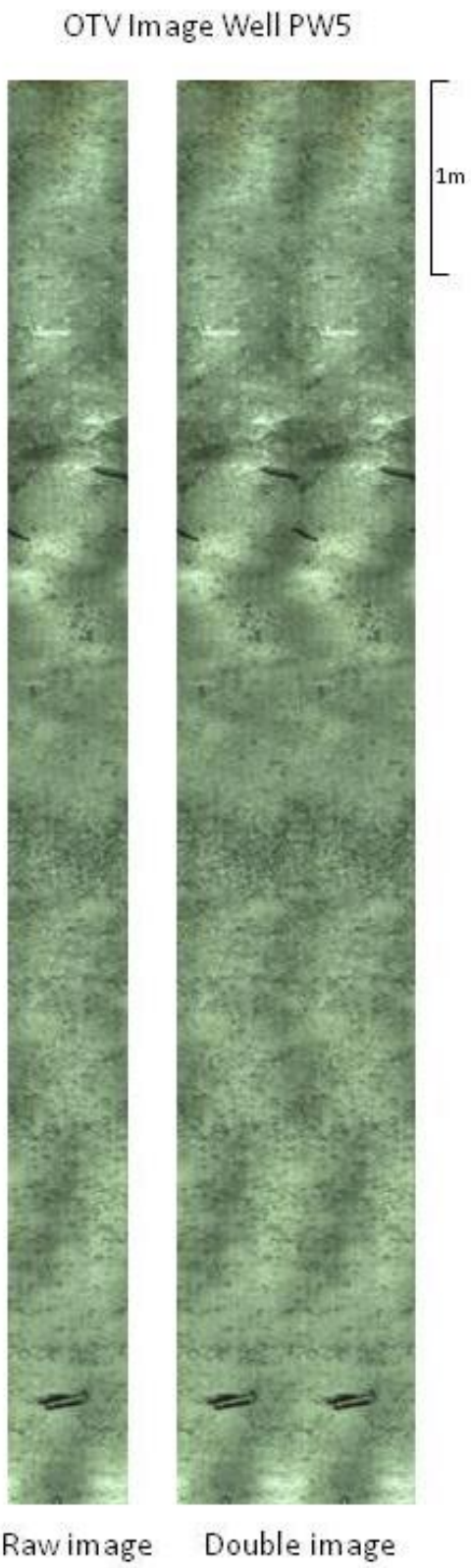

Figure 26. Flow chart of general image processing procedure and conversion of raw images to a GIS usable format.

Image geometric correction

Image geometric correction was a necessary processing procedure for removing the inherent geometric distortions from any input image and calibrating the data radiometrically. Geometric modification was accomplished through image rectification and restoration in which distortion was removed and the output image is made to have the desired projection properties, appropriate orientation, and uniform scale (ERDAS, 2010a). As a result individual picture elements (e.g. pixels) are converted form row/column to the proper planimetric format (e.g. latitude/longitude) (Gao, 2008; Mather & Magaly, 2011). However, in this case output format was converted to a (x,y) location not a (lat/long) location designated from a map projection, this allowed the geometrically corrected output image to be used in the accurate extraction of distance, polygon area, and directional information within the desired (x,y) coordinate system (Chandra & Ghosh, 2005). The vertical dimension of the optical televiewer image was determined from the minimum and maximum depths the tool reached (cm). Because the horizontal dimension of the raw image was collected in azimuthal direction (0°, 180°, 90°, 360°), the corrected length (cm) was derived from background caliper measurements (Fig. 27).The histogram for the diameter of well PW5 derived from caliper measurements taken at 0.005m intervals is shown in Figure 29. The histogram reveals that the mean diameters are close to the background caliper measurements, but should not be selected over the mode as the measurements used in calibrating the image because the data would be slightly skewed. The corrected horizontal dimension calculated from background diameter measurements was 51.33 cm/360° and the vertical dimension was 773 cm. The vertical and horizontal dimension values will be applied as control points on the four corners of the image, because degree of distortion in the imagery was low, a basic first-order polynomial transformation utilizing the nearest

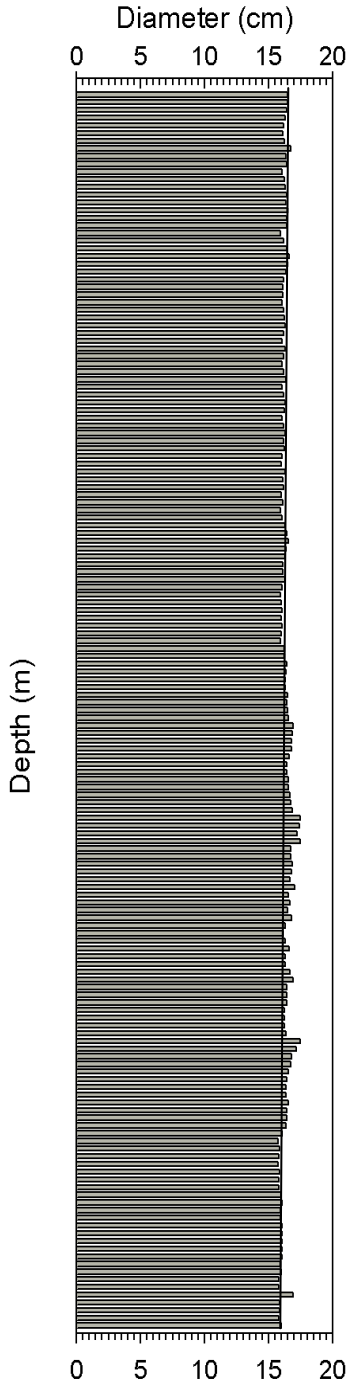

Figure 27. The diameter of well pw5 plotted as a bar graph. Vertical line represents mode of background diameter measurements to be used for calibration.

neighbor resampling algorithm was carried out. Computation of the root mean square (RMS) error was necessary to determine how well the transformation accounted for distortion. RMS error is a measure which represents the difference between the original control points and the new control point locations calculated by the transformation process (ERDAS, 2010b; Campbell, 1996). RMS error for each of the ground control point was kept at less than or equal to one during rectification, which is critical for rectification to be considered satisfactory (Campbell, 1996).

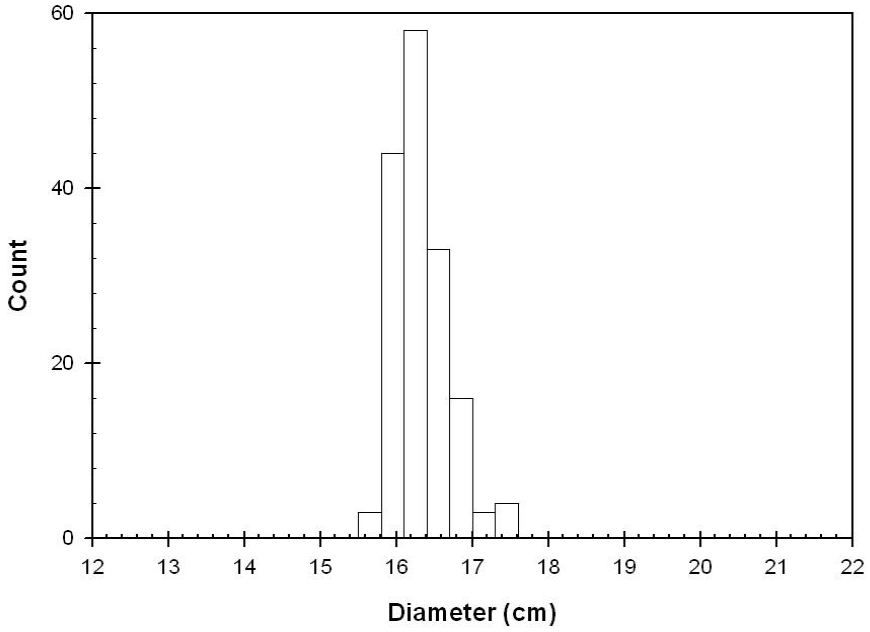

Figure 28. Borehole diameters calculated from caliper log for PW5. The diameter provided by caliper was used to calculate a circumference needed for image rectification.

Initial resolution for PW5 OTV image was 64.0 mega pixels (18239 x 3588 pixels), before resampling to a smaller output cell size of 0.01 cm. The resulting number of pixels from the resampled image was 793.0 mega pixels (77301 x 10264 pixels). A smaller cell size of

0.005cm was used to more accurately mimic features found on the original image during the classification process. Initial resolution for CHAS cores images averaged 7.0 mega pixels (2774 x 2571 pixels) before being resampled to a new smaller output cell size of 0.005cm. The resulting number of pixels from the resampled images averaged 9.3 mega pixels (3094 x 3014 pixels). Before resampling procedure CHAS and Biscayne thin section image resolution averaged 0.8 mega pixels (980 x 674 pixels) and 1.0 mega pixels (1158 x 761 pixels), respectively. After resampling to a smaller output cell size of 0.001 cm, the resulting number of pixels for the CHAS and Biscayne thin sections averaged 17.3 mega pixels (5150 x 3360 pixels) and 24.0 mega pixels (5946 x 3806 pixels), respectively.

The nearest-neighbor re-sampling algorithm determines a new pixel value by interpolating between the existing pixels to obtain an estimate of the new pixel value based off closest pixel value from the original uncorrected image (Verbyla, 2002). During the rectification process the nearest-neighbor re-sampling algorithm was implemented to upscale the amount of pixels from the original distorted image. Nearest-neighbor re-sampling was selected over bilinear or bicubic because it is the faster re-sampling method; also nearest-neighbor assignment does not change any of the values of cells from the original image. Nearest-neighbor assignment should be used for data where each value represents a class, member, or classification because smaller pixels will more accurately mimic features found on the original image during the classification process. (ERDAS, 2010a; Lillesand et al. 2004).

Image rectification is required for developing GIS data bases for GIS modeling, creating accurate scaled photomaps, extract accurate distance and area measurements, changing pixel grid to fit a map projection system, and performing any other analyses requiring precise geographic locations (ERDAS, 2010b). A total of (four) control points was sufficient for the first order

polynomial used with all images. The minimum number of control points to be used in the transformation was determined by

$$\frac{t+1\ (t+2)}{2},$$

Where, t is the order of the polynomial (ERDAS, 2010a).

Noise correction and image enhancement

At irregular intervals line-oriented noise problems occurred in the form of vertical lines running across optical televiewer images. Removing lines of flawed pixels required execution of a replace bad lines function in Erdas Imagine (ERDASa , 2010). The flawed pixel was replaced with the average of the values of the pixels from both sides of the flawed pixel. Any orientated noise problems leading to flawed pixels would have lead to inaccurate classification and had be corrected before the classification procedure could begin. No flawed pixels were detected in CHAS core images or either set of thin section images.

Before classification, the image was enhanced through contrast manipulation in order to aid in classification and promote individual features during visual interpretation post classification. A 2.5 standard deviation general contrast stretch was carried out on the optical televiewer image in an attempt to balance pixel brightness and reduce effects of eccentricity during logging. A 0.5 standard deviation general contrast stretch was applied to CHAS core and both sets of thin sections. This method increased the distinction of features by promoting the contrast of the resulting image.

Classification

The rectified and enhanced image was subjected to an unsupervised classification where classes and assignment of specific pixels was performed by the computer. Using the parametric classifier Iterative Self-Organizing Data Analysis Technique Algorithm (ISODATA), unsupervised classification sorted pixels according to statistical association, then interpreted the pixels into classes or categories (ERDAS, 2010a, b), based on spectral distance between candidate pixel and spectral mean of each existing signature (Jensen 2000).

Comparison of unsupervised and supervised classification indicates that an unsupervised classification method has advantages when classifying heterogeneous classes in high-resolution digital images (Rogan and Yool, 2001). Thirty separate classes were chosen for classification because there would be more separation of classes that were distinctly similar also sampling could be done more efficiently (Rogan and Yool, 2001). Separating into 30 classes increased confidence that pore and matrix would be classified correctly (Zhou and Robinson, 2001). Results showed too low of a class output will likely result in poor separation between pore and matrix because the image has been oversimplified. To high of a class output would not noticeably change the division between pixels but would result in more time spent recoding with no net gain in separation between pore and matrix classification.

Recoding and filtering

After the thirty initial classes had been appointed, they were recoded to two classes: matrix and pore. In order to achieve this, the classified image was laid over the original image with all designated classes "turned off" by setting their opacity to zero to allow visual inspection

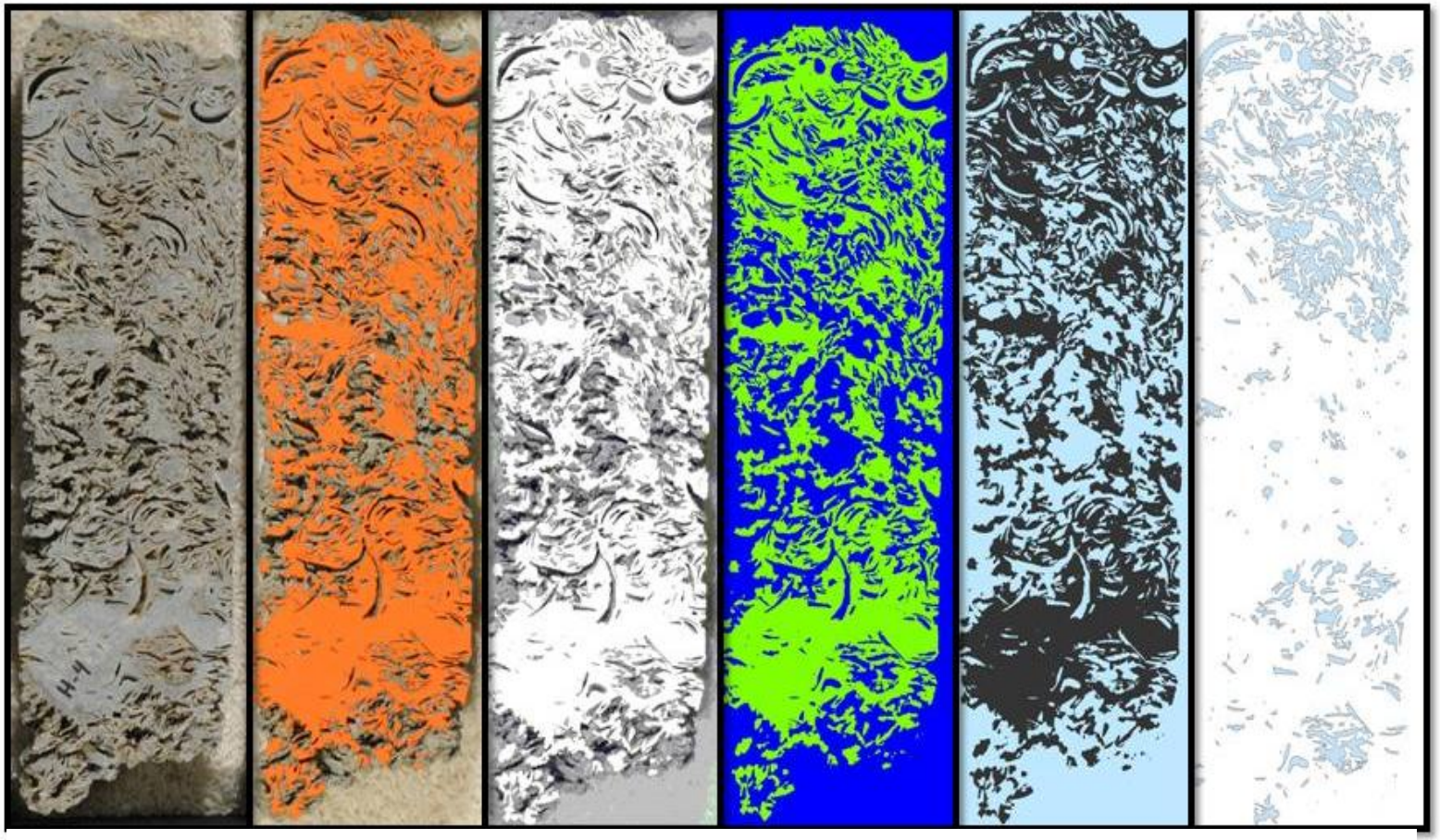

Figure 29. Description left to right; raw unpainted slabbed core; painted slabbed core; after image enhancement has been performed; after classification (30 individual classes); after recoding procedure (2 classes pore/matrix); after successful vector conversion.

of each class. Starting with a single class and then "turning it on" by setting the opacity to one allowed for visual inspection of that single class with the original image as its background. If a majority of features in that single class coincide with what has been designated matrix in the original image, it was designated 'matrix'. Alternatively, if that single class features coincide with what has been designated pore space in the original image it was designated as 'macropore'. This process was repeated for all 30 classes until each has been recoded to either matrix or macropore class. Optical televiewer, slabbed cores, and thin section images were all be subjected to the same "macropore or matrix" recoding based off comparison of single classes to original raw image for reference to guarantee the most accurate recoding (Fig. 29).

The recoded binary image was then filtered by applying a 3x3 majority statistical filter. The filter operation smoothes out the features in the binary image to more closely imitate pores from the original image.

Accuracy Assessment

Accuracy measures the agreement between a standard assumed to be correct and a classified image with known quality (Campbell, 1996) and assists in defining the "correctness" of an image classification. A 50 point random sampling accuracy assessment was carried out on all binary borehole, core and thin section images in ERDAS Imagine. Random points were placed on the original image; the user visual inspected then inputted values corresponding to those of the two classes (pore or matrix). The software then compares the user inputted values from the original image to those determined from the recoded image and gives a measure of agreement between the two images as an overall classification percent and a kappa coefficient

(Jenson, 1996; Campbell, 1996). Kappa (κ) is defined by a measure of the difference between observed agreement between two images .Chrisman (1980) and others simplified the equation as,

$$\kappa = \frac{Observed - expected}{1 - expected}$$

where "Observed" designate the accuracy reported in the error matrix and "expected" designates the correct classification to be projected by change agreement between the two images. The overall classification accuracy and kappa coefficients for the CHAS borehole image were 90% and 0.78 respectively; CHAS core had an overall accuracy of 96% and a kappa coefficient of .85. Thin sections images from CHAS and Biscayne had an overall accuracy's of 98% and 97% respectively with kappa coefficients of 0.91 and 0.92 respectively. Conventionally, a kappa of 0.61- 0.80 is strong agreement and more then 0.8 is complete agreement, the kappa coefficients are greater than 0.80 and thus signify complete agreement (Fleiss, 1981). Previously classified images of Biscayne core had an overall classification accuracy and kappa coefficient of 90% and 0.77; while Biscayne borehole images had an accuracy of 88% and a kappa coefficient of 0.76.

Vector conversion

In ArcGIS, the binary image was converted to a vector format (Fig. 29); the pore attribute was converted to a particular value (e.g., 1) and the matrix attribute was also converted to a particular value (e.g., 2) allowing for individual attributes to be analyzed separately. In the attribute table for each image new fields were added for area and perimeter calculations. Using ArcGIS field calculator, VBA (Visual Basic for Applications) statements were uploaded to extract area and perimeter measurements for each individual polygon for a selected attribute

(e.g., 1-pore or 2-matrix). The full attribute table was the export to Excel and SigmaPlot for analysis and data manipulation.

Sample Name	Overall Classification Accuracy (%)	Kappa Coefficient
h-1	96.00	0.914
h-2	100.00	1.000
h-3	92.00	0.822
h-4	98.00	0.923
h-5	94.00	0.842
h-6	90.00	0.800
h-7	94.00	0.866
h-8	100.00	1.000
hr-1	96.00	0.911
hr-2	96.00	0.905
hr-3	94.00	0.868
hr-4	92.00	0.827
hr-5	96.00	0.811
hr-6	98.04	0.847
hr-7	98.00	0.926
hr-8	98.00	0.912

Table 4. Overall classification and kappa coefficients from Castle Hayne slabbed (half) core images. Average classification is 95.75% and kappa coefficient is 0.87 signifying agreement between classified and original image.

Porosity

2D porosity is here defined as the percentage of surface area occupied by macropores within a rectangular window. After generating a rectangle with the dimensions of interest ArcMap field calculator was used to calculate the total area of all macropores within the window. Once the area of macropores within the rectangle was determined, simply dividing by the area of the rectangle gave a percent area covered by macropores (i.e. the porosity). This porosity calculation procedure was repeated for each image within the three scales of observation.

The area of the polygon area was calculated, then divided by the total pore area within that particular polygon giving the percent area covered by macropores (e.g. percent porosity).

Shape Measure

The ability to measure shape and orientation of pores from digital images would allow for the investigation into geometry of pores found in the CHAS. The quantification of shape measures, although difficult, would provide useful insight into how a pore's geometry influences porosity in moldic sedimentary rocks. A shape index that describes the complex nature of pore shapes in carbonate rocks was presented by Anselmetti et al., (1998) based on measurements of pore area and perimeter. The shape index that will be applied to analyze data is expressed as:

$$\gamma = \frac{P}{2\sqrt{\pi A}}$$

Where γ is the shape index, *P* is the perimeter and *A* is the area of the pore (Anselmetti et al., 1998). ArcMap provides the necessary function tools needed to obtain measurements of pore area and perimeter. The shape index has a range from one to infinity; a shape index value of one would represents a circle with the eccentricity of zero, or perfect circle and the higher positive values from one indicate an increase in complexity of the shape (Fig. 31). Pore shape was plotted against pore area to study how pore shape varies with size in the karst limestones.

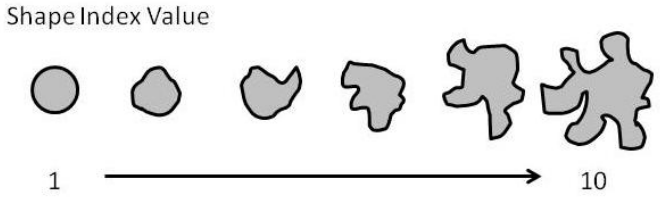

Figure 31. Left to right starting with simple pore with low shape index increasing to a complex pore with high shape index

APPENDIX D: PORE GEOMETRY BOX PLOT STATISTICS

	CHAS OTV	Biscayne OTV	CHAS Core	Biscayne Core	CHAS Thin Section	Biscayne Thin Section
Mean	20.03	32.38	0.04	0.01	2.22E-03	2.43E-03
Median	6.65	9.14	0.01	0.01	1.19E-04	1.19E-04
Std. Dev	53.03	90.48	0.19	0.09	2.05E-02	1.55E-02
Std. Err	3.85	3.41	0.00	0.00	3.63E-04	2.60E-04
Min	4.01	4.00	0.00	0.00	1.40E-05	4.00E-06
Max	608.60	1469.00	7.01	5.84	8.05E-01	3.97E-01

Table 5. Statistics of pore area (cm^2) distribution for pore areas derived from optical televiewer, core and thin-sections.

	CHAS OTV	Biscayne OTV	CHAS Core	Biscayne Core	CHAS Thin Section	Biscayne Thin Section
Mean	99.98	55.88	0.84	0.44	0.14	0.16
Median	38.60	24.41	0.37	0.24	0.05	0.07
Std. Dev	232.80	137.19	2.34	0.97	0.51	0.48
Min	18.20	8.21	0.02	0.10	0.02	0.01
Max	2554.18	2789.36	82.01	49.56	13.38	17.64

Table 6. Statistics of pore perimeter (cm) distribution for pore areas derived from optical televiewer, core and thin-sections.

	CHAS OTV	Biscayne OTV	CHAS Core	Biscayne Core	CHAS Thin Section	Biscayne Thin Section
Mean	5.39	2.70	1.49	1.46	1.31	1.31
Median	4.39	2.33	1.43	1.30	1.20	1.21
Std. Dev	3.49	1.51	0.44	0.50	0.31	0.34
Std. Err	0.25	0.06	0.00	0.00	0.00	0.01
Min	2.39	1.04	1.02	0.89	0.93	1.09
Max	29.21	20.53	8.74	11.98	6.20	8.75

Table 7. Statistics of pore shape index distribution for pore areas derived from optical televiewer, core and thin-sections.

APPENDIX E: OTV IMAGES UTILIZED IN STUDY

OTV Image Well PW5

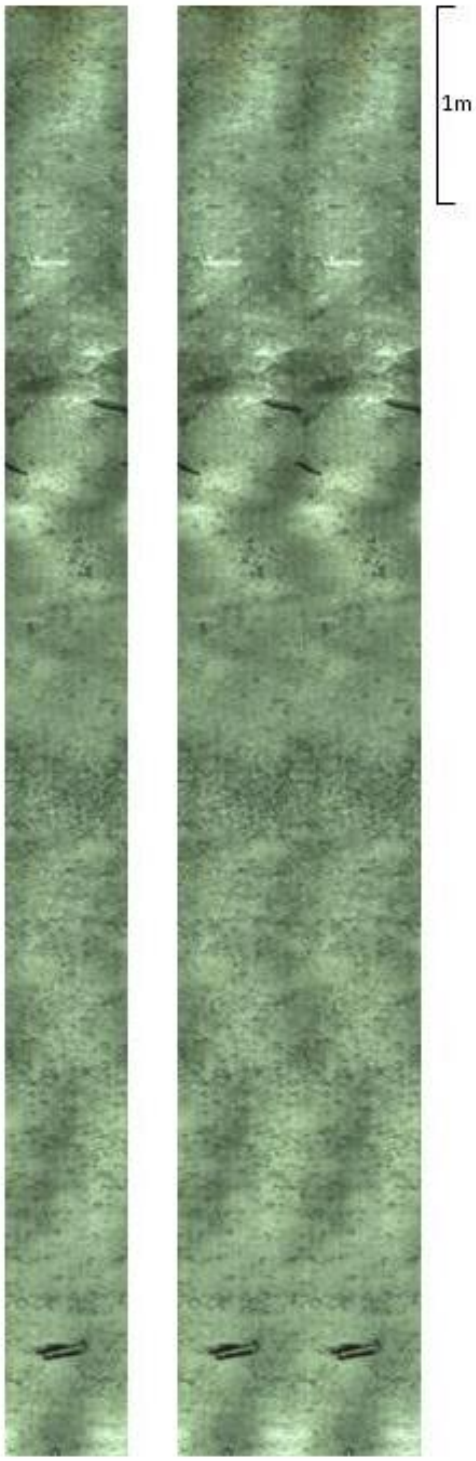

Raw image Double image

OTV Image Well FPL1

Raw image Double image

APPENDIX F: PHOTOGRAPHS OF BISCAYNE CORE UTILIZED IN STUDY

1-6

1-10

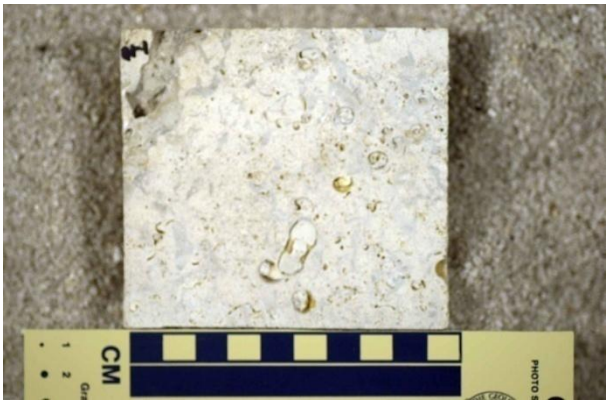

1-12

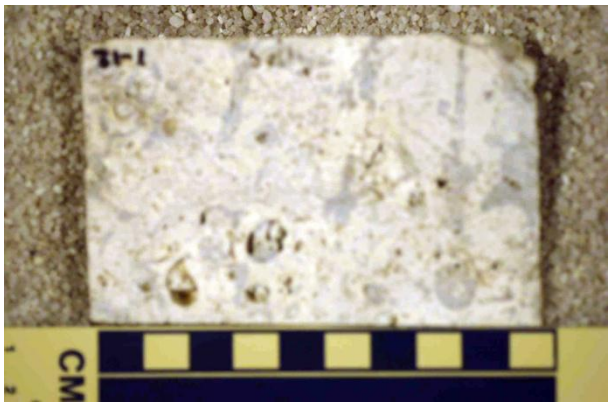

1-15

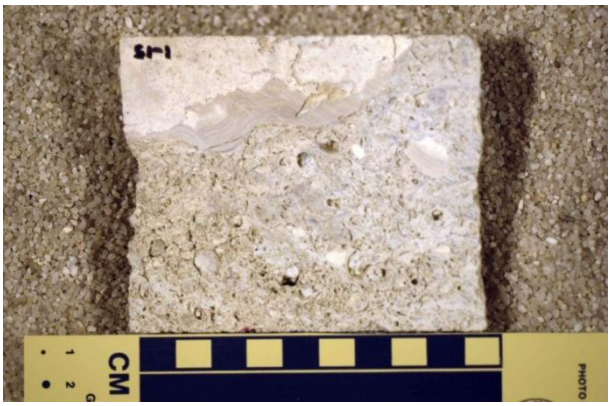

1-19

2-3

2-4

2-6

2-11

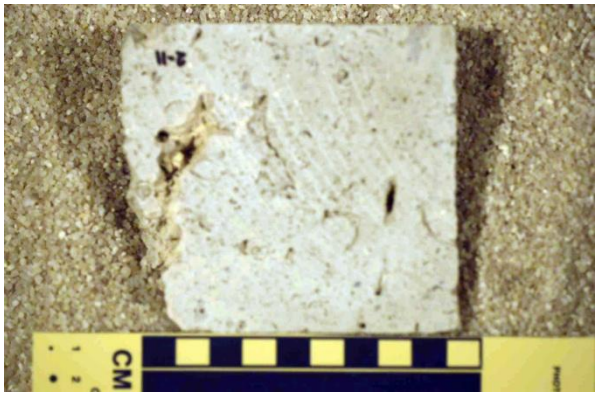

3-1

3-2

3-3

3-12

3-15

4-4

4-7

4-15

5-5

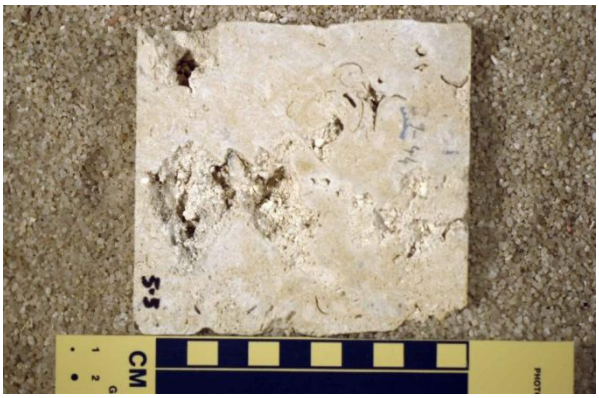

5-10

5-12

6-3

6-6

6-10

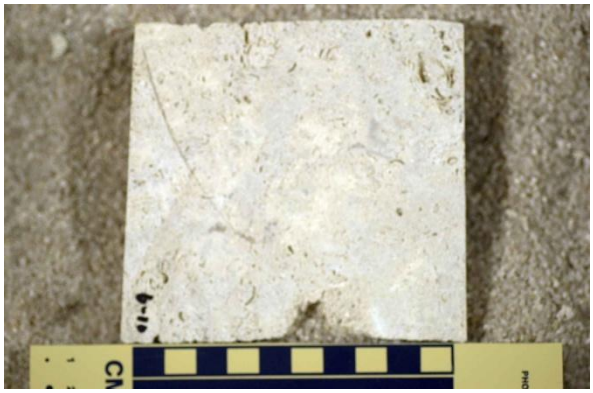

6-13

APPENDIX G: PHOTOGRAPHS OF CHAS CORE UTILIZED IN STUDY

H-1

H-2

H-3

H-4

H-5

H-6

H-7

H-8

HR-1

HR-2

HR-3

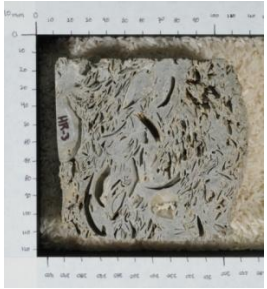

HR-4

HR-5

HR-6

HR-7

HR-8

Q1_A

Q1_B

Q2_A

Q2_B

Q3_A

Q3_B

Q4_A

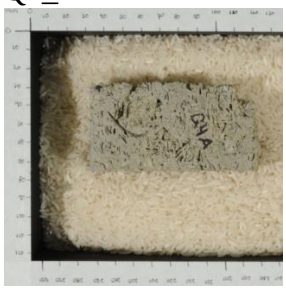

Q4_B

Q5_A

Q5_B

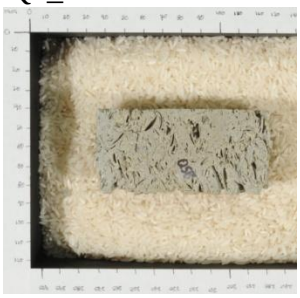

Q6_A

Q6_B

Q7_A

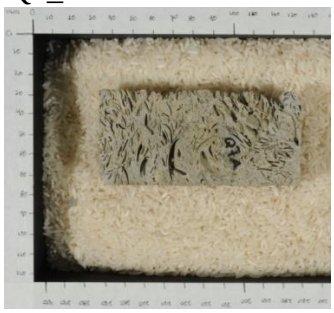

Q7_B

Q8_A

Q8_B

Q9_A

Q9_B

Q10_A

Q10_B

Q11_A

Q11_B

Q12_A

Q12_B

Q13_A

Q13_B

Q14_A

Q14_B

Q15_A

Q15_B

Q16_A

Q16_B

Q17_A

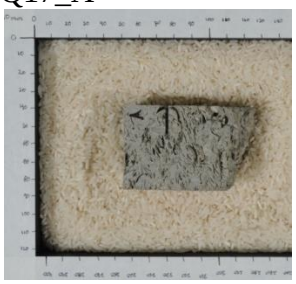

Q17_B

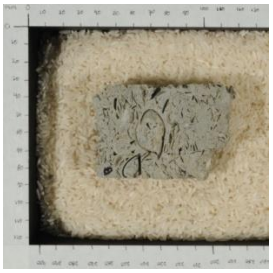

Q18_A

Q18_B

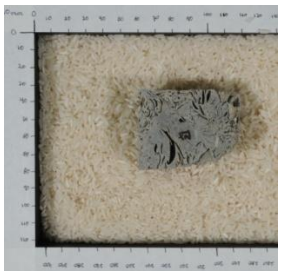

Q19_A

Q19_B

Q20_A

Q20_B

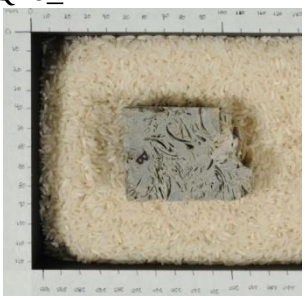

Q21_A

Q21_B

Q22_A

Q22_B

Q23_A

Q23_B

Q24_A

Q24_B

Q25_A

Q25_B

Q26_A

Q26_B

Q27_A

Q27_B

Q28_A

Q28_B

Q29_A

Q29_B

APPENDIX H: PHOTOGRAPHS OF BISCAYNE THIN SECTIONS USED IN STUDY

1-6

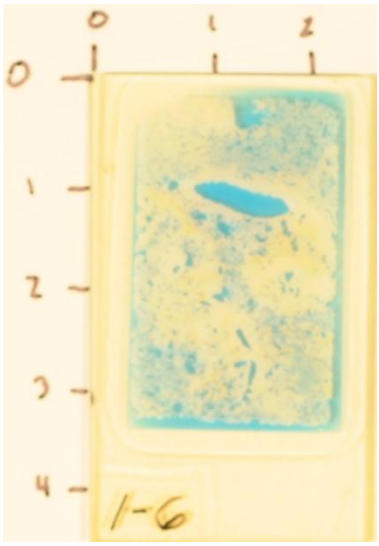

1-10

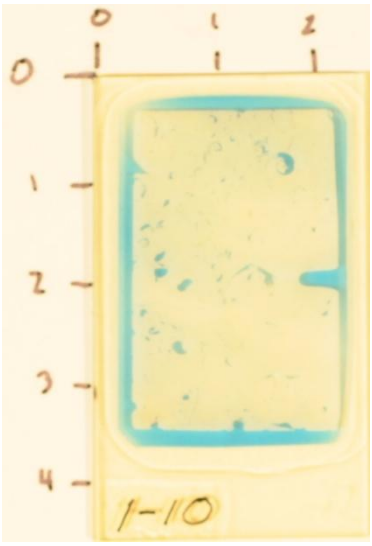

1-19

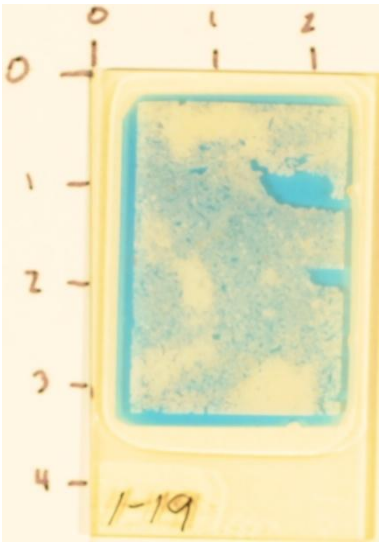

2-3

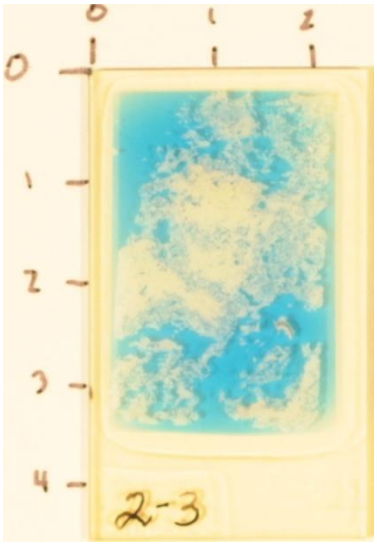

2-4

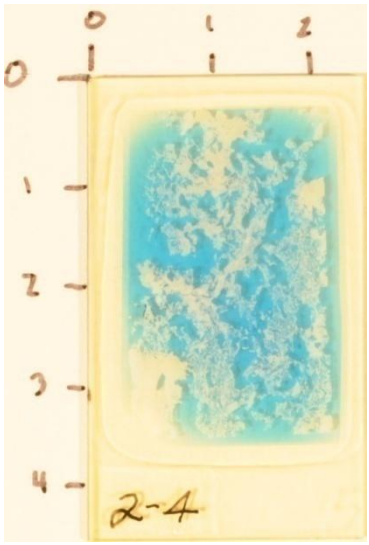

3-3

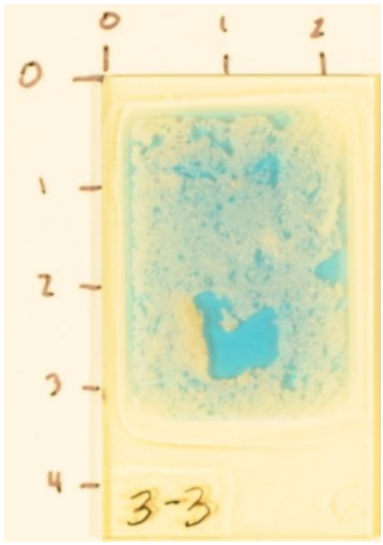

4-4

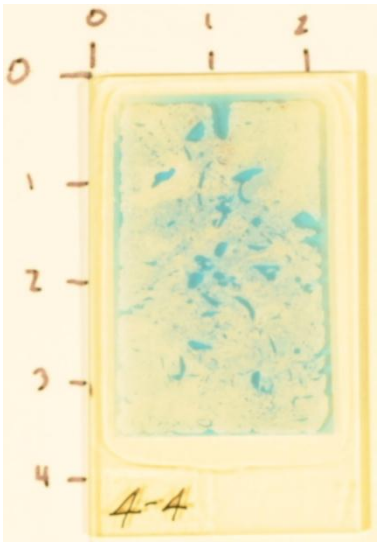

4-15

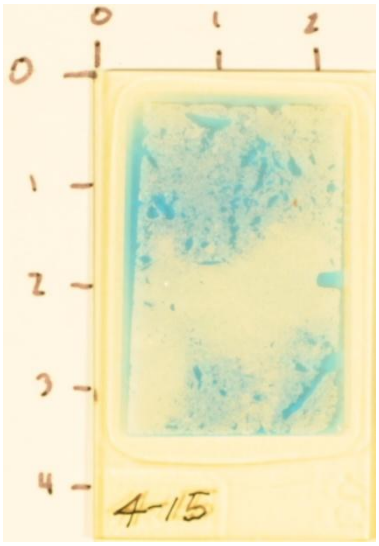

5-5

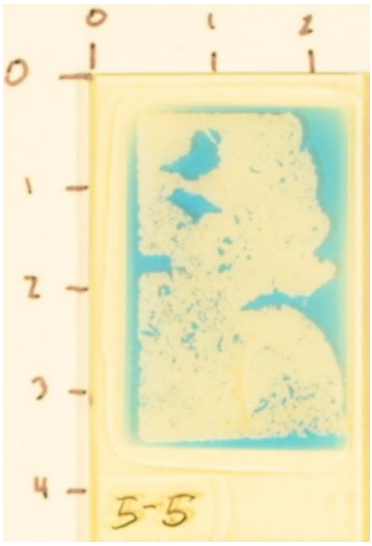

5-14

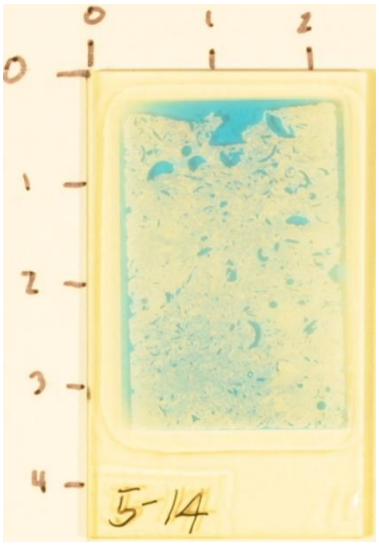

6-13

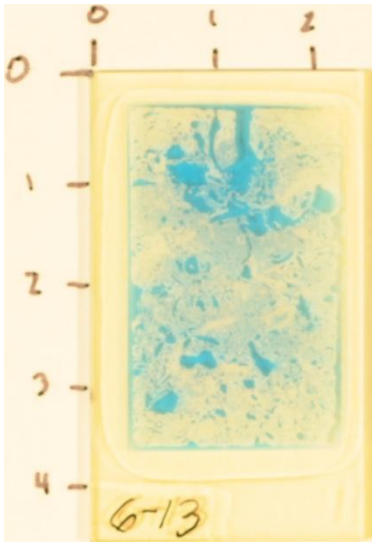

1-1

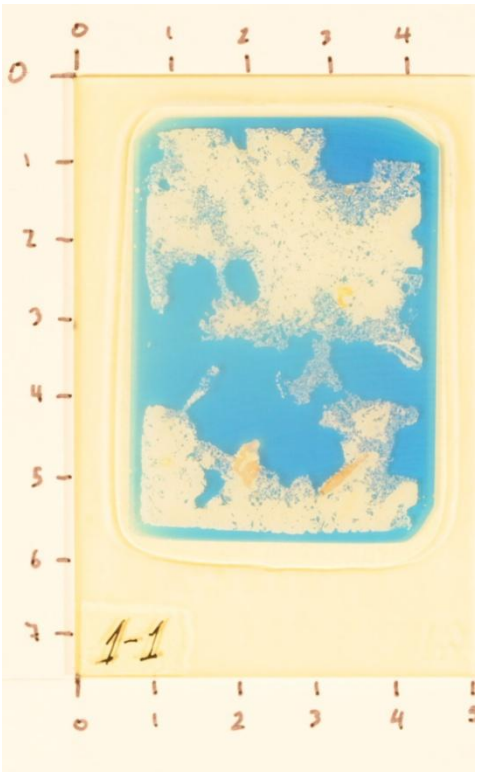

2-11

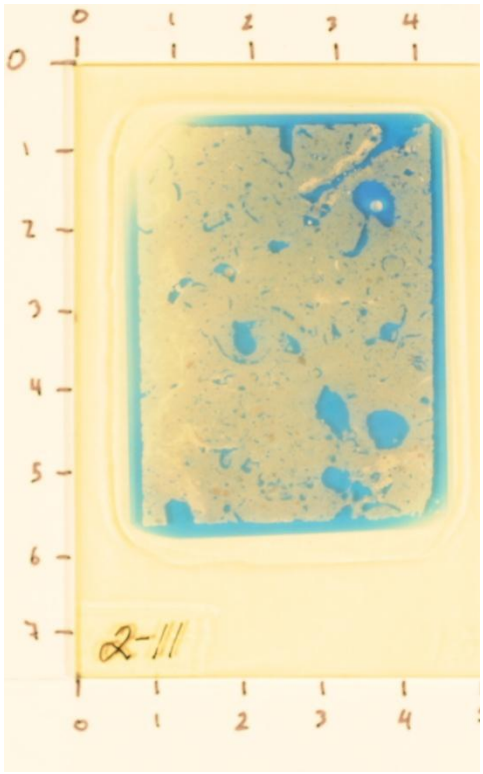

5-8

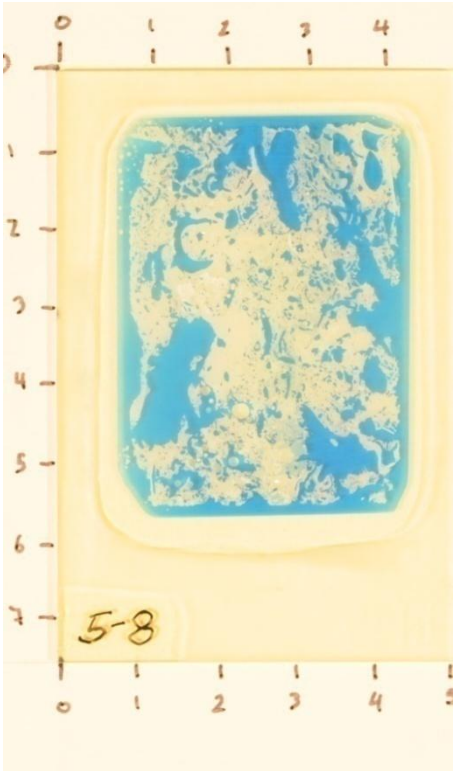

APPENDIX I: PHOTOGRAPHS OF CHAS THIN SECTIONS UTILIZED IN STUDY

37-5

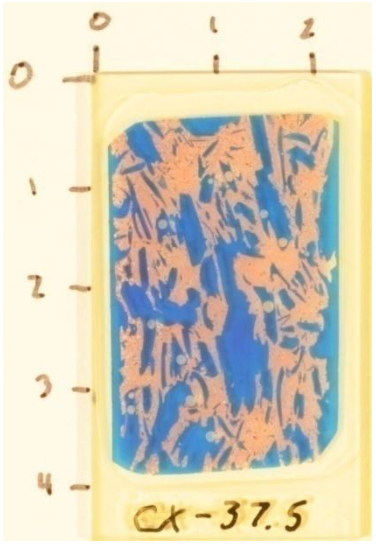

38-5

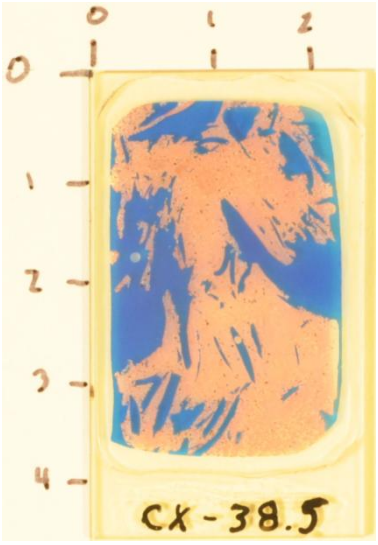

39-0

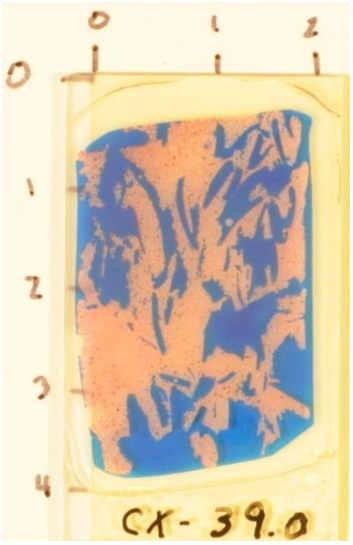

39-5

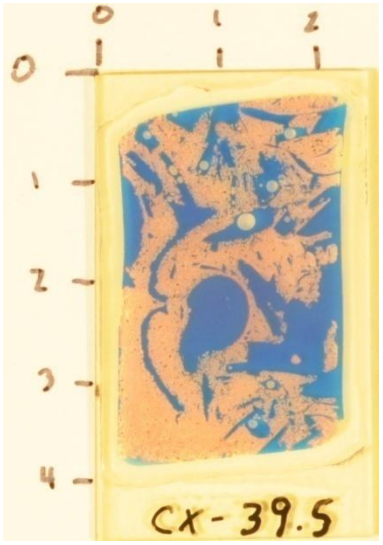

40-5

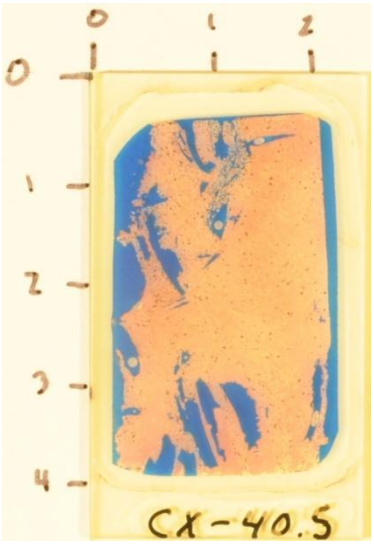

62-0

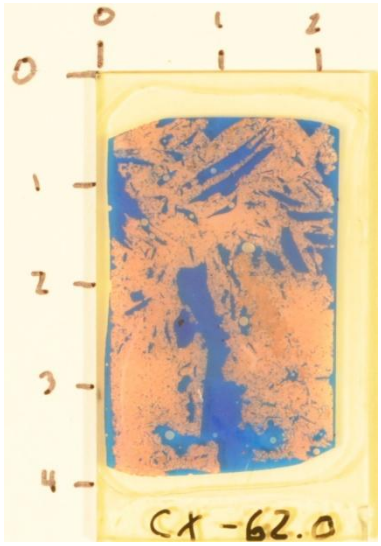

62-5

63-0

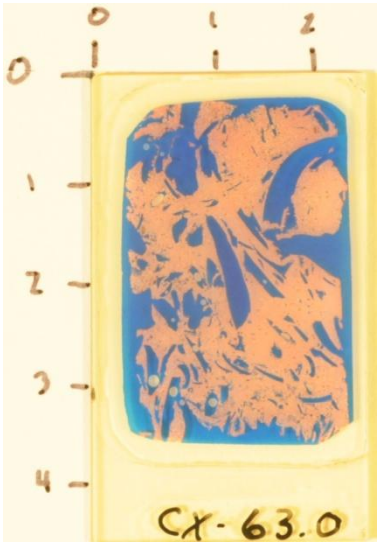

63-5

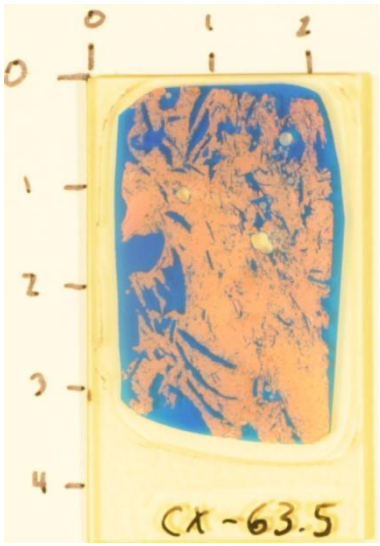

64-0

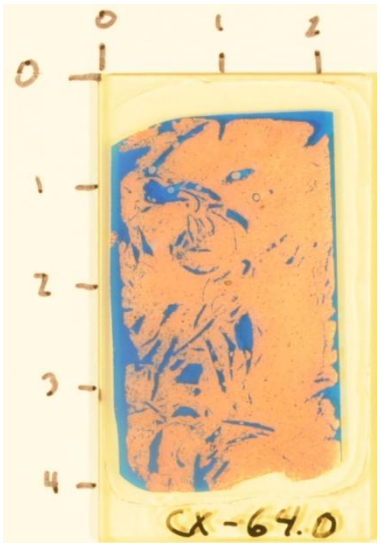

64-5

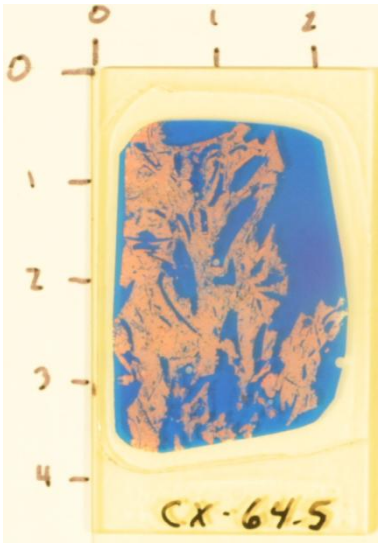

APPENDIX J: ACCURACY ASSEMENT REPORTS

Accuracy assement for the CHAS Core

Sample Name	Overall Classification Accuracy (%)	Kappa Coefficient
h-1	96.00	0.91
h-2	100.00	1.00
h-3	92.00	0.82
h-4	98.00	0.92
h-5	94.00	0.84
h-6	90.00	0.80
h-7	94.00	0.87
h-8	100.00	1.00
hr-1	96.00	0.91
hr-2	96.00	0.90
hr-3	94.00	0.87
hr-4	92.00	0.83
hr-5	96.00	0.81
hr-6	98.04	0.85
hr-7	98.00	0.93
hr-8	98.00	0.91
q1a	92.00	0.73
q1b	92.00	0.82
q2a	94.12	0.74
q2b	96.08	0.78
q3a	92.00	0.83
q3b	96.00	0.91
q4a	96.00	0.86
q4b	92.16	0.67
q5a	96.00	0.81
q5b	94.00	0.77
q6a	96.00	0.65
q6b	94.12	0.71
q7a	94.00	0.87
q7b	100.00	1.00
q8a	96.08	0.77
q8b	94.00	0.87
q9a	96.00	0.83
q9b	98.00	0.91
q10a	98.00	0.92
q10b	100.00	1.00
q11a	96.08	0.78
q11b	98.00	0.91
q12a	94.14	0.76
q12b	98.00	0.88

q13a	96.00	0.78
q13b	94.22	0.74
q14a	96.00	0.82
q14b	94.00	0.79
q15a	98.00	0.93
q15b	98.67	0.93
q16a	98.00	0.92
q16b	98.00	0.91
q17a	94.00	0.80
q17b	96.00	0.85
q18a	98.08	0.85
q18b	98.00	0.66
q19a	96.10	0.81
q19b	94.00	0.76
q20a	100.00	1.00
q20b	94.00	0.79
q21a	96.00	0.81
q21b	96.00	0.89
q22a	96.00	0.87
q22b	94.00	0.81
q23a	96.00	0.88
q23b	94.00	0.81
q24a	98.00	0.91
q24b	98.00	0.91
q25a	96.08	0.83
q25b	96.00	0.80
q26a	100.00	1.00
q26b	94.00	0.79
q27a	92.00	0.82
q27b	94.00	0.85
q28a	100.00	1.00
q28b	94.00	0.76
q29a	98.00	0.94
q29b	94.00	0.81
Average	**95.86**	**0.85**

Biscayne Core

Sample Name	Overall Classification Accuracy (%)	Coefficient
1_6	94.23	0.86
1_10	92.69	0.81
1_12	90.00	0.76
1_15	91.15	0.82
1_19	82.69	0.64
2_3	88.46	0.77
2_4	95.38	0.91
2_6	90.00	0.68
2_11	85.38	0.70
3_1	92.31	0.85
3_2	93.46	0.87
3_3	94.23	0.87
3_12	86.15	0.71
3_15	89.62	0.78
4_4	93.08	0.68
4_7	86.15	0.85
4_15	92.69	0.85
5_5	96.15	0.92
5_10	93.46	0.87
5_12	90.00	0.80
6_3	85.00	0.69
6_6	88.08	0.71
6_7	83.46	0.59
6_10	82.69	0.65
6_13	85.38	0.71
Average	**89.68**	**0.77**

CHAS Thin-section

Sample Name	Overall Classification Accuracy (%)	Kappa Coefficient
37-5	98.00	0.96
38-5	98.00	0.95
39-0	96.00	0.85
39-5	100.00	1.00
40-0	98.00	0.91
40-5	98.00	0.92
62-0	98.00	0.93
62-5	100.00	1.00
63-0	96.00	0.85
63-5	96.00	0.84
64-0	98.00	0.92
64-5	98.00	0.92
Average	**97.83**	**0.92**

BISCAYNE Thin-section

Sample Name	Overall Classification Accuracy (%)	Kappa Coefficient
1-1b_f	96.00	0.87
1-6b_f	98.00	0.93
1-10b_f	98.00	0.93
1-19b_f	100.00	1.00
2-3b_f	98.00	0.94
2-4b_f	96.00	0.85
2-11b_f	98.00	0.93
3-3b_f	100.00	1.00
4-4b_f	98.00	0.85
4-15b_f	100.00	1.00
5-5b_f	98.00	0.83
5-8b_f	98.00	0.92
5-15b_f	96.00	0.85
6-13b_f	98.00	0.93
Average	**98.00**	**0.92**

APPENDIX K: PLOTS OF PORE AREA AND PERIMETER DISTRIBUTION

Plots of pore area and perimeter distribution from CHAS core samples

H-1

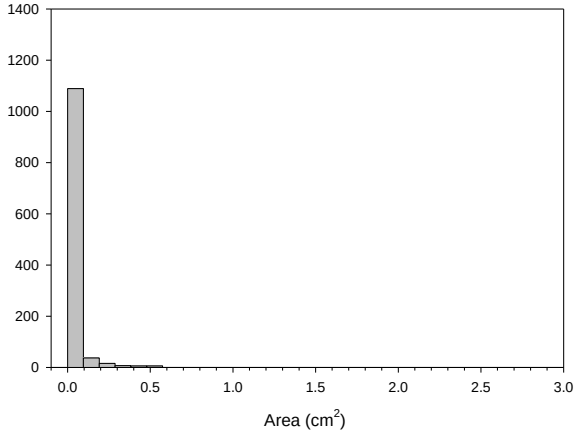

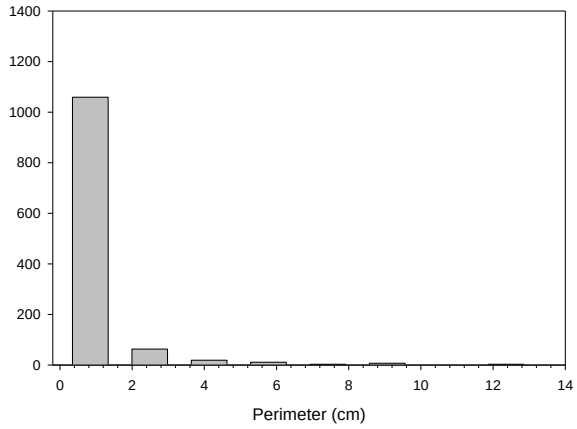

H-2

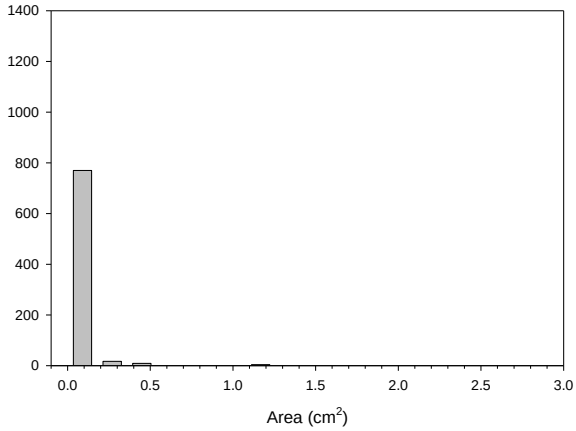

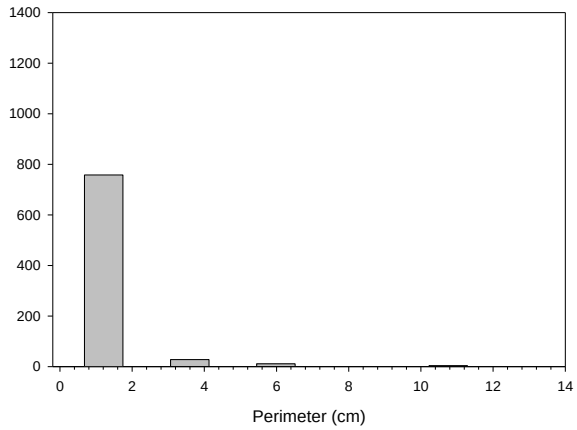

H-3

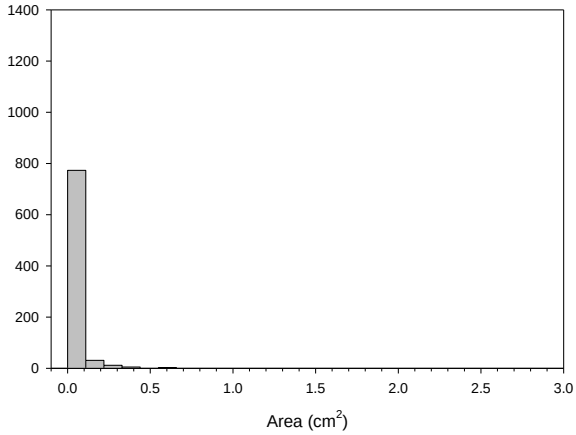

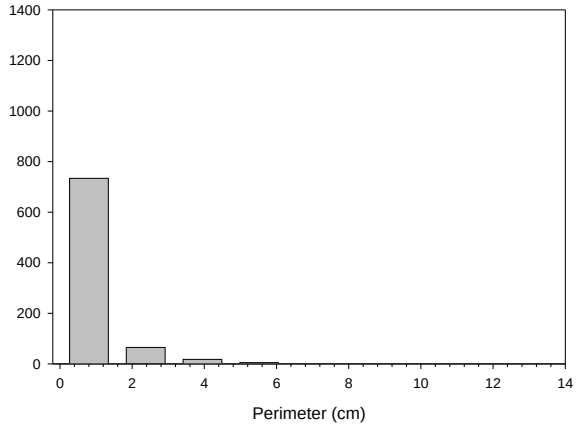

H-4

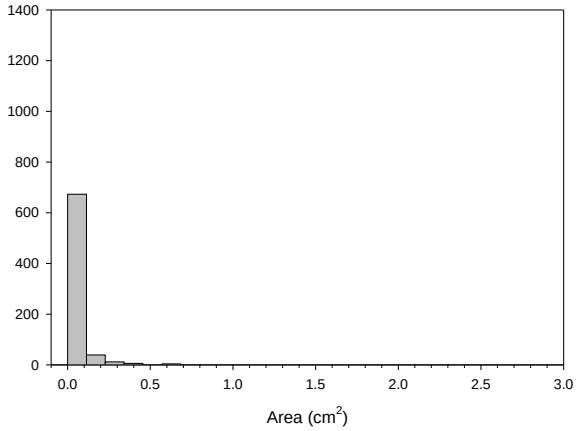
1400
1200
1000
800
600
400
200
0
0.0
0.5
1.0
1.5
2.0
2.5
3.0
Area (cm2)

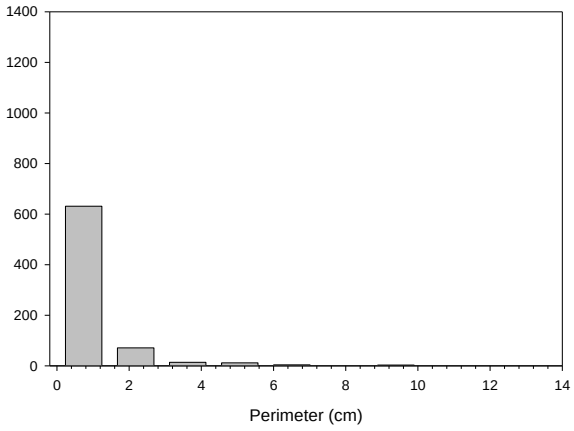
1400
1200
1000
800
600
400
200
0
0
2
4
6
8
10
12
14
Perimeter (cm)

H-5

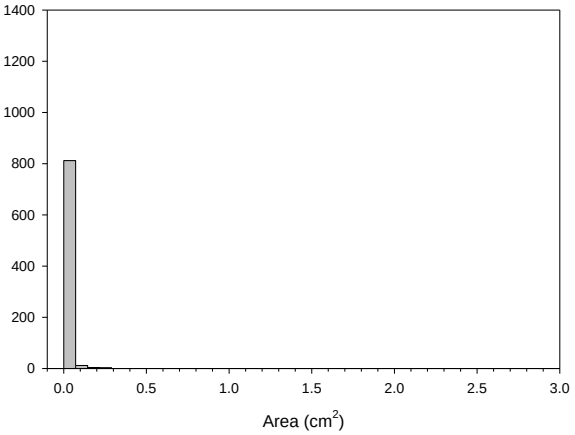
1400
1200
1000
800
600
400
200
0
0.0
0.5
1.0
1.5
2.0
2.5
3.0
Area (cm2)

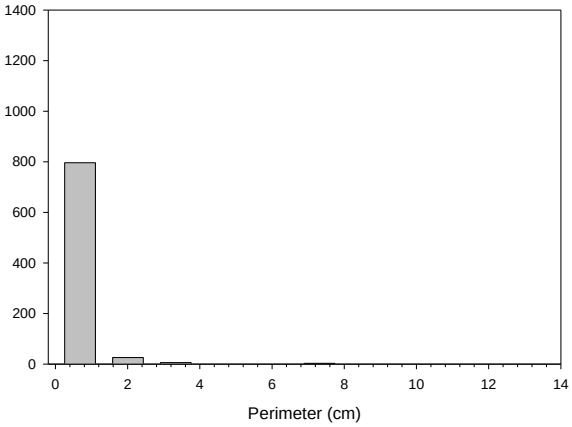
1400
1200
1000
800
600
400
200
0
0
2
4
6
8
10
12
14
Perimeter (cm)

H-6

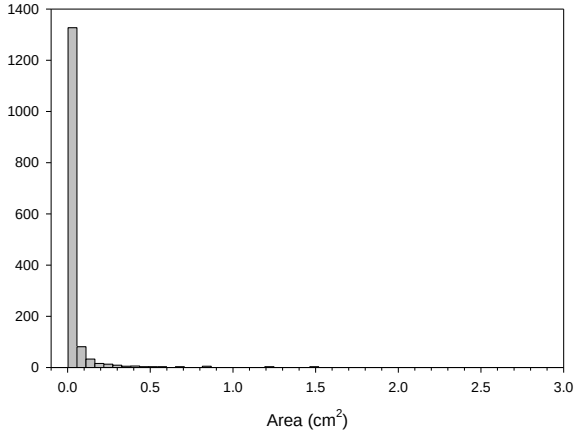
1400
1200
1000
800
600
400
200
0
0.0
0.5
1.0
1.5
2.0
2.5
3.0
Area (cm2)

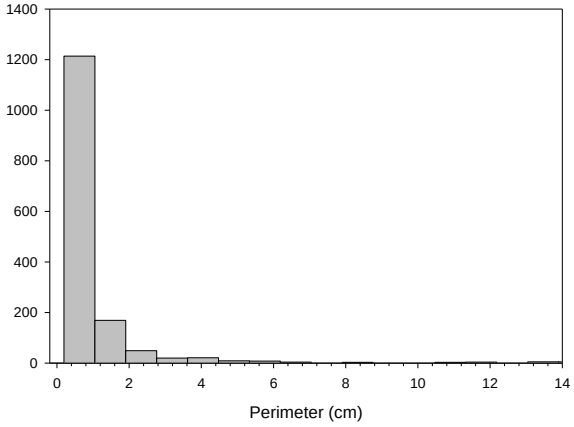
1400
1200
1000
800
600
400
200
0
0
2
4
6
8
10
12
14
Perimeter (cm)

H-7

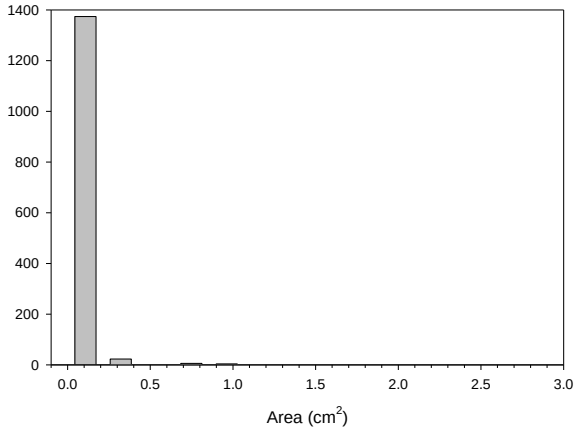
1400
1200
1000
800
600
400
200
0
0.0
0.5
1.0
1.5
2.0
2.5
3.0
Area (cm2)

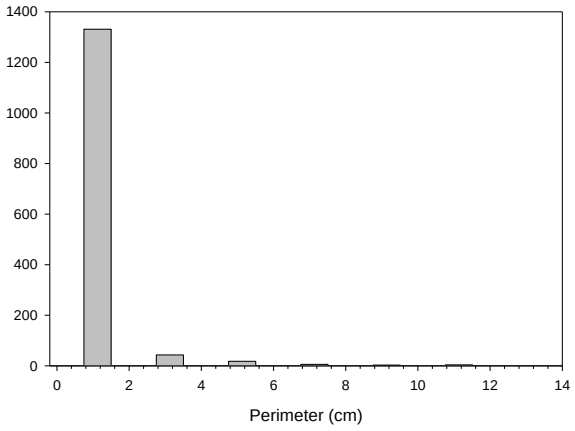
1400
1200
1000
800
600
400
200
0
0
2
4
6
8
10
12
14
Perimeter (cm)

H-8

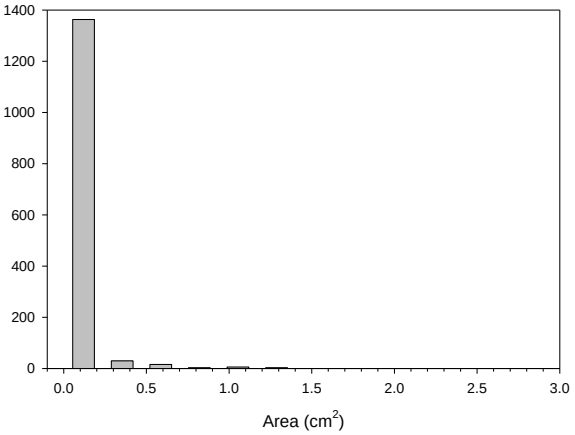
1400
1200
1000
800
600
400
200
0
0.0
0.5
1.0
1.5
2.0
2.5
3.0
Area (cm2)

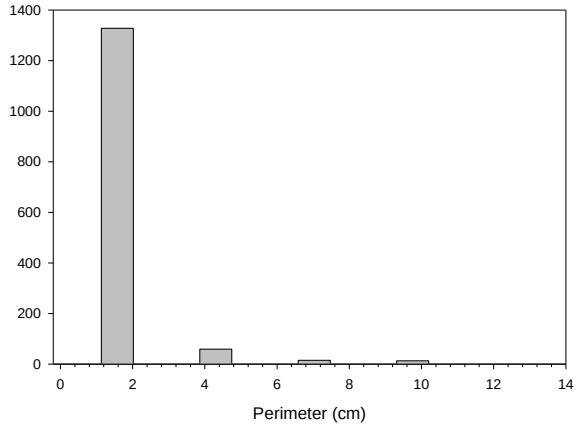
1400
1200
1000
800
600
400
200
0
0
2
4
6
8
10
12
14
Perimeter (cm)

HR-1

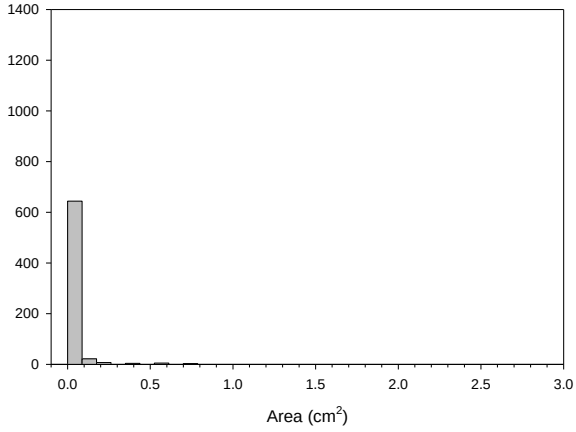
1400
1200
1000
800
600
400
200
0
0.0
0.5
1.0
1.5
2.0
2.5
3.0
Area (cm2)

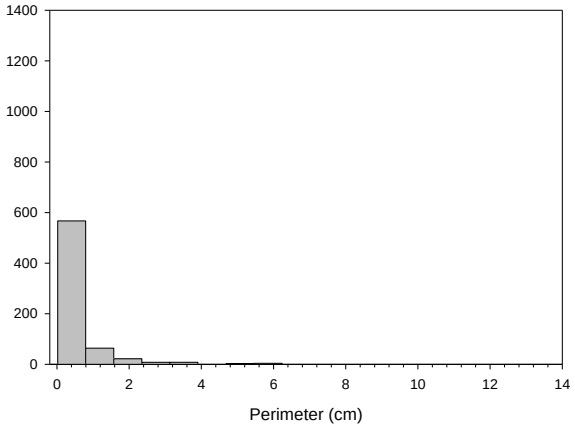
1400
1200
1000
800
600
400
200
0
0
2
4
6
8
10
12
14
Perimeter (cm)

HR-2

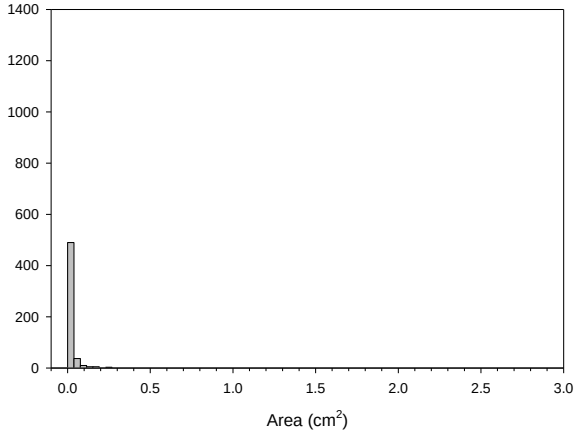
1400
1200
1000
800
600
400
200
0
0.0
0.5
1.0
1.5
2.0
2.5
3.0
Area (cm2)

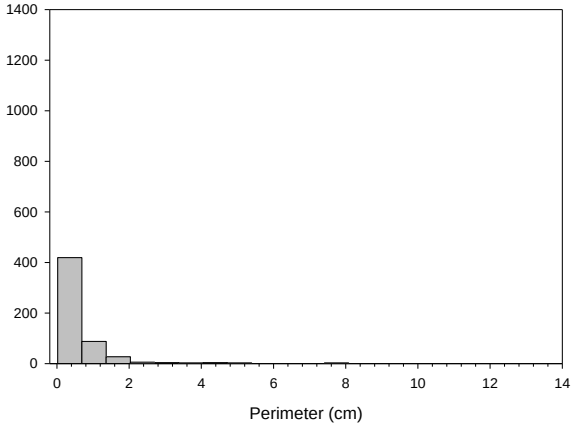
1400
1200
1000
800
600
400
200
0
0
2
4
6
8
10
12
14
Perimeter (cm)

HR-3

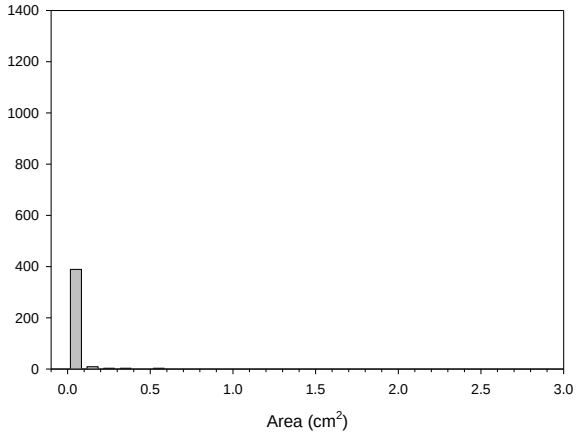
1400
1200
1000
800
600
400
200
0
0.0
0.5
1.0
1.5
2.0
2.5
3.0
Area (cm2)

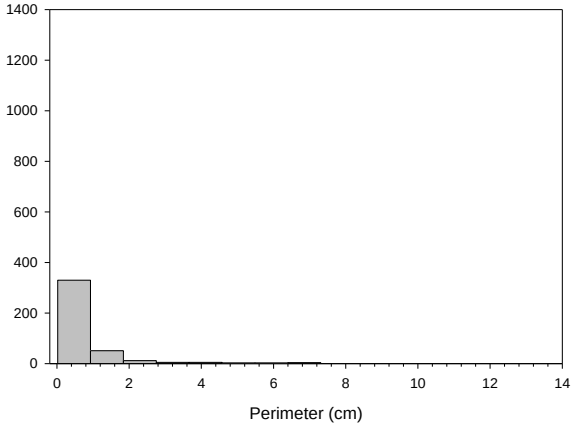
1400
1200
1000
800
600
400
200
0
0
2
4
6
8
10
12
14
Perimeter (cm)

HR-4

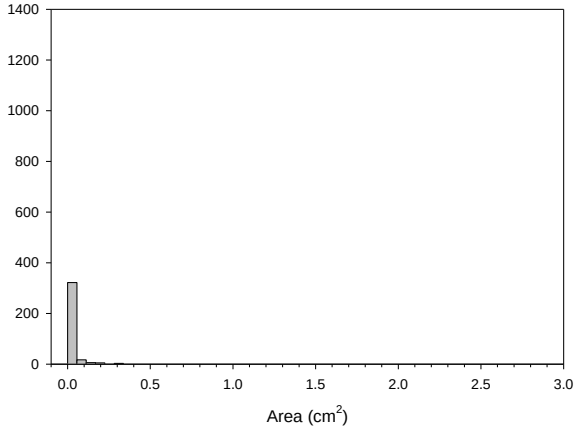
1400
1200
1000
800
600
400
200
0
0.0
0.5
1.0
1.5
2.0
2.5
3.0
Area (cm2)

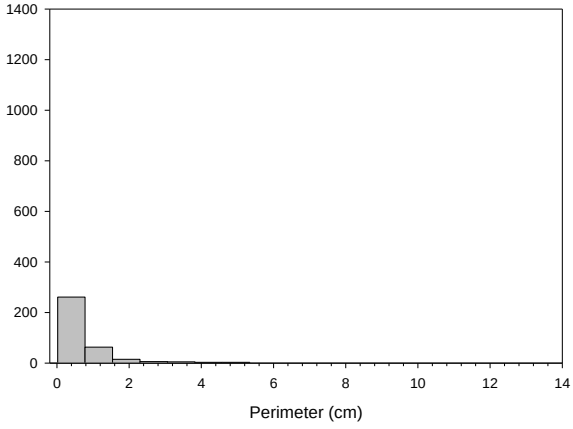
1400
1200
1000
800
600
400
200
0
0
2
4
6
8
10
12
14
Perimeter (cm)

HR-5

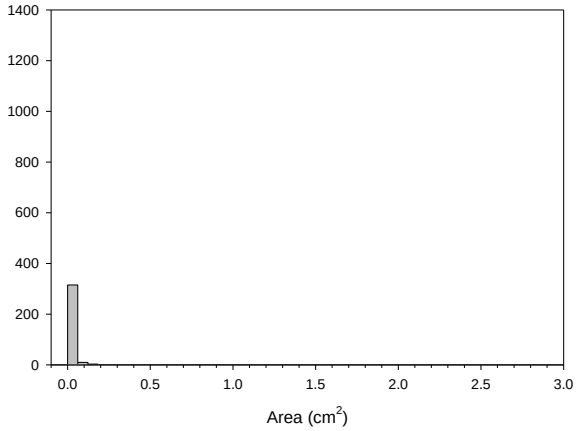
1400
1200
1000
800
600
400
200
0
0.0
0.5
1.0
1.5
2.0
2.5
3.0
Area (cm2)

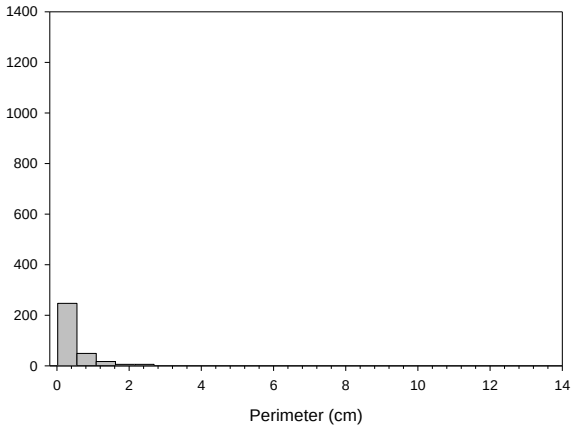
1400
1200
1000
800
600
400
200
0
0
2
4
6
8
10
12
14
Perimeter (cm)

HR-6

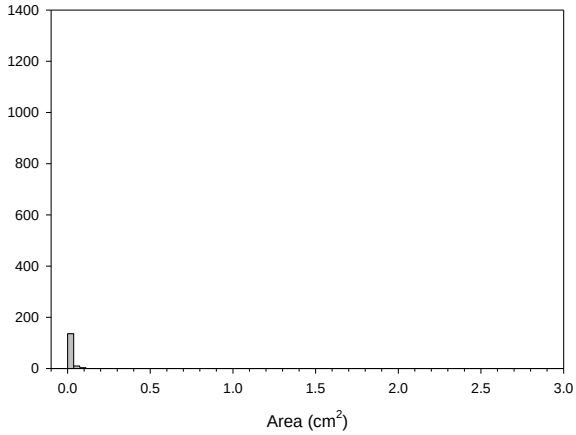
1400
1200
1000
800
600
400
200
0
0.0
0.5
1.0
1.5
2.0
2.5
3.0
Area (cm2)

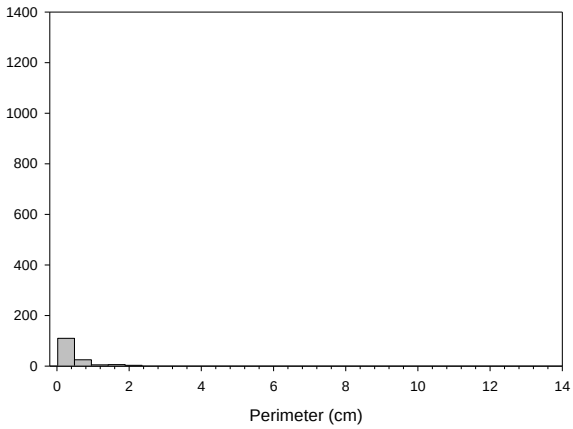
1400
1200
1000
800
600
400
200
0
0
2
4
6
8
10
12
14
Perimeter (cm)

HR-7

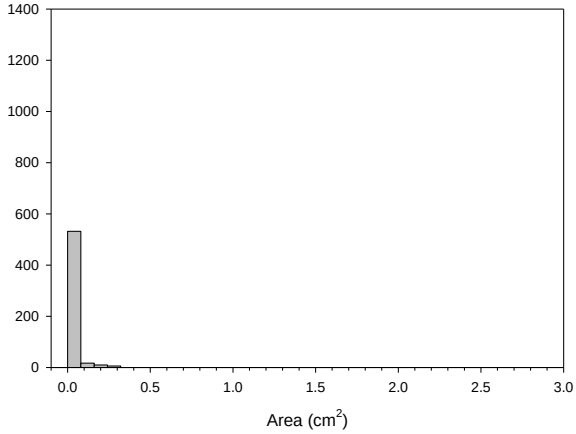
1400
1200
1000
800
600
400
200
0
0.0
0.5
1.0
1.5
2.0
2.5
3.0
Area (cm2)

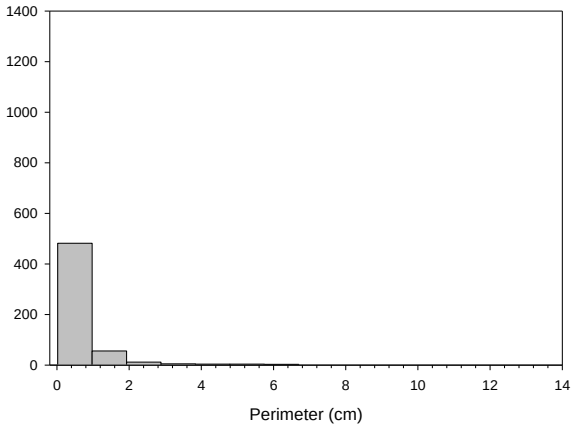
1400
1200
1000
800
600
400
200
0
0
2
4
6
8
10
12
14
Perimeter (cm)

HR-8

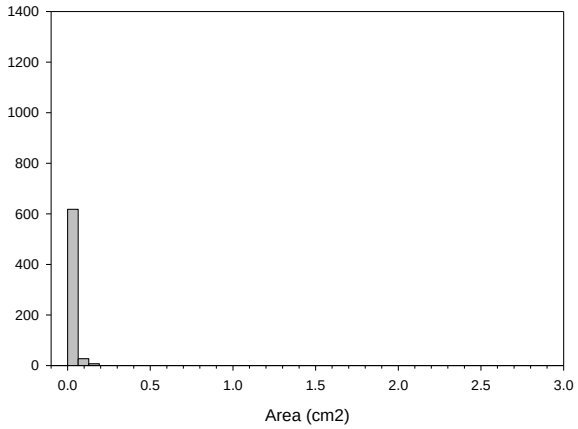
1400
1200
1000
800
600
400
200
0
0.0
0.5
1.0
1.5
2.0
2.5
3.0
Area (cm2)

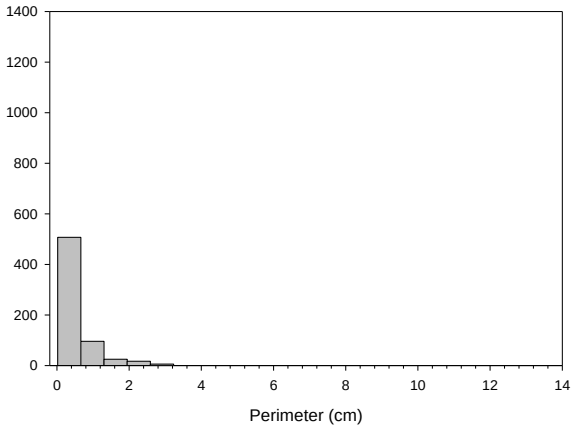
1400
1200
1000
800
600
400
200
0
0
2
4
6
8
10
12
14
Perimeter (cm)

Statistics from plots of pore area and perimeter distribution from CHAS core samples

H-1	Area (cm²)	Perimeter (cm)
Mean	0.0361	0.7686
Median	4.43E-03	0.2822
Std. Dev	0.1554	2.0829
Std. Err	4.54E-03	0.0609
95% Conf	8.91E-03	0.1194
99% Conf	0.0117	0.1571
Size	1171	1171
Total	42.24	900.0134
Min	1.70E-05	0.0189
Max	2.8722	49.3791
Min. Pos	1.70E-05	0.0189

H-2	Area (cm²)	Perimeter (cm)
Mean	0.057	1.0195
Median	5.76E-03	0.3464
Std. Dev	0.3011	3.6802
Std. Err	0.0106	0.1293
95% Conf	0.0208	0.2538
99% Conf	0.0273	0.3339
Size	810	810
Total	46.1494	825.7817
Min	1.70E-05	0.0189
Max	5.3894	71.5922
Min. Pos	1.70E-05	0.0189

H-3	Area (cm²)	Perimeter (cm)
Mean	0.0376	0.8262
Median	5.94E-03	0.3593
Std. Dev	0.1529	2.2043
Std. Err	5.30E-03	0.0765
95% Conf	0.0104	0.1501
99% Conf	0.0137	0.1974
Size	831	831
Total	31.2618	686.6016
Min	1.70E-05	0.0189
Max	3.2916	47.1615
Min. Pos	1.70E-05	0.0189

H-4	Area (cm²)	Perimeter (cm)
Mean	0.0485	0.9717
Median	6.36E-03	0.3887
Std. Dev	0.1844	2.4401
Std. Err	6.77E-03	0.0895
95% Conf	0.0133	0.1757
99% Conf	0.0175	0.2312
Size	743	743
Total	36.0706	722.0053
Min	1.70E-05	0.0189
Max	3.4183	43.2677
Min. Pos	1.70E-05	0.0189

H-5	Area (cm²)	Perimeter (cm)
Mean	0.0155	0.4712
Median	2.82E-03	0.2202
Std. Dev	0.0846	1.5511
Std. Err	2.92E-03	0.0536
95% Conf	5.74E-03	0.1052
99% Conf	7.55E-03	0.1384
Size	837	837
Total	12.9647	394.3727
Min	1.70E-05	0.0189
Max	2.1675	39.8265
Min. Pos	1.70E-05	0.0189

H-6	Area (cm²)	Perimeter (cm)
Mean	0.0507	1.0566
Median	0.0106	0.4742
Std. Dev	0.1637	2.1674
Std. Err	4.19E-03	0.0555
95% Conf	8.22E-03	0.1088
99% Conf	0.0108	0.1431
Size	1527	1527
Total	77.491	1613.3706
Min	2.60E-03	0.1938
Max	1.6271	25.8873
Min. Pos	2.60E-03	0.1938

H-7	Area (cm²)	Perimeter (cm)
Mean	0.04	0.8743
Median	6.32E-03	0.4023
Std. Dev	0.2407	2.5941
Std. Err	6.40E-03	0.069
95% Conf	0.0126	0.1353
99% Conf	0.0165	0.178
Size	1414	1414
Total	56.5004	1236.2365
Min	1.02E-03	0.1231
Max	6.4082	60.2095
Min. Pos	1.02E-03	0.1231

H-8	Area (cm²)	Perimeter (cm)
Mean	0.0639	1.2257
Median	0.0129	0.5614
Std. Dev	0.2765	3.2623
Std. Err	7.32E-03	0.0864
95% Conf	0.0144	0.1694
99% Conf	0.0189	0.2228
Size	1427	1427
Total	91.1496	1749.1297
Min	3.28E-03	0.2142
Max	7.0054	82.0094
Min. Pos	3.28E-03	0.2142

HR-1	Area (cm²)	Perimeter (cm)
Mean	0.0358	0.7649
Median	5.21E-03	0.313
Std. Dev	0.1527	1.8528
Std. Err	5.81E-03	0.0705
95% Conf	0.0114	0.1384
99% Conf	0.015	0.1821
Size	691	691
Total	24.7067	528.5784
Min	1.70E-05	0.0189
Max	2.6233	23.3432
Min. Pos	1.70E-05	0.0189

HR-2	Area (cm²)	Perimeter (cm)
Mean	0.0271	0.6792
Median	4.07E-03	0.2917
Std. Dev	0.0935	1.4295
Std. Err	3.94E-03	0.0602
95% Conf	7.74E-03	0.1183
99% Conf	0.0102	0.1557
Size	563	563
Total	15.2806	382.3876
Min	1.70E-05	0.0189
Max	1.151	20.1728
Min. Pos	1.70E-05	0.0189

HR-3	Area (cm²)	Perimeter (cm)
Mean	0.0529	0.9124
Median	5.53E-03	0.3459
Std. Dev	0.2203	2.3031
Std. Err	0.0108	0.1126
95% Conf	0.0212	0.2214
99% Conf	0.0279	0.2915
Size	418	418
Total	22.0972	381.3642
Min	1.70E-05	0.0189
Max	3.0104	27.3531
Min. Pos	1.70E-05	0.0189

HR-4	Area (cm²)	Perimeter (cm)
Mean	0.0531	1.0059
Median	5.86E-03	0.3473
Std. Dev	0.1949	2.5411
Std. Err	0.0102	0.1328
95% Conf	0.02	0.2612
99% Conf	0.0264	0.344
Size	366	366
Total	19.4529	368.1414
Min	1.60E-05	0.0187
Max	1.6893	22.8367
Min. Pos	1.60E-05	0.0187

HR-5	Area (cm²)	Perimeter (cm)
Mean	0.0245	0.566
Median	2.35E-03	0.2359
Std. Dev	0.1198	1.2485
Std. Err	6.55E-03	0.0682
95% Conf	0.0129	0.1342
99% Conf	0.017	0.1767
Size	335	335
Total	8.1975	189.6172
Min	1.60E-05	0.0187
Max	1.8428	16.0487
Min. Pos	1.60E-05	0.0187

HR-6	Area (cm²)	Perimeter (cm)
Mean	0.0322	0.6562
Median	2.21E-03	0.2246
Std. Dev	0.1345	1.5719
Std. Err	0.0108	0.1263
95% Conf	0.0213	0.2494
99% Conf	0.0282	0.3293
Size	155	155
Total	4.9884	101.711
Min	1.70E-05	0.0189
Max	1.1037	14.0599
Min. Pos	1.70E-05	0.0189

HR-7	Area (cm²)	Perimeter (cm)
Mean	0.0288	0.7246
Median	4.93E-03	0.3303
Std. Dev	0.129	1.7933
Std. Err	5.40E-03	0.0751
95% Conf	0.0106	0.1475
99% Conf	0.014	0.1941
Size	570	570
Total	16.4026	413.009
Min	1.70E-05	0.0189
Max	2.4102	28.6549
Min. Pos	1.70E-05	0.0189

HR-8	Area (cm²)	Perimeter (cm)
Mean	0.0208	0.5688
Median	3.14E-03	0.2808
Std. Dev	0.0987	1.2701
Std. Err	3.85E-03	0.0495
95% Conf	7.55E-03	0.0972
99% Conf	9.94E-03	0.1278
Size	659	659
Total	13.7237	374.8382
Min	1.70E-05	0.0189
Max	1.9181	19.2902
Min. Pos	1.70E-05	0.0189

Plots of pore area and perimeter distribution from Biscayne core samples

1-6

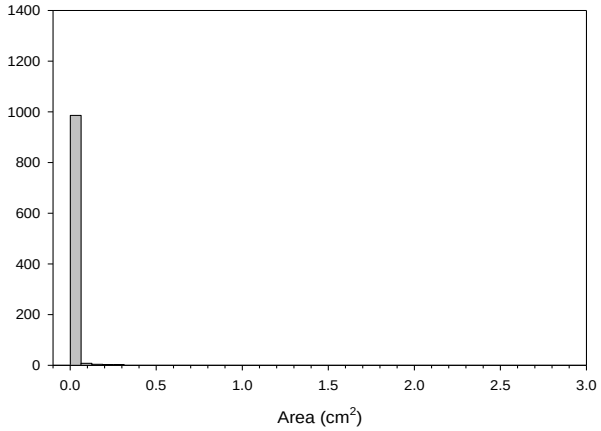

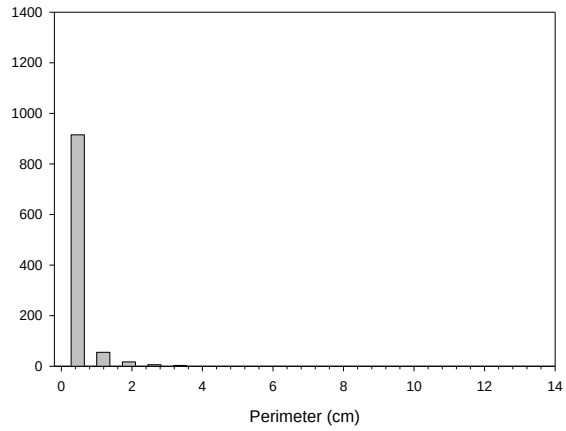

1-10

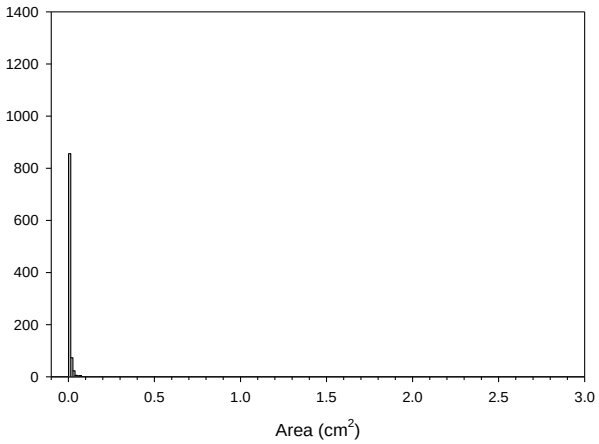

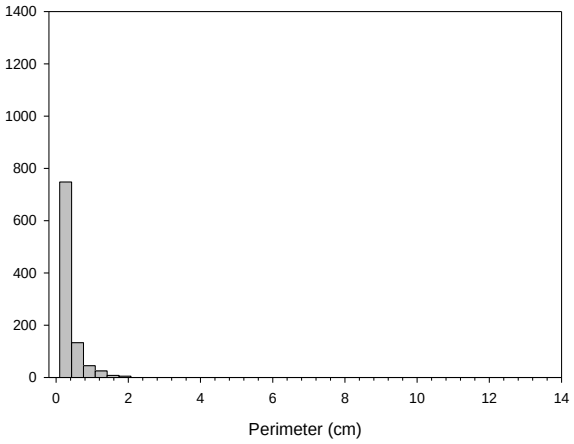

1-12

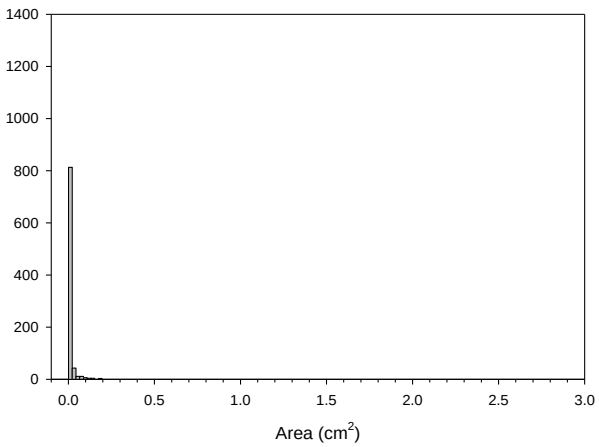

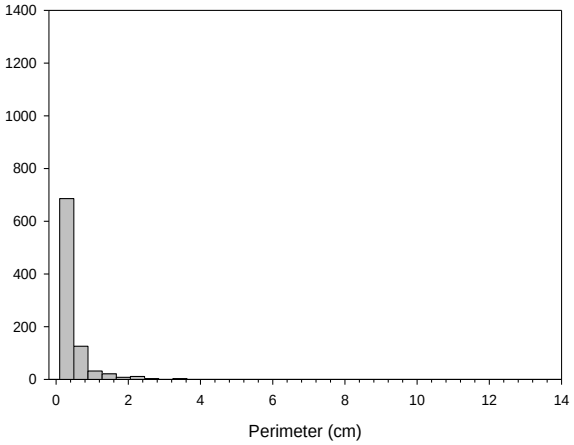

1-15

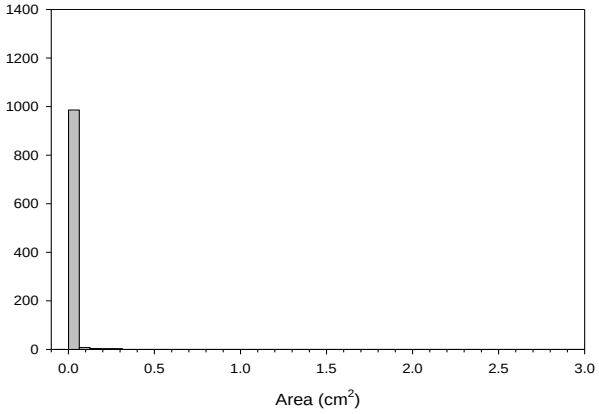
1400
1200
1000
800
600
400
200
0
0.0
0.5
1.0
1.5
2.0
2.5
3.0
Area (cm2)

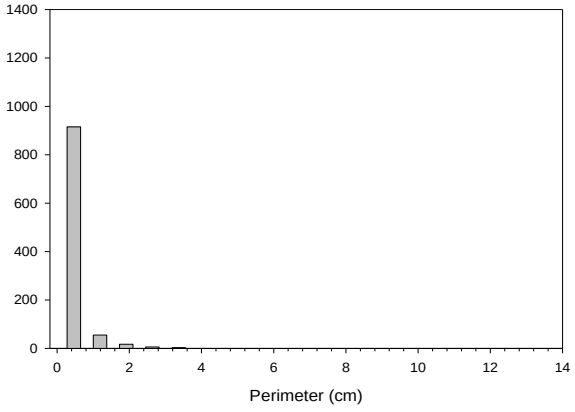
1400
1200
1000
800
600
400
200
0
0
2
4
6
8
10
12
14
Perimeter (cm)

1-19

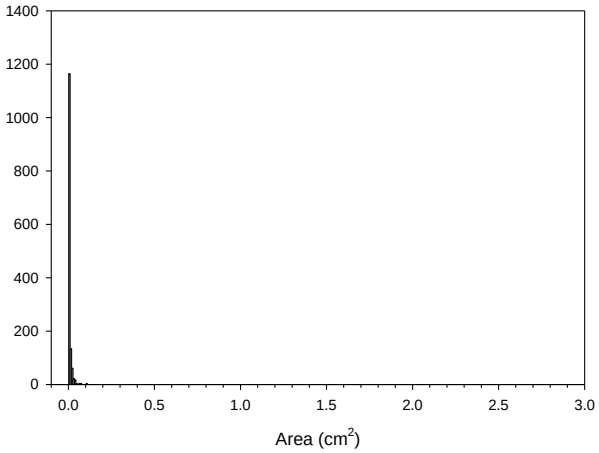
1400
1200
1000
800
600
400
200
0
0.0
0.5
1.0
1.5
2.0
2.5
3.0
Area (cm2)

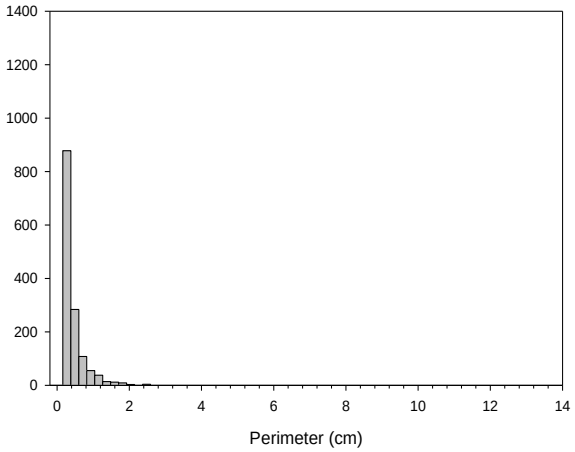
1400
1200
1000
800
600
400
200
0
0
2
4
6
8
10
12
14
Perimeter (cm)

2-3

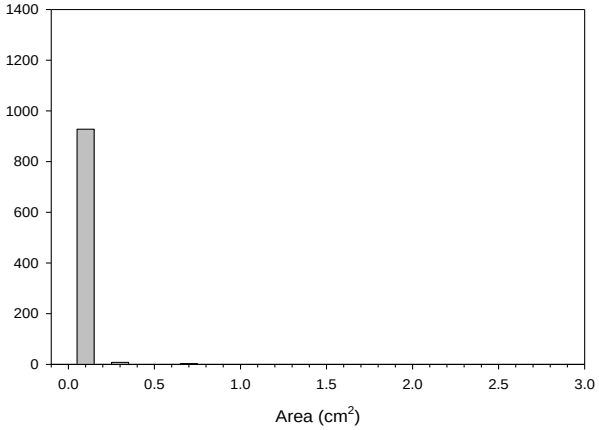
1400
1200
1000
800
600
400
200
0
0.0
0.5
1.0
1.5
2.0
2.5
3.0
Area (cm2)

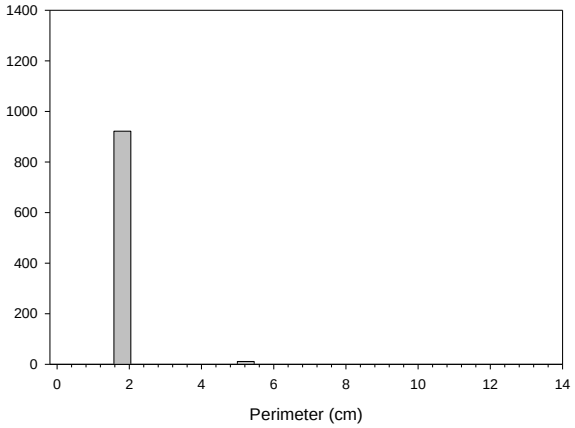
1400
1200
1000
800
600
400
200
0
0
2
4
6
8
10
12
14
Perimeter (cm)

2-4

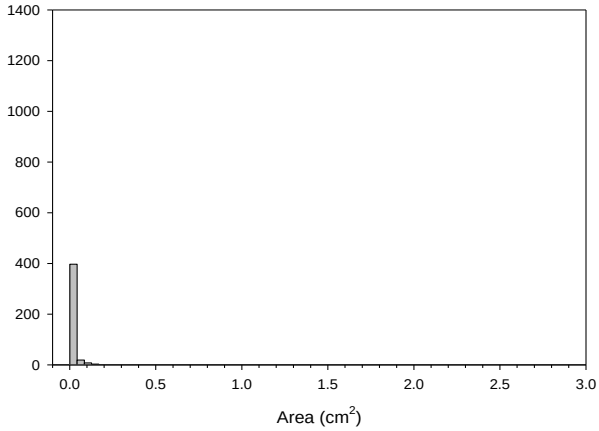
1400
1200
1000
800
600
400
200
0
0.0
0.5
1.0
1.5
2.0
2.5
3.0
Area (cm2)

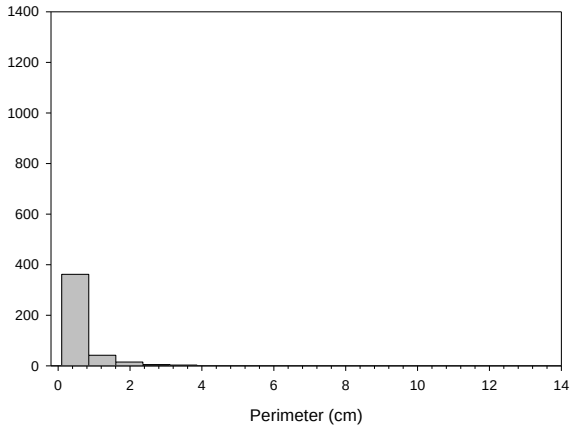
1400
1200
1000
800
600
400
200
0
0
2
4
6
8
10
12
14
Perimeter (cm)

2-6

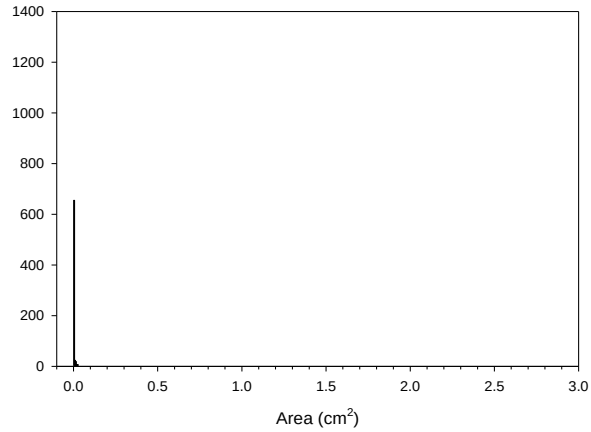
1400
1200
1000
800
600
400
200
0
0.0
0.5
1.0
1.5
2.0
2.5
3.0
Area (cm2)

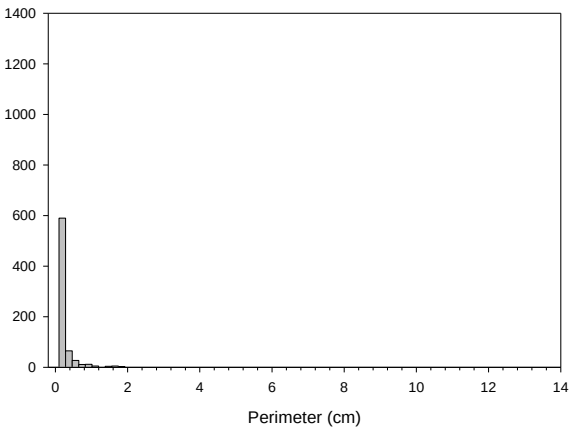
1400
1200
1000
800
600
400
200
0
0
2
4
6
8
10
12
14
Perimeter (cm)

2-11

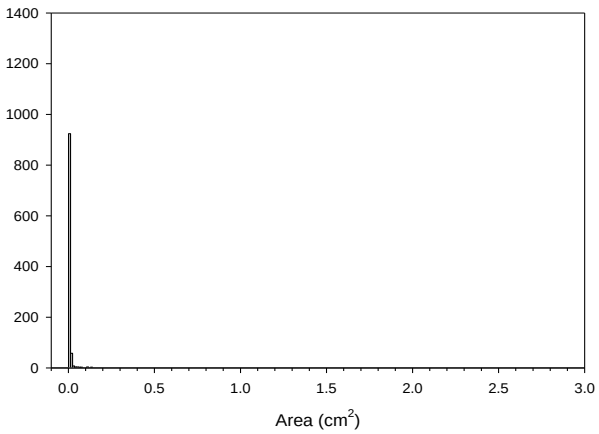
1400
1200
1000
800
600
400
200
0
0.0
0.5
1.0
1.5
2.0
2.5
3.0
Area (cm2)

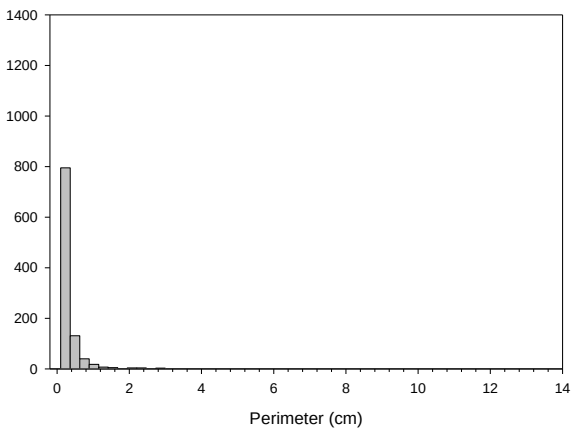
1400
1200
1000
800
600
400
200
0
0
2
4
6
8
10
12
14
Perimeter (cm)

3-1

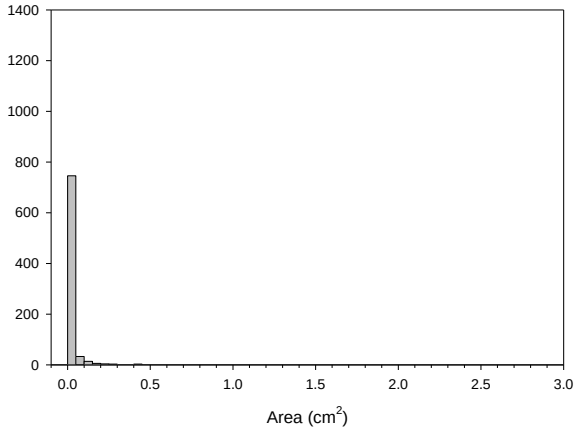
1400
1200
1000
800
600
400
200
0
0.0
0.5
1.0
1.5
2.0
2.5
3.0
Area (cm2)

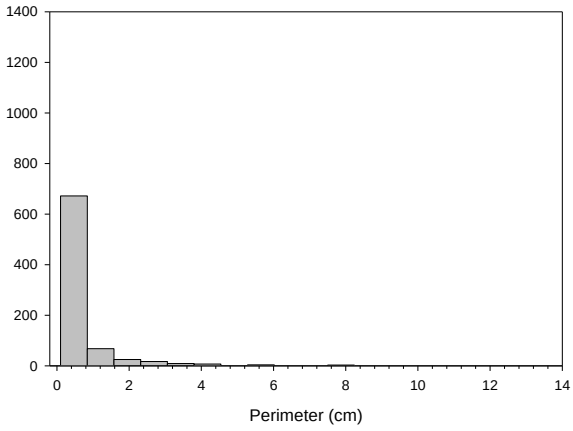
1400
1200
1000
800
600
400
200
0
0
2
4
6
8
10
12
14
Perimeter (cm)

3-2

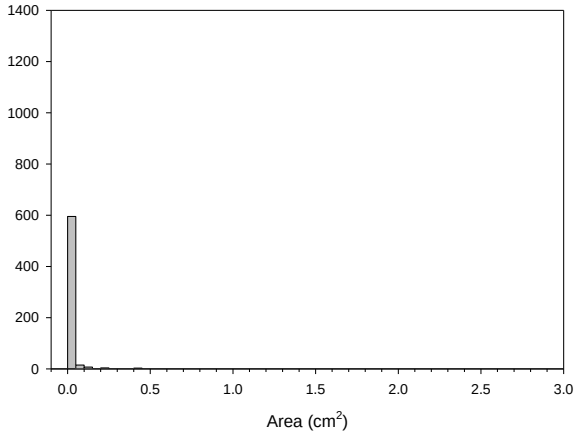
1400
1200
1000
800
600
400
200
0
0.0
0.5
1.0
1.5
2.0
2.5
3.0
Area (cm2)

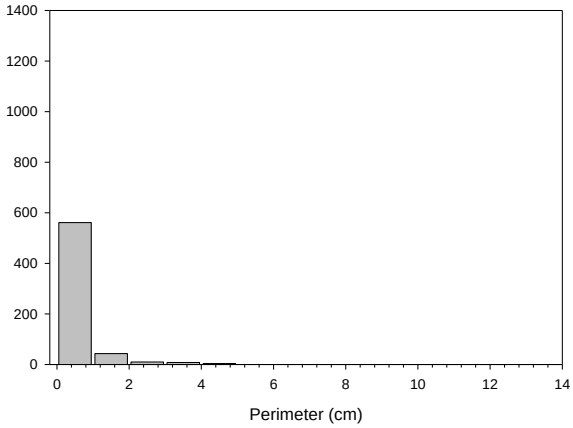
1400
1200
1000
800
600
400
200
0
0
2
4
6
8
10
12
14
Perimeter (cm)

3-3

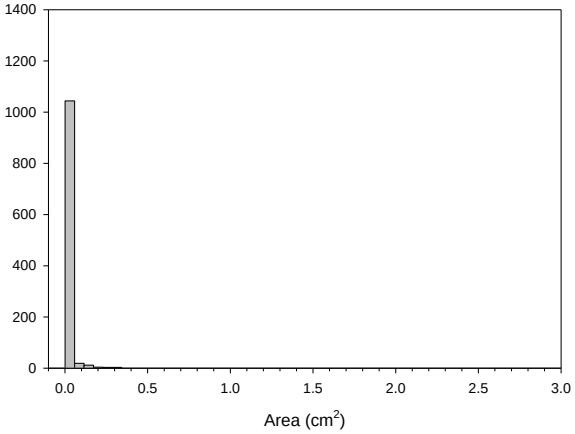
1400
1200
1000
800
600
400
200
0
0.0
0.5
1.0
1.5
2.0
2.5
3.0
Area (cm2)

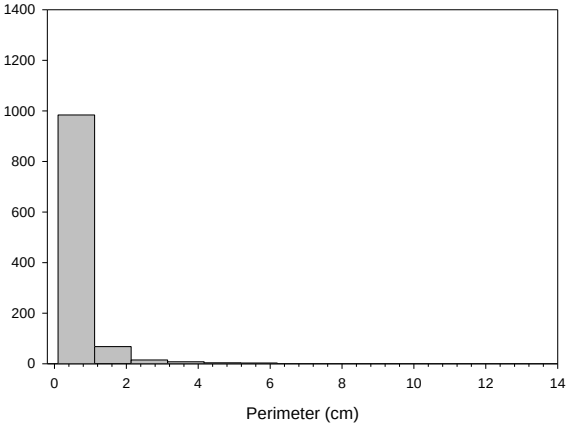
1400
1200
1000
800
600
400
200
0
0
2
4
6
8
10
12
14
Perimeter (cm)

3-12

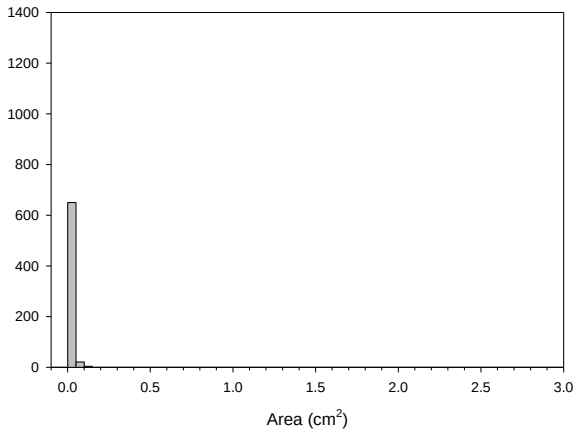
1400
1200
1000
800
600
400
200
0
0.0
0.5
1.0
1.5
2.0
2.5
3.0
Area (cm2)

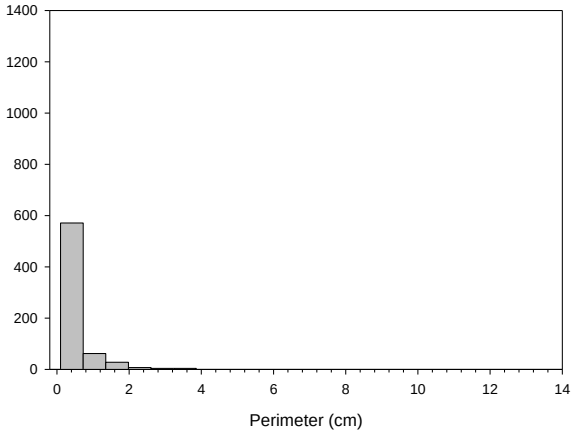
1400
1200
1000
800
600
400
200
0
0
2
4
6
8
10
12
14
Perimeter (cm)

3-15

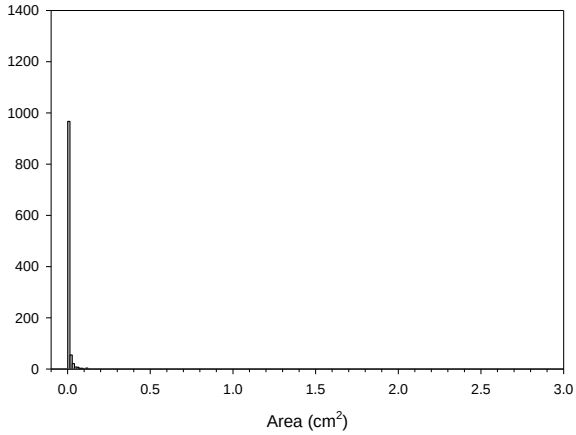
1400
1200
1000
800
600
400
200
0
0.0
0.5
1.0
1.5
2.0
2.5
3.0
Area (cm2)

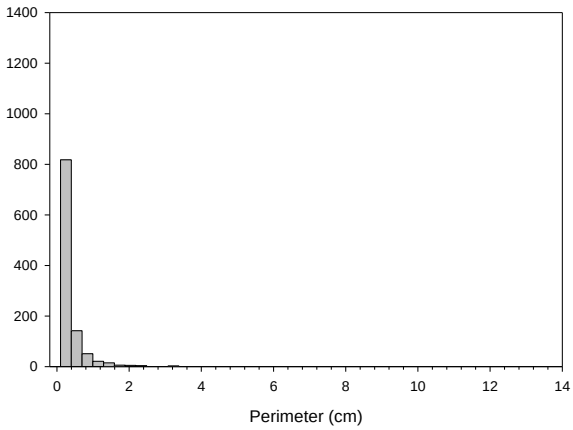
1400
1200
1000
800
600
400
200
0
0
2
4
6
8
10
12
14
Perimeter (cm)

4-4

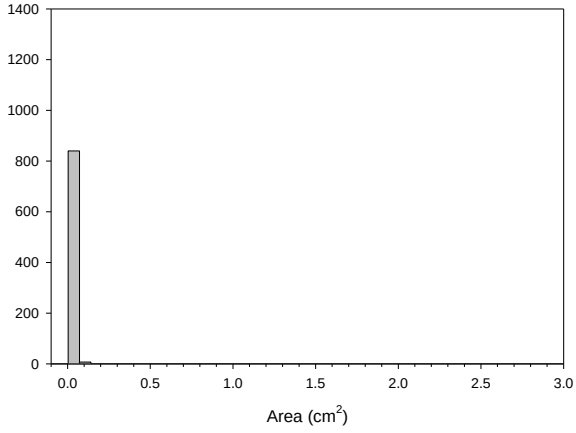
1400
1200
1000
800
600
400
200
0
0.0
0.5
1.0
1.5
2.0
2.5
3.0
Area (cm2)

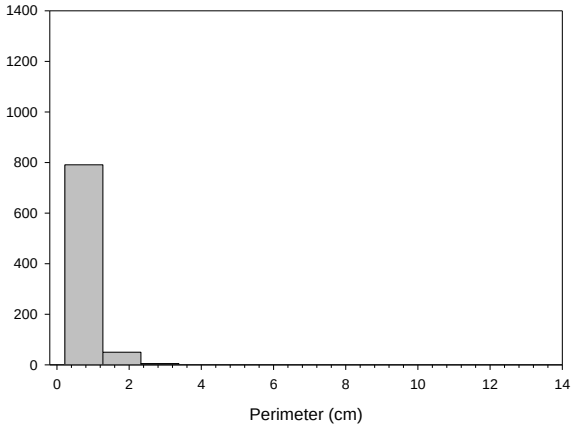
1400
1200
1000
800
600
400
200
0
0
2
4
6
8
10
12
14
Perimeter (cm)

4-7

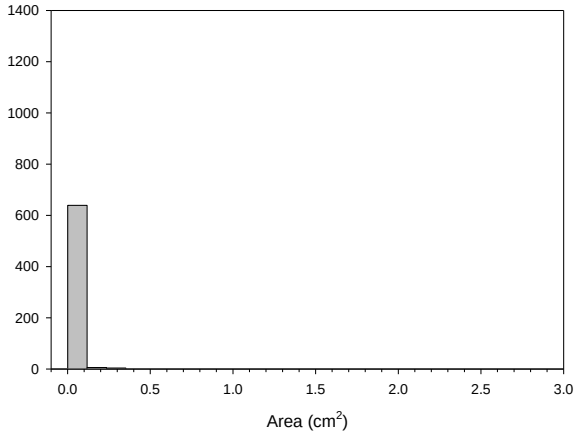
1400
1200
1000
800
600
400
200
0
0.0
0.5
1.0
1.5
2.0
2.5
3.0
Area (cm2)

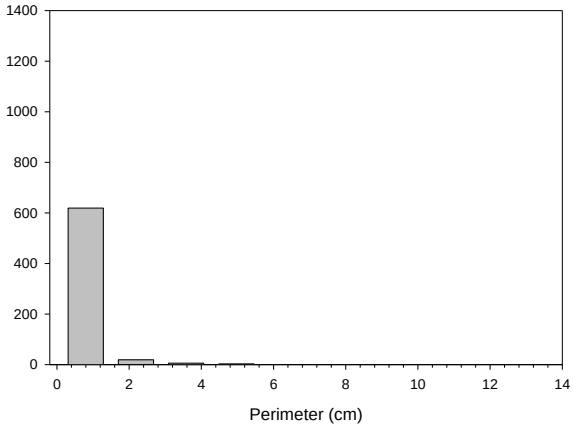
1400
1200
1000
800
600
400
200
0
0
2
4
6
8
10
12
14
Perimeter (cm)

4-15

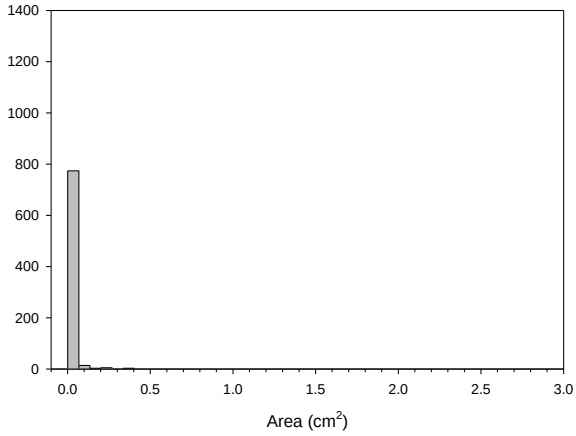
1400
1200
1000
800
600
400
200
0
0.0
0.5
1.0
1.5
2.0
2.5
3.0
Area (cm2)

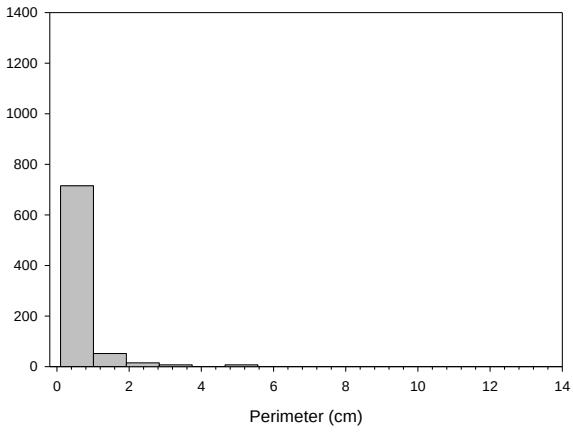
1400
1200
1000
800
600
400
200
0
0
2
4
6
8
10
12
14
Perimeter (cm)

5-5

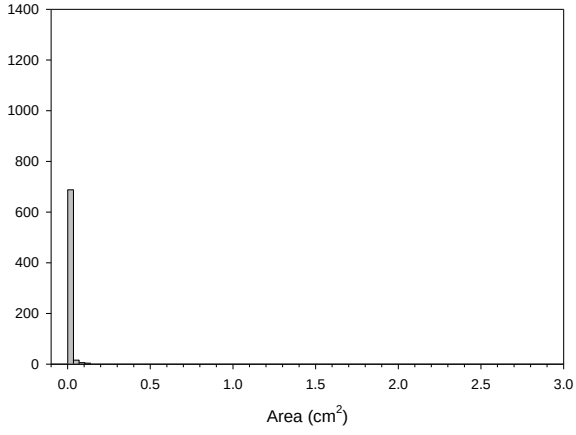
1400
1200
1000
800
600
400
200
0
0.0
0.5
1.0
1.5
2.0
2.5
3.0
Area (cm2)

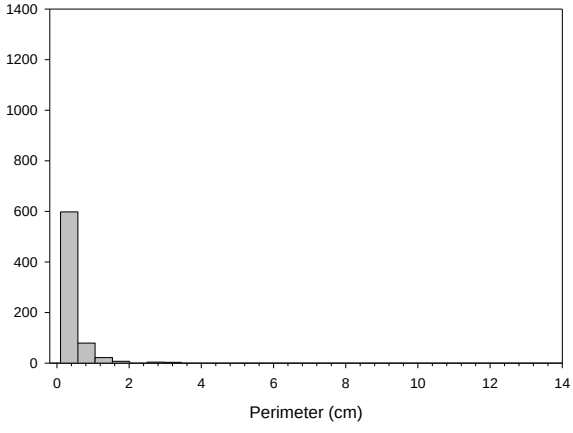
1400
1200
1000
800
600
400
200
0
0
2
4
6
8
10
12
14
Perimeter (cm)

5-10

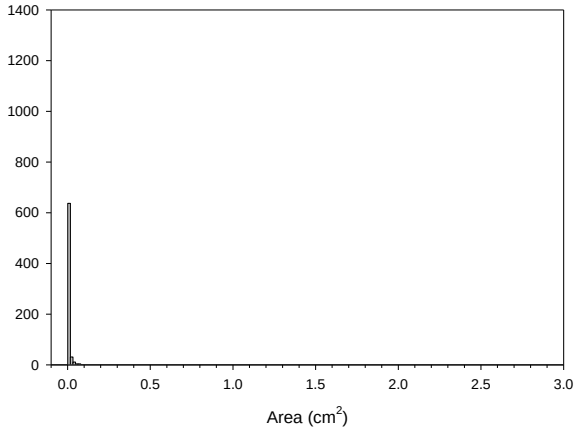
1400
1200
1000
800
600
400
200
0
0.0
0.5
1.0
1.5
2.0
2.5
3.0
Area (cm2)

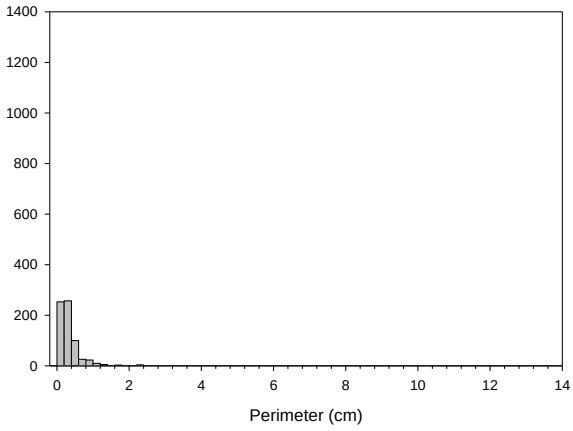
1400
1200
1000
800
600
400
200
0
0
2
4
6
8
10
12
14
Perimeter (cm)

5-12

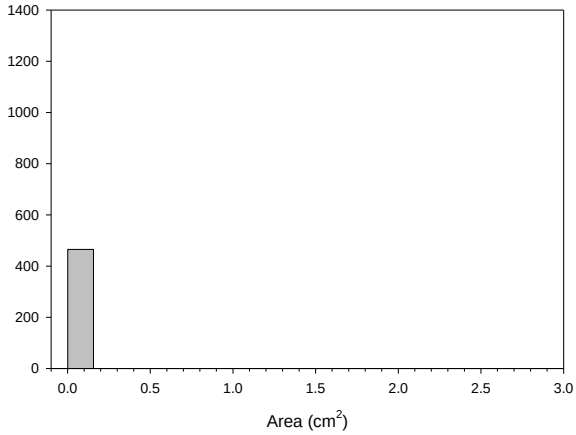
1400
1200
1000
800
600
400
200
0
0.0
0.5
1.0
1.5
2.0
2.5
3.0
Area (cm2)

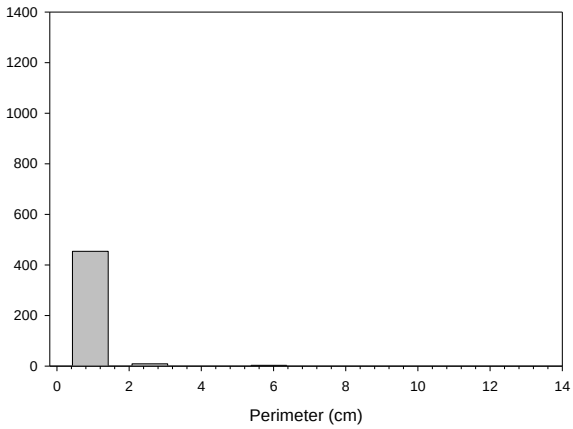
1400
1200
1000
800
600
400
200
0
0
2
4
6
8
10
12
14
Perimeter (cm)

6-3

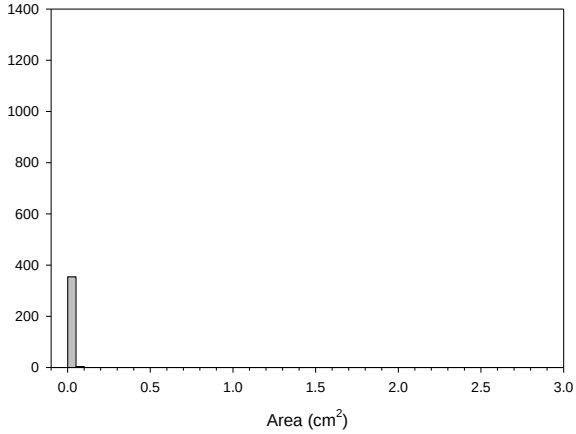
1400
1200
1000
800
600
400
200
0
0.0
0.5
1.0
1.5
2.0
2.5
3.0
Area (cm2)

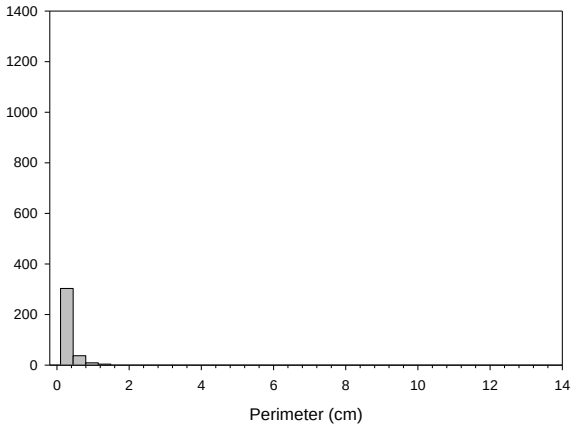
1400
1200
1000
800
600
400
200
0
0
2
4
6
8
10
12
14
Perimeter (cm)

6-6

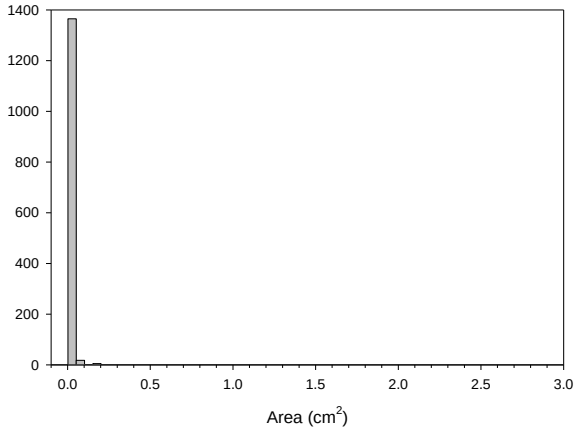
1400
1200
1000
800
600
400
200
0
0.0
0.5
1.0
1.5
2.0
2.5
3.0
Area (cm2)

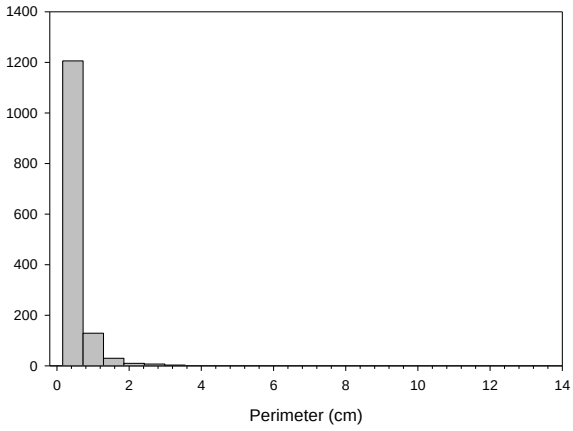
1400
1200
1000
800
600
400
200
0
0
2
4
6
8
10
12
14
Perimeter (cm)

6-7

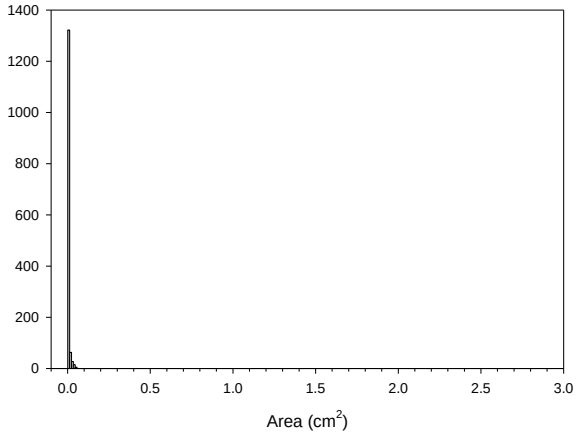
1400
1200
1000
800
600
400
200
0
0.0
0.5
1.0
1.5
2.0
2.5
3.0
Area (cm2)

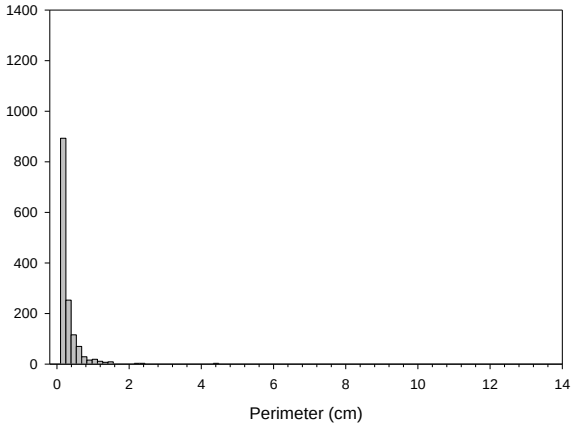
1400
1200
1000
800
600
400
200
0
0
2
4
6
8
10
12
14
Perimeter (cm)

6-10

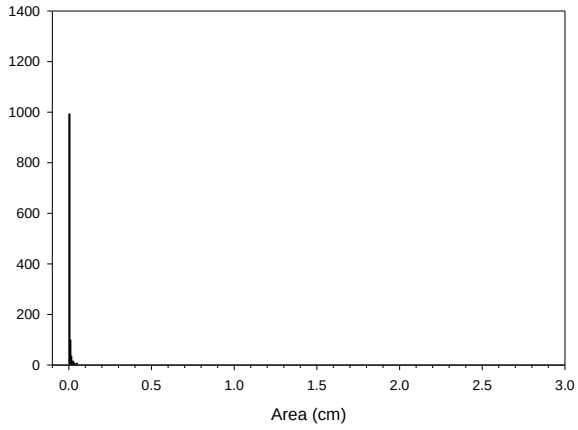
1400
1200
1000
800
600
400
200
0
0.0
0.5
1.0
1.5
2.0
2.5
3.0
Area (cm)

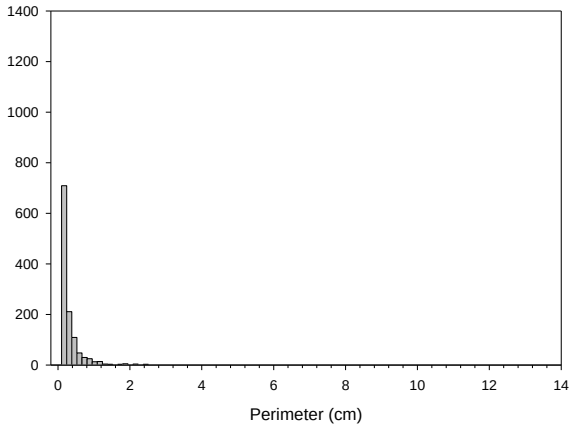
1400
1200
1000
800
600
400
200
0
0
2
4
6
8
10
12
14
Perimeter (cm)

6-13

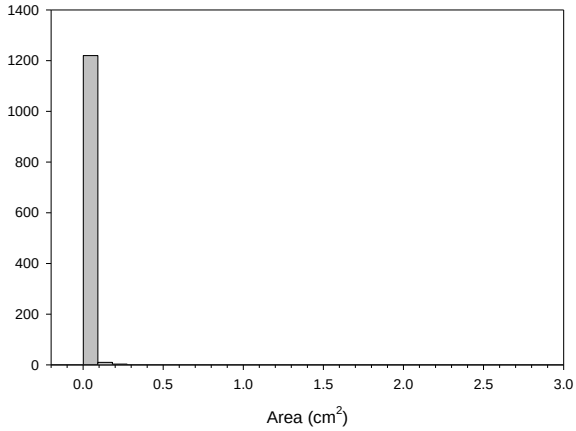
1400
1200
1000
800
600
400
200
0
0.0
0.5
1.0
1.5
2.0
2.5
3.0
Area (cm2)

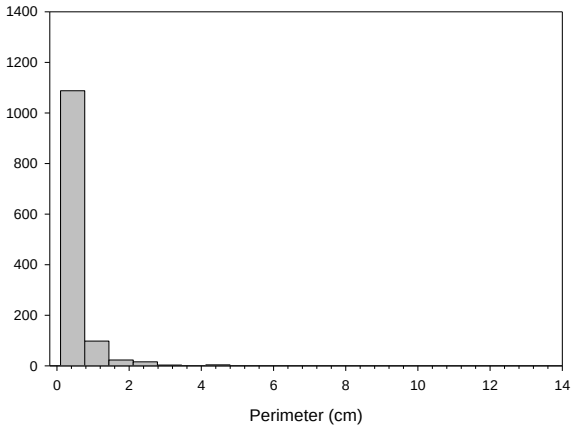
1400
1200
1000
800
600
400
200
0
0
2
4
6
8
10
12
14
Perimeter (cm)

Statistics from plots of pore area and perimeter distribution from Biscayne core samples

1_6	Area (cm²)	Perimeter (cm)
Mean	0.0115	0.4525
Median	2.00E-03	0.24
Std. Dev	0.0678	0.9738
Std. Err	2.14E-03	0.0307
95% Conf	4.20E-03	0.0602
99% Conf	5.52E-03	0.0792
Size	1007	1007
Total	11.602	455.7
Min	1.00E-03	0.1
Max	1.877	21.88
Min. Pos	1.00E-03	0.1

1_10	Area (cm²)	Perimeter (cm)
Mean	7.14E-03	0.3768
Median	2.00E-03	0.22
Std. Dev	0.0208	0.5509
Std. Err	6.66E-04	0.0176
95% Conf	1.31E-03	0.0346
99% Conf	1.72E-03	0.0455
Size	976	976
Total	6.973	367.72
Min	1.00E-03	0.1
Max	0.376	9.96
Min. Pos	1.00E-03	0.1

1_12	Area (cm²)	Perimeter (cm)
Mean	0.0117	0.4591
Median	2.00E-03	0.24
Std. Dev	0.04	0.7819
Std. Err	1.33E-03	0.0261
95% Conf	2.62E-03	0.0512
99% Conf	3.45E-03	0.0673
Size	900	900
Total	10.487	413.16
Min	1.00E-03	0.1
Max	0.652	11.86
Min. Pos	1.00E-03	0.1

1_15	Area (cm²)	Perimeter (cm)
Mean	0.0142	0.5455
Median	4.00E-03	0.32
Std. Dev	0.0438	0.9224
Std. Err	1.91E-03	0.0402
95% Conf	3.75E-03	0.0789
99% Conf	4.93E-03	0.1039
Size	527	527
Total	7.503	287.46
Min	1.00E-03	0.1
Max	0.734	14.84
Min. Pos	1.00E-03	0.1

1_19	Area (cm²)	Perimeter (cm)
Mean	7.88E-03	0.4656
Median	4.00E-03	0.32
Std. Dev	0.0131	0.4561
Std. Err	3.48E-04	0.0121
95% Conf	6.83E-04	0.0237
99% Conf	8.98E-04	0.0312
Size	2201	2201
Total	11.19	661.2
Min	2.00E-03	0.16
Max	0.252	6.78
Min. Pos	2.00E-03	0.16

2_3	Area (cm²)	Perimeter (cm)
Mean	0.0238	0.7432
Median	2.00E-03	0.22
Std. Dev	0.2295	4.0718
Std. Err	7.48E-03	0.1327
95% Conf	1.47E-02	0.2604
99% Conf	0.0193	0.3424
Size	942	942
Total	22.432	700.06
Min	1.00E-03	0.1
Max	5.837	102.62
Min. Pos	1.00E-03	0.1

2_4	Area (cm²)	Perimeter (cm)
Mean	0.017	0.5965
Median	4.00E-03	0.32
Std. Dev	0.0661	1.2343
Std. Err	3.19E-03	0.0595
95% Conf	6.26E-03	0.1169
99% Conf	8.24E-03	0.1538
Size	431	431
Total	7.322	257.1
Min	1.00E-03	0.1
Max	1.26	22.68
Min. Pos	1.00E-03	0.1

2_6	Area (cm²)	Perimeter (cm)
Mean	3.82E-03	0.2654
Median	1.00E-03	0.16
Std. Dev	0.0107	0.3679
Std. Err	3.96E-04	0.0136
95% Conf	7.78E-04	0.0268
99% Conf	1.02E-03	0.0352
Size	729	729
Total	2.787	193.5
Min	1.00E-03	0.1
Max	0.162	5.58
Min. Pos	1.00E-03	0.1

2_11	Area (cm²)	Perimeter (cm)
Mean	6.07E-03	0.3318
Median	2.00E-03	0.2
Std. Dev	0.0193	0.4977
Std. Err	6.05E-04	0.0156
95% Conf	1.19E-03	0.0306
99% Conf	1.56E-03	0.0403
Size	1016	1016
Total	6.164	337.08
Min	1.00E-03	0.1
Max	0.349	8
Min. Pos	1.00E-03	0.1

3_1	Area (cm²)	Perimeter (cm)
Mean	0.0261	0.7785
Median	3.00E-03	0.26
Std. Dev	0.1119	1.8935
Std. Err	3.91E-03	0.0661
95% Conf	7.67E-03	0.1298
99% Conf	0.0101	0.1707
Size	820	820
Total	21.381	638.4
Min	1.00E-03	0.1
Max	1.483	22.3
Min. Pos	1.00E-03	0.1

3_2	Area (cm²)	Perimeter (cm)
Mean	0.0234	0.617
Median	2.00E-03	0.24
Std. Dev	0.1043	1.6105
Std. Err	4.14E-03	0.0639
95% Conf	8.12E-03	0.1255
99% Conf	0.0107	0.1651
Size	635	635
Total	14.83	391.78
Min	1.00E-03	0.1
Max	1.132	19.68
Min. Pos	1.00E-03	0.1

3_3	Area (cm²)	Perimeter (cm)
Mean	0.0146	0.5568
Median	3.00E-03	0.28
Std. Dev	0.063	1.2551
Std. Err	1.91E-03	0.038
95% Conf	3.74E-03	0.0746
99% Conf	4.92E-03	0.0981
Size	1089	1089
Total	15.884	606.34
Min	1.00E-03	0.1
Max	1.714	30.58
Min. Pos	1.00E-03	0.1

3_12	Area (cm²)	Perimeter (cm)
Mean	0.0157	0.5479
Median	2.00E-03	0.26
Std. Dev	0.0734	1.0987
Std. Err	2.80E-03	0.042
95% Conf	5.50E-03	0.0824
99% Conf	7.24E-03	0.1084
Size	685	685
Total	10.769	375.3
Min	1.00E-03	0.1
Max	1.494	18.9
Min. Pos	1.00E-03	0.1

3_15	Area (cm²)	Perimeter (cm)
Mean	7.99E-03	0.4012
Median	2.00E-03	0.22
Std. Dev	0.0264	0.6986
Std. Err	8.04E-04	0.0213
95% Conf	1.58E-03	0.0418
99% Conf	2.07E-03	0.0549
Size	1077	1077
Total	8.608	432.1
Min	1.00E-03	0.1
Max	0.407	9.04
Min. Pos	1.00E-03	0.1

4_4	Area (cm²)	Perimeter (cm)
Mean	0.0156	0.6313
Median	6.00E-03	0.4
Std. Dev	0.0915	1.3572
Std. Err	3.14E-03	0.0465
95% Conf	6.15E-03	0.0913
99% Conf	8.10E-03	0.12
Size	2255	2255
Total	13.317	537.88
Min	3.00E-03	0.22
Max	2.074	31.8
Min. Pos	3.00E-03	0.22

4_7	Area (cm²)	Perimeter (cm)
Mean	0.0174	0.5312
Median	3.00E-03	0.26
Std. Dev	0.1407	1.7587
Std. Err	5.52E-03	0.069
95% Conf	1.08E-02	0.1355
99% Conf	0.0143	0.1782
Size	650	650
Total	11.3	345.3
Min	1.00E-03	0.1
Max	3.513	41.86
Min. Pos	1.00E-03	0.1

4_15	Area (cm²)	Perimeter (cm)
Mean	0.018	0.622
Median	3.00E-03	0.32
Std. Dev	0.0946	1.516
Std. Err	3.34E-03	0.0535
95% Conf	6.56E-03	0.105
99% Conf	8.62E-03	0.1381
Size	803	803
Total	14.431	499.44
Min	1.00E-03	0.1
Max	2.014	27.44
Min. Pos	1.00E-03	0.1

5_5	Area (cm²)	Perimeter (cm)
Mean	9.68E-03	0.4284
Median	3.00E-03	0.28
Std. Dev	0.0423	0.6798
Std. Err	1.58E-03	0.0254
95% Conf	3.10E-03	0.0498
99% Conf	4.07E-03	0.0655
Size	718	718
Total	6.947	307.62
Min	1.00E-03	0.1
Max	1.031	14.46
Min. Pos	1.00E-03	0.1

5_10	Area (cm²)	Perimeter (cm)
Mean	8.21E-03	0.385
Median	3.00E-03	0.24
Std. Dev	0.0277	0.512
Std. Err	1.05E-03	0.0194
95% Conf	2.07E-03	0.0381
99% Conf	2.72E-03	0.0502
Size	695	695
Total	5.706	267.58
Min	1.00E-03	0.1
Max	0.471	5.84
Min. Pos	1.00E-03	0.1

5_12	Area (cm²)	Perimeter (cm)
Mean	0.0283	0.6021
Median	2.00E-03	0.22
Std. Dev	0.2612	2.7647
Std. Err	1.20E-02	0.1273
95% Conf	2.36E-02	0.2501
99% Conf	0.0311	0.3291
Size	472	472
Total	13.354	284.18
Min	1.00E-03	0.1
Max	4.661	49.56
Min. Pos	1.00E-03	0.1

6_3	Area (cm²)	Perimeter (cm)
Mean	0.0124	0.3919
Median	2.00E-03	0.18
Std. Dev	0.0868	0.9419
Std. Err	4.55E-03	0.0494
95% Conf	8.95E-03	0.0971
99% Conf	0.0118	0.1278
Size	364	364
Total	4.523	142.64
Min	1.00E-03	0.1
Max	1.495	10.56
Min. Pos	1.00E-03	0.1

6_6	Area (cm²)	Perimeter (cm)
Mean	0.0105	0.5078
Median	4.00E-03	0.32
Std. Dev	0.0509	0.8125
Std. Err	1.36E-03	0.0217
95% Conf	2.67E-03	0.0427
99% Conf	3.51E-03	0.0561
Size	3004	3004
Total	14.663	708.92
Min	2.00E-03	0.16
Max	1.506	17.12
Min. Pos	2.00E-03	0.16

6_7	Area (cm²)	Perimeter (cm)
Mean	5.56E-03	0.3228
Median	2.00E-03	0.2
Std. Dev	0.0172	0.3923
Std. Err	4.54E-04	0.0103
95% Conf	8.90E-04	0.0202
99% Conf	1.17E-03	0.0266
Size	1686	1686
Total	8.041	466.5
Min	1.00E-03	0.1
Max	0.338	4.48
Min. Pos	1.00E-03	0.1

6_10	Area (cm²)	Perimeter (cm)
Mean	5.30E-03	0.3373
Median	2.00E-03	0.22
Std. Dev	0.0125	0.401
Std. Err	3.64E-04	0.0116
95% Conf	7.13E-04	0.0228
99% Conf	9.38E-04	0.03
Size	1191	1191
Total	6.308	401.68
Min	1.00E-03	0.1
Max	0.171	4.36
Min. Pos	1.00E-03	0.1

6_13	Area (cm²)	Perimeter (cm)
Mean	0.0135	0.4529
Median	2.00E-03	0.24
Std. Dev	0.1065	0.962
Std. Err	3.03E-03	0.0273
95% Conf	5.93E-03	0.0536
99% Conf	7.80E-03	0.0705
Size	1239	1239
Total	16.703	561.18
Min	1.00E-03	0.1
Max	2.734	20.22
Min. Pos	1.00E-03	0.1